



저작자표시-비영리-변경금지 2.0 대한민국

이용자는 아래의 조건을 따르는 경우에 한하여 자유롭게

- 이 저작물을 복제, 배포, 전송, 전시, 공연 및 방송할 수 있습니다.

다음과 같은 조건을 따라야 합니다:



저작자표시. 귀하는 원저작자를 표시하여야 합니다.



비영리. 귀하는 이 저작물을 영리 목적으로 이용할 수 없습니다.



변경금지. 귀하는 이 저작물을 개작, 변형 또는 가공할 수 없습니다.

- 귀하는, 이 저작물의 재이용이나 배포의 경우, 이 저작물에 적용된 이용허락조건을 명확하게 나타내어야 합니다.
- 저작권자로부터 별도의 허가를 받으면 이러한 조건들은 적용되지 않습니다.

저작권법에 따른 이용자의 권리는 위의 내용에 의하여 영향을 받지 않습니다.

이것은 [이용허락규약\(Legal Code\)](#)을 이해하기 쉽게 요약한 것입니다.

[Disclaimer](#)

Thesis for the Degree of Doctor of Philosophy

**Preparation, characterization and
application of bacterial cellulose based
functional nanocomposites**

박테리아 셀룰로오스 기반
기능성 나노복합체의 제조와 특성 및 응용 연구

August 2016

By

Park, Minsung

Department of Biosystems & Biomaterials

Science and Engineering

SEOUL NATIONAL UNIVERSITY

Thesis for the Degree of Doctor of Philosophy

**Preparation, characterization and
application of bacterial cellulose based
functional nanocomposites**

August 2016

By

Park, Minsung

**Department of Biosystems & Biomaterials
Science and Engineering**

SEOUL NATIONAL UNIVERSITY

Thesis for the Degree of Doctor of Philosophy

**Preparation, characterization, and
application of bacterial cellulose based
functional nanocomposites**

**A Thesis Submitted to the Faculty of Seoul National University
in Partial Fulfillment of the Requirements for
the Degree of Doctor of Philosophy**

**By
Park, Minsung**

Advisor : Professor Jinho Hyun, Ph.D.

August 2016

**Department of Biosystems & Biomaterials
Science and Engineering**

SEOUL NATIONAL UNIVERSITY

Department of Biosystems & Biomaterials
Science and Engineering

SEOUL NATIONAL UNIVERSITY

Supervisory Committee Approval

of Thesis submitted by

Park, Minsung

**This thesis has been read by each member of the following
supervisory committee and has been found to be satisfactory.**

Chairman of Committee :

Lee, Kihoon

Vice Chairman of Committee :

Hyun, Jinho

Member of Committee :

Ki, Chang Seok

Member of Committee :

Youn, Hye Jung

Member of Committee :

Kim, Jaehwan

Preparation, characterization and application of bacterial cellulose based functional nanocomposites

박테리아 셀룰로오스 기반

기능성 나노복합체의 제조와 특성 및 응용 연구

지도교수 현 진 호

이 논문을 박사 학위논문으로 제출함

2016년 5월

서울대학교 대학원
바이오시스템·소재학부
바이오소재전공

박 민 성

박민성의 박사 학위논문을 인준함

2016년 6월

위 원 장 이 기 훈 (인)

부위원장 현 진 호 (인)

위 원 기 창 석 (인)

위 원 윤 혜 정 (인)

위 원 김 재 환 (인)

Abstract

Bacterial cellulose (BC)-based nanocomposites incorporated with inorganic nanoparticles and biopolymers were fabricated by employing suitable synthesis strategies, and their potential applications were investigated. Firstly, a series of BC nanocomposites containing inorganic nanoparticles were synthesized using appropriate methods. BC magnetite nanocomposites (MNP-BC) were biosynthesized by incubating bacteria in a medium containing magnetic nanoparticles (MNPs). Subsequently, polyaniline (PANI) was synthesized on the MNPs-BC nanocomposites by carrying out oxidative polymerization of aniline. Magnetic and electrical measurements confirmed that the MNP-PANI-BC exhibited the potential to be used as an electromagnetic shielding material. Silicon nanoparticles (SiNPs)-BC nanocomposites were prepared by dipping BC in the SiNPs dispersion. SiNPs were uniformly attached to the BC pellicle surfaces along the nanofibers. The conductive PANi-Si-BC composite exhibited stable conductivity under repetitive bending stress, confirming its potential for flexible anode application. Gold nanoparticles (AuNPs)-BC nanocomposites were prepared by employing the *in situ* polymerization of AuNPs on the BC fibers, which could act as a template and an immobilized reducing agent. The surface-enhanced Raman scattering signals corresponding to molecules to be detected on the AuNPs-BC nanocomposite were significantly enhanced due to the spatial deformation of the composite. Secondly, a series of BC nanocomposites containing biopolymers were synthesized with TEMPO-oxidized bacterial cellulose (TOBC). TOBC fibers were obtained using a TEMPO/NaBr/NaClO system at pH 10 and room temperature. The fibrillated

TOBCs mixed with alginate were cross-linked in the presence of Ca^{2+} solution to form hydrogel composites. Alginate/TOBC hydrogel composites exhibited improved mechanical and chemical resistance, indicating that the hydrogel could be used for cell encapsulation applications. Elastin-like polypeptide (ELP)-BC composites were synthesized, which could be used as a thermosensitive hydrogel for cell encapsulation applications. Positively charged ELP was used as a polymeric cross-linker for conjugating with negatively charged cellulose nanofibers. Hydrogel formation was triggered by increasing the temperature, and the hydrogel was converted to the liquid phase by decreasing the temperature.

Keywords: Bacterial cellulose nanocomposite, Inorganic nanoparticles, Magnetite nanoparticles, Silicon nanoparticles, Gold nanoparticles, Biopolymer, Alginate, Elastin-like polypeptide

Student number: 2011-21250

CONTENTS

Chapter 1

Introduction	1
---------------------------	----------

Chapter 2

Literature survey	7
2.1. Cellulose nanofibers.....	8
2.1.1. Cellulose	8
2.1.2. Processes of cellulose nanofibers preparation	12
2.1.3. Three types of cellulose nanofibers	12
2.1.3.1. Cellulose nanocrystals.....	17
2.1.3.2. Cellulose nanofibrils.....	17
2.1.3.3. Bacterial cellulose	19
2.1.4. Surface modification of cellulose nanofibers.....	20
2.2. Bacterial cellulose (BC)	23
2.2.1. General information of BC.....	23
2.2.2. Biosynthesis process of BC	25
2.2.3. Factors affecting the production capacity of BC.....	28
2.2.4. Productivity of BC	30
2.2.4.1. The species and genetic modification of bacteria.....	31
2.2.4.2. Types of reactors for the production process	32

2.2.5. Characteristic differences between the plant cellulose and BC	34
2.2.6. Applications of BC	38
2.2.6.1. Composites with high mechanical strength.....	38
2.2.6.2. Separation and waste purifications.....	39
2.2.6.3. Conducting materials and electrical devices	39
2.2.6.4. Biomedical applications	41
2.2.6.5. Food applications	42

Chapter 3

Electromagnetic BC nanocomposite using magnetite nanoclusters and polyaniline.....	44
3.1. Introduction	45
3.2. Materials and method	48
3.2.1. Preparation of highly dispersive magnetite nanoparticles (MNPs)	48
3.2.2. Biosynthesis of MNP-incorporated BC (MNP-BC) nanocomposites	49
3.2.3. Polymerization of polyaniline (PANi) on the MNP-BC (PANi-MNP-BC) nanocomposites	49
3.2.4. Characterizations of nanocomposites	50
3.3. Results and discussion.....	51

3.3.1. Enhancement of the colloidal stability of MNP solutions	51
3.3.2. Biosynthesis of MNP-BC nanocomposites.....	54
3.3.3. Synthesis of PANi-MNP-BC nanocomposites	58
3.3.4. Electromagnetic properties of nanocomposites	64
3.4. Summary	66

Chapter 4

Flexible conductive BC combined with silicon

nanoparticles and polyaniline	67
4.1. Introduction	68
4.2. Materials and method	71
4.2.1. Preparation of the silicon nanoparticle-embedded BC (Si-BC) nanocomposites	71
4.2.2. Polyaniline (PANi) polymerization with BC (PANi-BC) and Si-BC nanocomposites (PANi-Si-BC).....	71
4.2.3. Characterization of nanocomposites.....	72
4.3. Results and discussion.....	74
4.3.1. Preparation of the Si-BC nanocomposites.....	74
4.3.2. Synthesis of PANi-Si-BC nanocomposites	80
4.3.3. Conductivity of nanocomposite under bending stress	92
4.4. Summary	94

Chapter 5

Surface-enhanced Raman scattering sensor based on a BC hydrogel	95
5.1. Introduction	96
5.2. Materials and method	99
5.2.1. <i>In situ</i> synthesis of gold nanoparticles (AuNPs)-BC.....	99
5.2.2. Characterization of AuNPs-BC nanocomposites.....	99
5.2.3. SERS experiments	100
5.3. Results and discussion.....	100
5.3.1. <i>In situ</i> synthesis of AuNPs-BC hydrogel.....	100
5.3.2. SERS measurement using undeformed AuNPs-BC	105
5.3.3. SERS measurement using deformed AuNPs-BC.....	110
5.3.4. Detection of molecules with weak affinity to Au surfaces.....	114
5.4. Summary	116

Chapter 6

Oxidized BC/alginate hydrogel for cell encapsulation..	117
6.1. Introduction	118
6.2. Materials and method	121
6.2.1. Preparation of TEMPO-mediated oxidized BC (TOBC).....	121
6.2.2. Preparation of alginate/TOBC beads	121

6.2.3. Characterization of alginate/TOBC beads.....	122
6.2.4. Viability and proliferation of encapsulated cells	123
6.3. Results and discussion.....	123
6.3.1. Preparation of alginate/TOBC beads	123
6.3.2. Mechanical and chemical stability of alginate/TOBC.....	131
6.3.3. Permeability of alginate/TOBC beads.....	135
6.3.4. Viability and proliferation of encapsulated cells	139
6.4. Summary	142

Chapter 7

Thermoresponsive hybrid hydrogel of oxidized BC using a elastin like polypeptide	143
---	------------

7.1. Introduction	144
7.2. Materials and method	147
7.2.1. Elastin like polypeptide (ELP) synthesis	147
7.2.2. Sol-gel transition.....	147
7.2.3. Characterization of ELP/TOBC	147
7.2.4. Cell viability and proliferation.....	149
7.3. Results and discussion.....	151
7.3.1. Gel formation of ELP/TOBC	151
7.3.2. Rheological analysis of ELP/TOBC hydrogel	154
7.3.3. Morphological analysis of ELP/TOBC hydrogel.....	157

7.3.4. Mechanism of TOBC/ELP hydrogel formation	160
7.3.5. Viability and proliferation of cells	166
7.4. Summary	168

Chapter 8

Conclusions	169
References	173

List of Tables

Table 2-1. The family of cellulose nanofibers.....	15
--	----

List of Figures

Figure 2-1. Wood hierarchical structure: from tree to cellulose.....	9
Figure 2-2. Schematics of (a) single cellulose chain repeating unit, showing the directionality of the β -(1-4) linkage and intrachain hydrogen bonding (dotted line), (b) idealized cellulose microfibril showing one of the suggested configurations of the crystalline and amorphous regions, and (c) cellulose nanocrystals after acid hydrolysis dissolved the disordered regions.	11
Figure 2-3. Top-down process for obtaining cellulose nanofibers (CNC and CNF).....	13
Figure 2-4. Bottom up process for obtaining cellulose nanofibers (Bacterial cellulose)	14
Figure 2-5. Transmission electron micrographs of a) CNFs and b) CNCs, c) scanning electron micrograph of BC.....	16
Figure 2-6. Schematic images of the major metabolic pathways of <i>G.xylinum</i> and the assembly of cellulose molecules into nanoribbon.	27
Figure 2-7. BC produced under static and agitated conditions.	33
Figure 2-8. General overview of bacterial cellulose structural organization.	36
Figure 2-9. Unique structures and properties of bacterial cellulose.....	37
Figure 3-1. Preparation of electromagnetic BC nanocomposites. (A)	

Dispersion mechanism of MNPs using CLP stabilizer, (B) addition of aniline to BC membrane, and (C) oxidative polymerization by ammonium persulfate	47
Figure 3-2. (A) Dispersion mechanism of MNP using CLP stabilizer, (B) Optical images of an aqueous MNPs solution at different concentration of CLP, (C) Filtration test of (a) MNP solution and (b) CLP-modified MNP solution, and (D) Relative UV absorbance of MNP and CLP-MNP solution as a function of storage time (SD, n=5).	53
Figure 3-3. Optical images of (A) pure BC, (B) MNP-BC, and (C) PANi-MNP-BC. (b) is optical images for showing the magnetic property of MNP-BC using magnetic bar.	56
Figure 3-4. SEM images of (A) pure BC, (B) MNP-BC without CLP and (C) MNP-BC with CLP.....	57
Figure 3-5. SEM images of (A) PANi-BC and (B) PANi-MNP-BC, (C) magnified image of A and, (D) magnified image of B.	59
Figure 3-6. FT-IR spectra of (A) BC and (B) PANi-MNP-BC.....	61
Figure 3-7. TGA curves of (A) BC, (B) MNP-BC, (C) PANi-BC and (D) PANi-MNP-BC.....	63
Figure 3-8. Magnetic hysteresis curves of BC nanocomposites.....	65
Figure 4-1. Schematic representation of the process for preparing PANi-Si-BC	

composite.	70
Figure 4-2. Hydroxyl groups were introduced on the surface of SiNPs as a result of modification with phytic acid. Hydroxyl groups of SiNPs can form hydrogen bonds with BC nanofibers	75
Figure 4-3. Optical images of (A) pure BC, (B) Si-BC composite and (C) the weight percentage of SiNPs bound to BC in Si-BC composite as a function of incubation time in SiNP-dispersion solution.	76
Figure 4-4. FE-SEM images of BC and Si-BC composite. (A) Surface and (C) cross section of freeze-dried BC. (B) Surface and (D) cross section of freeze-dried Si-BC composite	79
Figure 4-5. After adding aniline monomer and APS, PANi was polymerized on both BC nanofibers and SiNPs. The BC structure can serve as the template for both the adsorption of SiNPs and the polymerization of PANi	81
Figure 4-6. (A and B) Conductivity and contents of PANi/BC with molar ratios of APS to aniline from 0.25 to 2. (Polymerization time was 1h and reaction temperature was 20 °C), (C and D) Conductivity and contents of PANi-Si-BC with reaction time from 0.5 h to 2 h. (Molar ratio of oxidant (APS) to monomer (aniline) was 1 and reaction temperature was 20 °C), and (E and F) Conductivity and contents of PANi-Si-BC with different reaction temperature 5 °C and 30 °C. (Molar ratio of oxidant (APS) to monomer (aniline) was 1 and	

reaction time was 1h.....	82
Figure 4-7. SEM images of composites. (A) Surface image of PANi-BC, (B) surface image of PANi-Si-BC, and (C) cross sectional images of freeze-dried PANi-Si-BC.....	84
Figure 4-8. TEM images of composites. (A) Si-BC and (B) PANi-Si without phytic acid. (C) PANi-Si and (D) PANi-Si-BC with phytic acid.....	85
Figure 4-9. XRD patterns of composites. (A) SiNPs, BC, PANi-BC, and PANi-Si-BC. (B) Change of crystallinity after the incorporation of SiNPs in BC	87
Figure 4-10. Thermal stability of the composites. Thermogravimetric curves of BC, Si-BC and PANi-Si-BC were obtained using 10 mg of a vacuum dried sample in the range of temperature from 25 °C to 600 °C at a heating rate of 10 °C min ⁻¹ under flowing nitrogen	88
Figure 4-11. Effect of phytic acid on the composites. (A) Morphological change and (B) the thermal stability of composites	91
Figure 4-12. Electrical stability of the composites to bending stress. (A) Optical images of bending process using UTM and parameters for the calculation of the bending radius, (B) resistance variation of PANi-Si-BC composite for changes in bending radius, and (C) the percentage of resistance change of the composite according to bending cycles up to 100 cycles.....	93

Figure 5-1. Schematic representation of the process for preparing AuNPs-BC hydrogel.....	98
Figure 5-2. Preparation of highly dispersed AuNPs-BC. Optical image of normal BC (A) and AuNPs-BC (B). (C) Absorption spectra of AuNPs-BC and normal BC and (D) characteristic XRD peaks of AuNPs-BC and normal BC.....	102
Figure 5-3. TEM images of AuNPs-BC synthesized with different reaction time. (A) 5, (B) 30 and (C) 60 min. Inserted micrographs are SEM images of each samples. (D) EDS spectrum from SEM image of sample (B)	104
Figure 5-4. The multilayer structure of the BC hydrogel. (A) The cross-sectional SEM image of the freeze-dried BC hydrogel, (B) spacing between BC layers, and (C) the thickness of the BC hydrogel as a function of cultivation time	106
Figure 5-5. SERS measurement with undeformed AuNPs-BC hydrogel. (A) Typical Raman spectrum 4-FBT on AuNPs-glass and undeformed AuNPs-BC. (B) Effect of layer number on SERS intensity. SERS signal at 1075 cm^{-1} was compared.....	107
Figure 5-6. SERS spectra of different concentrations of 4-FBT obtained with (A) two dimensional AuNPs-attached glass substrate, and (B) undeformed AuNPs-BC.....	109
Figure 5-7. FE-SEM images of AuNPs-BC composites. Top view (A) and	

cross-section (B) of hydrogel-state of Au30-BC. Top view (C) and cross-section (D) of spatially deformed Au30-BC 111

Figure 5-8. Effect of spatial deformation of AuNPs-BC hydrogel on SERS signal. SERS spectra of 4-FBT obtained with undeformed AuNP-BC, and spatially deformed AuNP-BC. 4-FBT concentration: 10^{-3} M.... 112

Figure 5-9. Detection of 4-FBT with AuNPs-BC composites (A) Schematic description for additional enhancement of SERS in case of the molecules which have strong affinity to noble metal surface such as 4-FBT (B) SERS spectra of 4-FBT obtained with undeformed AuNP-BC substrates, (C) SERS spectra of 4-FBT obtained with spatially deformed AuNP-BC substrates, and (D) SERS intensities comparison for three substrates..... 113

Figure 5-10. Detection of PAA with AuNPs-BC composites (A) Schematic description for additional enhancement of SERS in case of molecules which have weak affinity to noble metal surface such as PAA (B) SERS spectra of PAA obtained with unmodified AuNP-BC substrates and (C) SERS spectra of PAA obtained with spatial deformed AuNP-BC substrates (D) SERS spectrum of PAA with concentration of 1×10^{-7} M 115

Figure 6-1. Schematic representation of alginate and TOBC beads. (A) Optical microscopy image of alginate bead and scheme of surface structure of alginate bead, (B) Scheme of the structure of egg-box

junction zones of alginate. (C) optical microscopy image of alginate/TOBC bead and scheme of surface structure of alginate/TOBC bead, (D) Scheme of the structure of egg-box junction zones of alginate/TOBC 120

Figure 6-2. Selective oxidation of C6 primary hydroxyls of cellulose to carboxylate groups by TEMPO/NaBr/NaClO oxidation in water at pH 10. (A) Chemical structures of pure BC and TOBC, (B) A relationship between the amount of NaClO and the carboxylate content of the oxidized cellulose, (C) FT-IR spectra for pure BC and TOBC, and (D) X-ray diffraction patterns of the pure BC and TOBC 125

Figure 6-3. Preparation of the TOBC. (A) Optical image of pure BC, (B) TEM images of pure BC, and (C) TOBC 128

Figure 6-4. SEM images of surface morphology of alginate/TOBC microbeads regarding the TOBC content. (A) alginate beads, (B) alginate /TOBC10 beads and (C) alginate /TOBC20 beads. Inserted micrographs are optical images of each samples. (D~F) are magnified images of (A~C)..... 129

Figure 6-5. (A) FT-IR spectra for alginate/TOBC composites with various cellulose contents. (B) XRD patterns for alginate/TOBC composites with various TOBC contents 130

Figure 6-6. (A) Compressive stress-strain curves for various alginate/TOBC beads. (B) Compressive Modulus of various alginate/TOBC beads 132

Figure 6-7. Microscopy images of alginate and alginate/TOBC20 microbeads as formed (A, D), after being exposed to 40 mM sodium citrate in 6min(B, E) and 60 min (C, F). Scale bar = 500 μm (G) SEM images of alginate/TOBC20 microbeads after being exposed to 40 mM sodium citrate in 60 min. (H) is magnified images of (G) 134

Figure 6-8. Fluorescence microscopic images for permeability assessment of various alginate/TOBC microbeads. Alginate beads with 4 kDa FITC-Dextran (A) and 150 kDa FITC-Dextran (B) was immersed in water. After 30 min, 4 kDa FITC-Dextran was released out of the beads (A₂). 150 kDa FITC-Dextran could not be released out of the beads. (B₂). (C) and (D) are alginate/TOBC10 samples. (E) and (F) are alginate/TOBC20 samples..... 137

Figure 6-9. Confocal microscopy section images for permeability assessment of various alginate/TOBC microbeads. Alginate beads incubated with 4 kDa FITC-Dextran (A) and 150 kDa FITC-Dextran (B). Alginate/TOBC10 beads incubated with 4 kDa FITC-Dextran (C) and 150 kDa FITC-Dextran (D). Alginate/TOBC20 beads incubated with 4 kDa FITC-Dextran (E) and 150 kDa FITC-Dextran (F). Scale bar = 50 μm 138

Figure 6-10. Optical microscopy images of cells encapsulated in alginate (A), alginate/TOBC (B), and alginate/TOBC20 (C). Cell numbers for various alginate/TOBC beads as function of cultured days. Scale bar=250 μm 140

Figure 6-11. After recovering the cells from beads, Live/Dead staining were conducted. The fluorescence images are the staining results of cells encapsulated in alginate (A), alginate/TOBC10 (B), and alginate/TOBC20 beads (C). Scale bar=250 μm 141

Figure 7-1. Schematic representation of the process for preparing ELP/BC hydrogel..... 146

Figure 7-2. Temperature-triggered sol-gel transition of the ELP/TOBC complex. (A) TOBC only, (B) ELP only, and (C) ELP/TOBC 152

Figure 7-3. Turbidity variations of ELP (A) and ELP/TOBC (B) solution as a function of temperature (OD at 350 nm, Heating: 1 $^{\circ}\text{C}/\text{min}$)..... 153

Figure 7-4. Oscillatory temperature ramp measurements to confirm hydrogel formation. (A) ELP/TOBC complex, (B) pure TOBC solution, (C) pure ELP solution. (Heating rate: 2 $^{\circ}\text{C}/\text{min}$. Concentration of samples: 2 wt%) 156

Figure 7-5. FE-SEM images of freeze-dried TOBC (A and A₁), ELP/TOBC solution (B and B₁), and ELP/TOBC shrunken hydrogel (C and C₁). Schematic representation of TOBC (A₂), ELP/TOBC solution (B₂), and ELP/TOBC hydrogel (C₂)..... 159

Figure 7-6. (A) Zeta potential for individual biopolymers and biopolymer composites at 20 $^{\circ}\text{C}$, and (B) AFM images of TOBC and ELP/TOBC composites 161

Figure 7-7. Effect of pH at pH 12 on the formation of ELP/TOBC hydrogels.
The ELP/TOBC solution was adjusted to pH 12 to eliminate positive charges on the ELP molecules. The resulted in the inability to form a hydrogel despite increased temperature 164

Figure 7-8. CD spectra of ELP/TOBC and ELP obtained at different temperatures in water. ELP concentration was 0.5 mg/mL in both the ELP/TOBC and pure ELP solutions 165

Figure 7-9. (A) MTT results of ELP/TOBC solution, (B, C) Fluorescence microscopic images of fibroblast cells encapsulated in a ELP/TOBC hydrogel after (B) 1 day and (C) 7 days of incubation (cells were live/dead stained)..... 167

Chapter 1

Introduction

1. Introduction

Biopolymer-based nanocomposite materials have attracted significant attention in many industries owing to their impressive and ecofriendly properties [1]. Bio-based materials prepared using natural rubber [2-5], chitin or chitosan [6-9], polylactic acid [10], polyhydroxybutyrate [11], alginate [12-14], and cellulose [15, 16] have been extensively investigated. In particular, cellulose has received significant attention owing to its abundance in nature, sustainability, low cost, biosafety, biodegradability, and high potential in various applications [17]. Natural cellulose-based materials have been used for engineering and building materials as well as in forest products, paper, and textiles for thousands of years [18]. In the last decades, there have been several efforts to reduce the diameter of cellulose fibers to prepare cellulose nanofibers. Cellulose nanofibers are one of the most attractive materials that could satisfy the increasing demands for high-performance materials owing to its excellent mechanical properties, biocompatibility, tailorable surface modification, and renewable nature [19]. Cellulose nanofibers can be divided into three types: cellulose nanocrystals (CNCs), cellulose nanofibrils (CNFs), and bacterial cellulose (BC) [20, 21].

Among these materials, BC exhibiting unique structural features is considered an ideal nanomaterial for fabricating composites with various materials [22]. BC exhibits an ultrafine fibrous nano-sized three-dimensional (3D) network structure, which could serve as a potential reinforcing matrix in

composites. The well-arranged web-shaped fibrous network structure of BC fibers can bind or engage with nanoparticles. Besides, the presence of hydroxyl groups in the cellulose chain allows it to interact with other hydrophilic materials to form stable composites [23].

The preparation of BC-based nanocomposites could be categorized into four different methods: (1) biosynthesis of BC in a medium containing nanoparticles, (2) dipping BC in nanoparticles suspension, (3) *in-situ* synthesis of nanoparticles on the BC fiber surfaces, and (4) blending of modified cellulose with other biopolymers. Biosynthesized BC composites can be prepared by adding functional materials into the culture medium. Dipping of BC in the nanoparticle suspended solution is a simple method. However, it is difficult to obtain a uniformly distributed nanocomposite since nanoparticles cannot be diffused through the BC layers. The *in-situ* synthesis method enables the production of composites with a high density of functional materials. In this process, BC nanofibers are used not only as a template, but also as an immobilized reducing agent for synthesizing nanomaterials. Meanwhile, the highly networked BC fibers could be surface-modified and individually dispersed in aqueous solutions. In the modification and blending method, these dispersed BC nanofibers are mixed with other biopolymers to form a stable gel-like structure.

In this thesis, a series of BC based nanocomposites incorporated with inorganic nanoparticles or biopolymers and their potential electronics, sensor,

and medical applications are discussed. Appropriate methods for the synthesis of BC-based nanocomposites were designed by choosing functional materials for forming the composites with BC depending on the required applications. The best method for preparing composites was selected from the methods mentioned above.

1. Magnetite nanoparticles (MNPs)-BC nanocomposite by biosynthesis method.

An electromagnetic BC composite was synthesized by culturing *Gluconacetobacter xylinus* in a medium containing MNPs. Using comb-like polymer (CLP) as a polymer surfactant, the magnetite nanoparticles were stably dispersed in the culture medium as magnetite nanoclusters (MNCs). Subsequently, PANi was synthesized on the magnetic BC fibers by chemical oxidative polymerization. The morphology and electromagnetic properties of the BC nanocomposite were investigated.

2. Silicon nanoparticles (SiNPs)-BC nanocomposite by dipping method.

A flexible conductive BC composite was synthesized by dipping BC in SiNPs suspended solution. BC was used as a template for binding SiNPs. Subsequently, PANi was formed on the modified SiNPs and BC fibers by *in situ* polymerization of aniline monomers. The morphology and the electrical stability of the BC nanocomposite in the bending state were investigated.

3. Gold nanoparticles (AuNPs)-BC nanocomposite by *in situ* synthesis.

BC hydrogels containing AuNPs were prepared by *in situ* synthesis method. BC nanofibers were used not only as a template, but also as an immobilized reducing agent for preparing the AuNPs-BC hydrogel. The increase in the surface-enhanced Raman scattering (SERS) hot spot density driven by the spatial deformation of AuNPs-BC hydrogels is discussed.

4. Alginate/BC nanocomposite using modified BC fibers

Micro-hydrogels were prepared using BC nanofibers and alginate. TEMPO-mediated oxidized bacterial cellulose (TOBC) was used to improve the mechanical and chemical stability of the alginate hydrogel. The fibrillated TOBCs mixed with alginate were cross-linked in the presence of Ca^{2+} solution to form hydrogel composites. The mechanical and chemical stability of composites were investigated. In addition, the viability of the cells encapsulated in the alginate/TOBC composite was investigated for examining the potential biomedical applications of the composite.

5. Elastin-like polypeptide (ELP)/BC nanocomposite using modified BC fibers

A thermoresponsive polysaccharide hydrogel based on nanofibrous cellulose and ELP was prepared. Well-dispersed BC nanofibers were obtained by TEMPO mediated oxidation method. ELPs in the composite folded and

coacervated when the temperature increased above T_i , causing TOBCs to rope together and form a porous hybrid hydrogel of ELP and TOBC. Morphological and conformational changes of the composites were analyzed, and the biocompatibility of the composites for cell encapsulation was investigated.

Chapter 2

Literature survey

2. Literature survey

2.1. Cellulose nanofibers

2.1.1. Cellulose

Cellulose is considered to be the most abundant biopolymer and an important source of sustainable future as alternatives to synthetic products [24]. The origin of the word ‘material’ is known to be driven from the Latin for ‘trunk of tree’. It shows that there is a deep relationship with the wood and material [18]. Indeed, Wood containing cellulose has been used as the most representative material for a long time as an energy source, clothing, and building materials like timber for house, ship and other various fields. Also, since the Egyptian papyri as a paper, cellulose products have played an important role in the recording of culture [1]. In nature, cellulose is synthesized in large amounts by plants, where it is an essential component of the cell walls. Cellulose secreted as an extracellular product imparts mechanical strength to the cell wall and determines the direction of cell growth [20]. Wood hierarchical structure from tree to cellulose is shown in figure 2-1 [25].

Cellulose is composed of carbon, hydrogen and oxygen and it is classified carbohydrate. The repeat unit of the cellulose is cellobiose to comprise two anhydroglucose rings joined via a β -1,4 glycosidic linkage. Native cellulose is typically called cellulose I. This cellulose I form comprises

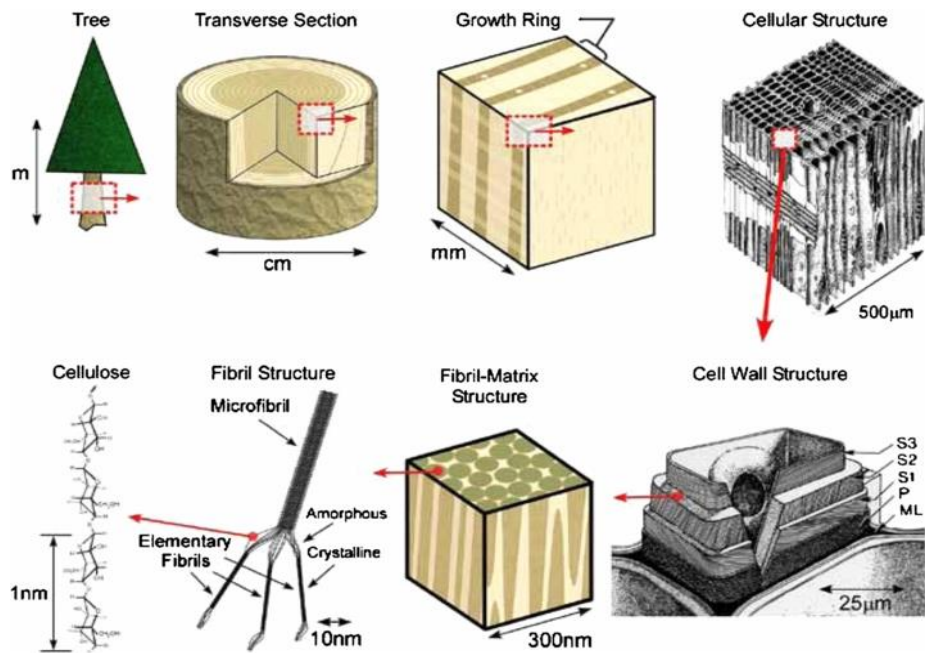


Figure 2-1. Wood hierarchical structure: from tree to cellulose [25].

two allomorphs, called cellulose I α and I β [20, 26]. The ratio of cellulose I α and I β is known to differ according to plant species, but cellulose I α is rich in the bacterial cellulose [20, 27]. The crystalline structures of cellulose I allomorphs have been characterized with the sophisticated hydrogen bonding system which does not allow cellulose to be dissolved in typical aqueous solvents immediately (figure 2-2) [20]. In addition, the stable crystalline structure makes cellulose have no melting point. Due to this unique structural feature, cellulose chains are highly stiff in the axial direction, which is essential property for the reinforcing roles of fiber in a composite [28].

Wood pulp have been used for some industrial feedstock such as the production of paper and cardboard, cellulose regeneration, and the large scale synthesis of cellulose derivatives. Apart from plants, some bacteria, fungi, and algae produce cellulose as well. Among the bacteria to synthesize the cellulose, *Gluconacetobacter xylinum* (*G. xylinum*) effectively synthesizes cellulose as a primary metabolic product. They are commonly found on fruits and can be easily cultivated under laboratory conditions [29].

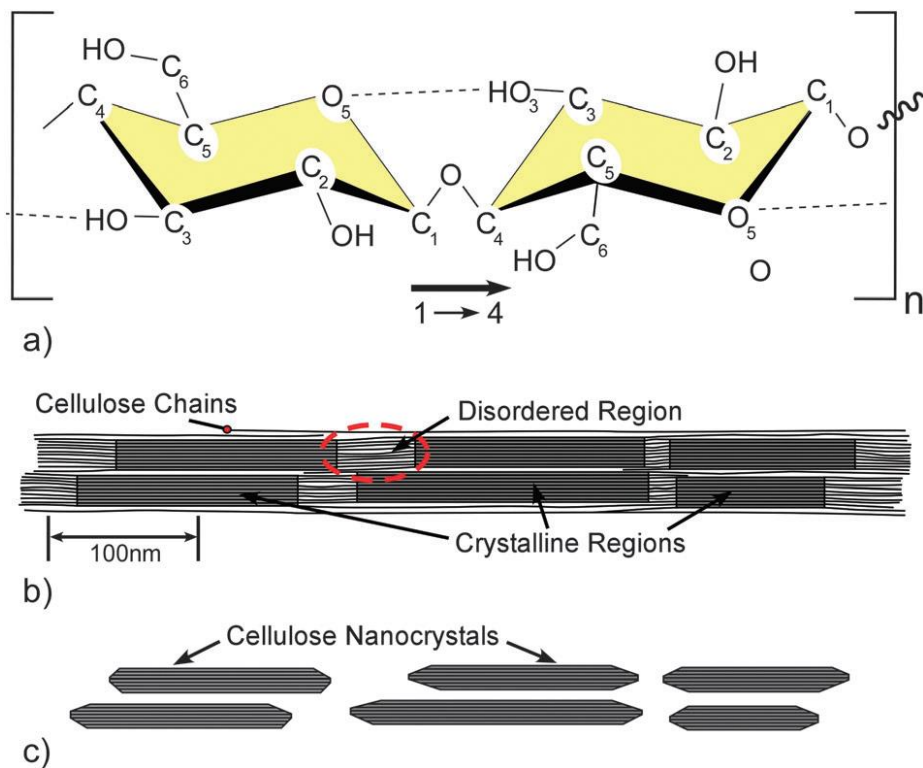


Figure 2-2. Schematics of (a) single cellulose chain repeating unit, showing the directionality of the β -(1-4) linkage and intrachain hydrogen bonding (dotted line), (b) idealized cellulose microfibril showing one of the suggested configurations of the crystalline and amorphous regions, and (c) cellulose nanocrystals after acid hydrolysis dissolved the disordered regions [20].

2.1.2. Processes of cellulose nanofibers preparation

In the last decades, there have been efforts to reduce the diameter of wood fibers. As a first effort, a micro-fibrillated cellulose (MFC) was developed in the early 1980s [18, 30]. Such isolated cellulosic materials have nanometer sized diameter are referred to as cellulose nanofibers. Today, there are two different ways to prepare cellulose nanofibers with controlled fiber diameters [31].

One is Top-down process involving physical, chemical, and enzymatic method for producing cellulose nanofibers from wood (figure 2-3) [32] and the other one is bottom-up synthesis of cellulose nanofibers from glucose by bacteria (figure 2-4) [33]. Cellulose nanofibers have unique properties such as excellent mechanical property, hydrophilicity, broad chemical-modification capacity, and very large surface area, and so on [17].

2.1.3. Three types of cellulose nanofibers

The cellulose nanofibers can be divided into three types such as cellulose nanocrystal (CNCs), cellulose nanofibrils (CNFs) and bacterial cellulose (BC) (Table 1). Different approaches are needed to obtain nanomaterial from cellulose sources [1]. Figure 2-5 is electron microscope images of the three types of cellulose nanofibers.

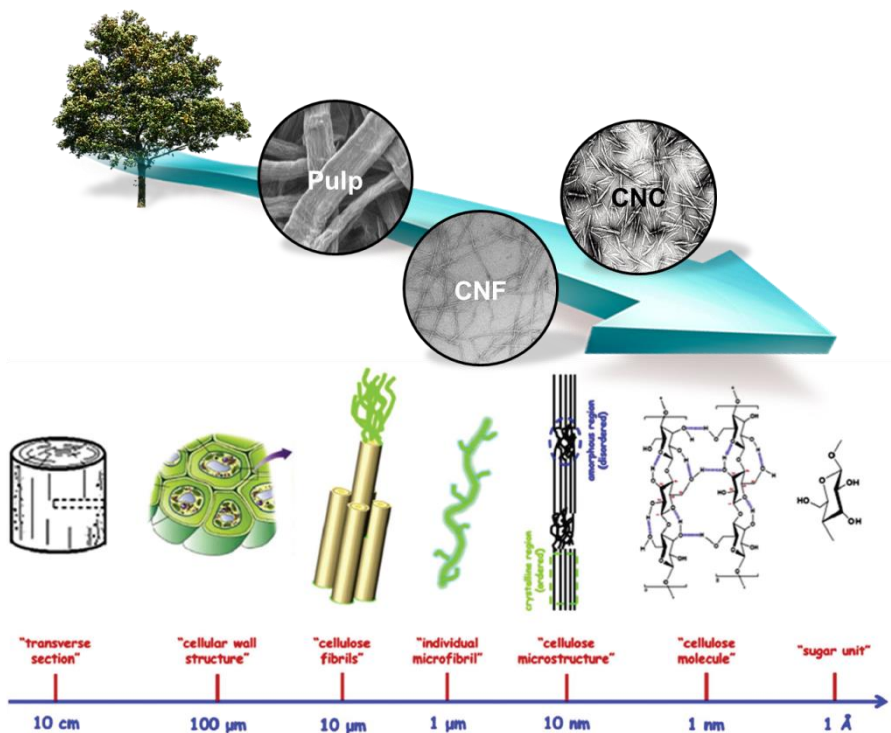


Figure 2-3. Top-down process for obtaining cellulose nanofibers (CNC and CNF) [32].

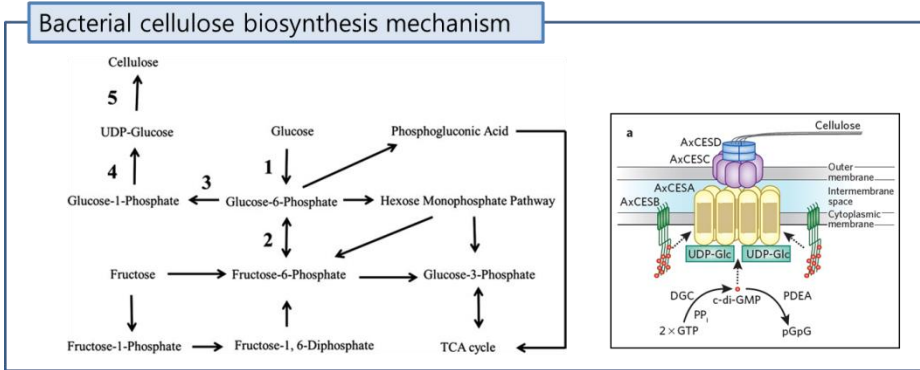
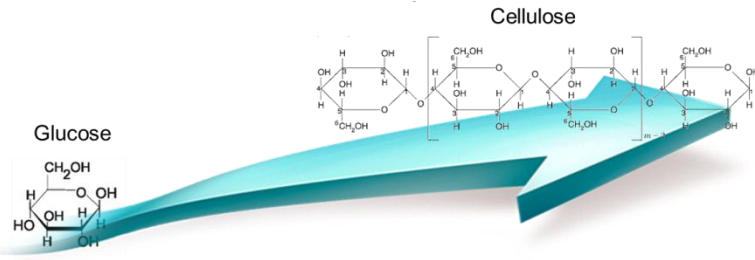


Figure 2-4. Bottom up process for obtaining cellulose nanofibers (Bacterial cellulose) [33].

Table 1. The family of cellulose nanofibers [1].

Type of nanocellulose	Selected references and synonyms	Typical sources	Formation and average size
Cellulose nanocrystal (CNC)	Cellulose nanocrystals, crystallites, whiskers, rodlike cellulose microcrystals	Wood, cotton, hemp, flax, wheat straw, mulberry bark, ramie, Avicel, tunicin, cellulose from algae and bacteria.	Acid hydrolysis of cellulose from many sources diameter: 5-70nm Length: 100-250 nm (from plant celluloses);100 nm to several micrometers (from celluloses of tunicates, algae, bacteria)
Cellulose nanofibril (CNF)	Microfibrillated cellulose, nanofibrils and microfibrils, nanofibrillated cellulose	Wood, sugar beet, potato tuber, hemp, flax	Delamination of wood pulp by mechanical pressure before and/or after chemical or enzymatic treatment Diameter: 5-60 nm Length: several micrometers
Bacterial nanocellulose (BC)	Bacterial cellulose, microbial cellulose, bio-cellulose	Low-molecular-weight sugars and alcohols	Bacterial synthesis Diameter: 200-100nm; different types of nanofiber networks

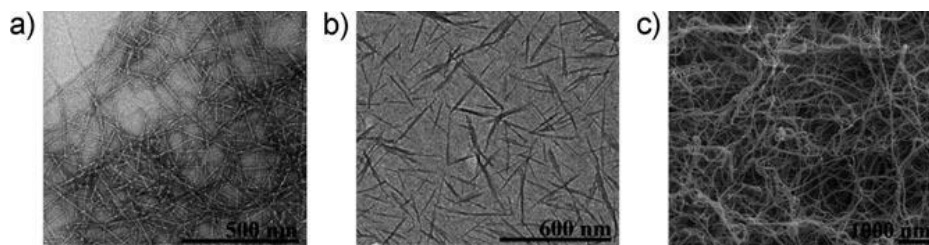


Figure 2-5. Transmission electron micrographs of a) CNFs and b) CNCs, c) scanning electron micrograph of BC [1, 54].

2.1.3.1. Cellulose nanocrystals

Cellulose nanocrystals (CNCs) isolated from cellulose can be obtained by acid-hydrolysis [34]. Non-crystalline regions of cellulose are hydrolyzed, whereas crystalline regions are protected from acid attack [35]. Following an acid hydrolysis, rod-like cellulose nanocrystals are obtained. The kinds of acid and the acid to cellulose ratio are critical parameters that influence the generated chemical character and efficiency of production of CNCs [36]. Sulfuric acid has been most widely used for preparing CNCs [37]. Extraction of the nanocrystals from cellulose involves selective hydrolysis of amorphous regions of cellulose, resulting in crystalline particles with source dependent diameter for plant source (from 5-20 nm to 100–500 nm) [20]. Sulfuric acid hydrolysis makes negatively charged sulfate ester groups onto the surface of the CNCs. The electrostatic repulsion of negatively charged surface act to prevent aggregation in aqueous suspension [38]. In addition, the rod-like shape of CNCs leads to self-assembly behavior of liquid crystalline [39]. CNCs are not soluble in various organic solvents, but can be dispersed in water as a colloidal suspension form. The stability of the CNCs suspensions depends on several parameters such as the size of polydispersity, dimensions of crystallites, and the surface charge [34].

2.1.3.2. Cellulose nanofibrils

Cellulose nanofibrils (CNFs) have micrometer-long entangled fibrils and

preserves noncrystalline domains in the microfibril unlike CNC [40]. It is worth noting that entanglement of the cellulose nanofibers in aqueous suspension gives high viscosity at relatively low concentrations [41]. The CNFs can be mainly prepared by three types of processes [24]: 1) mechanical treatments (high-pressure homogenization, cryo-crushing, and grinding), 2) chemical treatments (TEMPO-mediated oxidation), and 3) combination of chemical and mechanical treatments.

First, there are some mechanical methods for obtaining CNF from the pulp. (1) Refining and high-pressure homogenization is general method [42]. The principle of the method is that dilute pulp-water suspensions pass through a mechanical homogenizer, with a large pressure to facilitate microfibrillation. (2) cryo-crushing is used to obtain CNFs [43]. A frozen pulp via liquid nitrogen is mechanically crushed. (3) Grinder is used in order to prepare CNFs [42]. The cellulose slurry is passed between two a rotating grinder stones. Hydrogen bonds are broken down by the shearing forces generated by the grinding stones and then nanosized fibers are individualized from the pulp [44]. Threadlike long bundles of cellulose molecules are bonded by hydrogen bonds between the many hydroxyl groups in the cellulose. After mechanical treatment, hydrogen bonds are broken by the shearing forces of the grinding stones and then nanosized fibers are obtained from the pulp [45]. As an example, CNFs having diameters in the range 20–90 nm were prepared by a grinding method [46].

Second, chemical treatments were used for obtaining CNFs from pulp. The introduction of charged groups into the cellulose fibers could enhance delamination of the fiber walls [1]. Through the introduction of carboxyl or carboxymethyl groups by TEMPO-mediated oxidation [47] or carboxymethylation [48], fully delaminated CNFs may be produced. Such groups should be in the form of their sodium salts to cause as much swelling of the fibers as possible. Swollen cellulose has low cell-wall cohesion and should be easier to delaminate [1].

Lastly, combinations of chemical treatments and mechanical treatments are used to obtain CNFs, especially for enhancing the efficiency [1, 36]. Generally, the pre-treatments involve enzymatic modification [49, 50] or an introduction of charged groups on the fiber surfaces such as a carboxylation by TEMPO-mediated oxidation [51]. These pre-treatment will affect the surface properties of the fibers, which can make it easier to peel the fiber in the following mechanical process [36]. Therefore, combinations of chemical treatment and mechanical treatment allow more efficient preparation process of CNFs with less energy, time, and amounts of chemicals [1, 52].

2.1.3.3. Bacterial cellulose

Bacterial cellulose (BC) was produced by microorganisms. *Gluconacetobacter xylinum* is the most efficient bacteria to synthesize cellulose nanofibers [53]. These bacteria existed in nature where the

fermentation of sugars. In contrast to cellulose isolated from plant sources, BC is formed as nanomaterial by biotechnological synthesis processes from low-molecular weight carbon sources, such as glucose. The bacteria are cultivated in aqueous nutrient medium, and the BC is excreted as exopolysaccharide at the interface between the air and medium [54]. One of initial applications of the natural bacterial cellulose (BC) was a calorie-free dessert called Nata de coco [55].

2.1.4. Surface modification of cellulose nanofibers

In many cases, cellulose nanofibers play an important role as the filler in the composite material [57]. However, nanoscale crystallites and nano-scale fibers can undergo co-crystallization and aggregation [58]. Therefore, chemical modification of cellulose has been considered as a solution to improve the filler dispersion in polymer matrices [24]. In addition, chemical compatibility between the filler material and the continuous matrix material is critical in the adhesion and combination between the two materials, resulting in the enhancement of mechanical properties [24, 59]. Cellulose nanofibers can be derivatized by various direct reactions due to many hydroxyl groups on the surface and relatively large specific surface area, providing abundant active sites for chemical modification [20, 28].

Modifications forming covalent bonds, involving oxidation [60], esterification [61], etherification [62], polymer grafting [63], and silylation

[64], and modifications forming non-covalent bonds [65] are considered as reactions to introduce functional groups onto cellulose surfaces or as intermediate forms for additional modification. Cellulose surfaces can be more hydrophilic by introducing some ionic functional groups such as carboxylic and sulfuric groups. The surfaces become to have negative charges in their base forms.

2,2,6,6-tetramethylpiperidine-1-oxyl radicals (TEMPO) was used for creating carboxylate and aldehyde functional groups on the cellulosic surfaces [66]. Also, cellulose nanocrystal (CNC) from cellulose fibers by the treatment with sulfuric acid has negative charges on the cellulosic surfaces [67]. These hydrophilic properties of modified cellulose nanofibers improve the colloidal stability in aqueous solution [1].

In some occasions, the hydrophilic hydroxyl groups on the CNCs surfaces make it difficult to disperse in nonpolar solvents and polymer matrices, thus hydrophobization process is often utilized to improve compatibility. A number of hydrophobic groups can be introduced by acetylation [68], alkylation [69], and fluorine treatment [61].

Grafting reaction is another technique for cellulose modifications, which has been investigated to modify CNCs by ‘grafting-onto’ and ‘grafting-from’ techniques. The grafted chains not only improve the interaction between polymer matrix and CNC filler, but also enable the stress-transfer contributing

to the strength of nanocomposite materials [63, 70].

Meanwhile, polymer grafting can impart some unique properties to the cellulosic surfaces. For instance, CNCs grafted with PNIPAM brushes showed thermo-responsive property [71] and CNCs grafted with cationic polymers [63] expected to have potential for pH-responsive drug delivery and gene therapy. Grafting reaction can be used for attachment of various fluorophores on the surface of cellulose nanofibers, including FITC, RBITC, DTAF, poly(amidoamine) dendrimers, etc. These fluorescein-labelled nanomaterials are expected to have potential in biosensing, bioimaging, and biodetection in the medical fields [72, 73].

Most commonly, surfactant is used to stabilize the cellulose nanofibers and modify the surface characteristics of cellulose. Due to its lack of dispersibility in organic solvent and polymers, cellulose nanofibers are commonly stabilized with surfactants [20]. A variety of studies have reported that addition of surfactant improved the stability of cellulose nanofibers in solution and compatibility between cellulose nanofibers and matrix polymers in the formation of composites. It is proposed that the hydrophilic head group of surfactant adsorbs on the cellulose surface while its hydrophobic tail interacted with matrix [74].

Sulfuric acid derived CNCs provide a charged surface to adsorb surfactants. Such dispersants as stearic acid and

cetyltetramethylammoniumbromide (CTAB) are common [75]. Another method using adsorptive modification is through the use of electrostatic adsorption. Layer-by-layer (LBL) deposition is commonly used [76]. Xyloglucan block copolymers have been used as a non-ionic absorbant/dispersant due to its strong and specific adsorption property for cellulose [77]. Much less electrostatic stabilization is reported for the CNFs. This is likely due to the lower surface charge compared to CNCs. However, dispersants derived from guluronic, mannuronic acids, and ethylene-acrylic acid copolymers have been used [78].

2.2. Bacterial cellulose (BC)

2.2.1. General information of BC

The cellulose about the production of vinegar, Nata de coco, and Kombucha tea has been observed and used for centuries, even though formerly recognized as metabolite of the bacterium [79, 80]. It was firstly confirmed as cellulose in 1886 by Brown [54]. Although not yet fully understood, there are some theories about the reason why the bacteria produce cellulose. The cellulose is thought to help the bacteria to move over the surface by entrapment of carbon dioxide produced from the tricarboxylic acid cycle. This phenomenon is important to survival of bacteria since the bacteria are aerobic. The cellulose also immobilizes the bacteria for protects the bacteria from enemies and helps bacteria attach to the surface of objects that

supply the nutrition. In addition, the cellulose can protect the bacteria from ultraviolet (UV) light and dehydration [54].

While researching with acetic acid bacteria, a gel-like solid material was found in the process of vinegar fermentation, which was named as vinegar plant [81]. This solid mass was recorded that has similar feel of the animal tissue with high toughness [82]. Among the bacteria to synthesize the cellulose, *Acetobacter* strains are suitable for the synthesis of cellulose. The genus *Acetobacter* refers to a group of bacteria that has the ability to oxidize sugars and produce acetic acid as the major end product. Reclassified as the genus *Gluconacetobacter* strains, especially *Gluconacetobacter xylinum* (*G. xylinum*) effectively synthesize the cellulose as a primary metabolic product [55]. *G. xylinum* are found on rotting fruits that have fixed sugars. They existed at the air-medium interface and their presence can be detected if they synthesize a cellulose pellicle or film [54]. *G. xylinum* are rod-like shaped bacteria without a flagellum, and although it is nonmotile, movement of bacteria can be observed by microscope during the synthesizing of the cellulose ribbon [54]. At stationary culture condition, cellulose is produced mat-like pellicle. While in shaking cultures of *G. xylinum*, cellulose is produced as small sphere form. The BC fibrils in sphere form have relatively lower cellulose Ia content and have lower Young's modulus, but higher water holding capacity comparing to BC membrane cultured in static condition [83].

The biosynthesis of cellulose is the exciting option to produce cellulose

by culturing the bacteria in the sense of white biotechnology and to control the structure and shape of the cellulose during biosynthesis. The resulting cellulose leads to new properties, functionalities, and applications [83].

2.2.2. Biosynthesis process of BC

The synthesis of the BC is based on an accurate and regulated process, involving many of enzymes and protein complexes. The biosynthesis of BC by bacteria could be divided into four parts, which were polymerizing, secreting, assembling and crystallizing [84, 85]. Through microscopic studies of the bacterial, the presence of cellulose ribbons attached to the longitudinal axis of the cell was found. Also, through a freeze fracture analysis, a linear array of pores in the cell envelope of *G. xylinus* was found [86, 87]. When *G. xylinus* is cultivated in glucose based media, essentially four enzymatic steps have been found in the pathway from glucose to cellulose. These are the phosphorylation of glucose by glucokinase, the isomerization of glucose-6-phosphate to glucose-1-phosphate by phosphoglucomutase, the synthesis of uridine diphosphate glucose (UDP-glucose) from glucose-1-phosphate by UDP-glucose pyrophosphorylase and the synthesis of cellulose from UDP-glucose by cellulose synthase [88]. At the beginning state, about 6-8 glucan chains were combined. Polymerization of glucose residues to form a glucan chain was taken place in the membrane. Assembling of the cellulose I crystallite is proposed to proceed in stages, with the formation of glucan chain sheets by hydrogen bonding of molecules. Final crystallization of the glucan

chains like a ribbon form into cellulose I occurring in the extracellular space [85]. Figure 2-6 shows the way how glucan chains are aggregated together. The terminal complex (TC) which was placed at the surface of the cell was considered to be the start point of forming cellulose. The TC is comprised of a subunits (grouped in triplets) and each subunit in the cytoplasmic membrane produces at least 16 cellulose chains that arrange in a mini-crystal (elementary fibril). For each triplet subunit, the three elementary fibrils closely stack to produce a ribbon like microfibril, and additional stacking of triplet subunits produces microfibrils of larger widths, but the thickness remains the same. Typically BC obtained by the *G.xylium* have a rectangular cross-section (6–10 nm by 30–50 nm), a high crystallinity, and a high fraction of Ia crystal structure [20, 54]. Through the further researches on biosynthesis of cellulose by *G. xylinus*, it was proposed that BC biosynthesis system was composed of bcs or acs and cdg operons, which are responsible for cellulose synthesis and its activation, respectively [89, 90]. The bcs operon is constructed of bcsA, bcsB, bcsC and bcsD. BcsA is speculated to play a role in the polymerization of uridine diphosphate glucose (UDP-Glc) (Figure 6); bcsB a binding subunit of cyclic di-guanosine monophosphate (c-di-GMP), that is an activator of cellulose synthesis [91]. The bcsC and bcsD are thought to be located on the outer membrane, playing roles in the crystallization and/or extrusion of cellulose. The acs operon is consisted of acsAB, acsC and acsD, and their translation subunits are thought to be similar to those of the bcs operon.

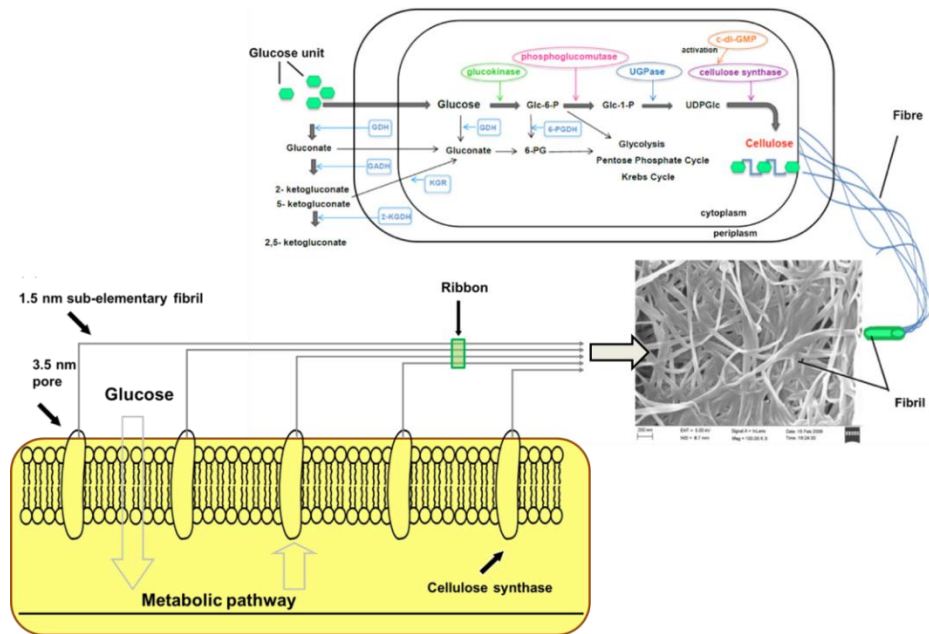


Figure 2-6. Schematic images of the major metabolic pathways of *G. xylinum* and the assembly of cellulose molecules into nanoribbon (Modified from [92] and [93]).

Up to date, three types of cdg operon have been found. The cdg1 operon is composed of pdeA1 and dgc1, with two unknown open reading frames. PdeA1 is phosphodiesterase A, and degrades cdi-GMP. Dgc1 is a di-guanilate cyclase which synthesizes c-di-GMP. Besides these operons, there are several genes for BC production, such as CMCase, β -glucosidase and ORF2 [92, 93]. Despite the above researches, the metabolic pathways of BC production remain unclear.

2.2.3. Factors affecting the production capacity of BC

There are many factors influencing the morphology of the cellulose network and the production rate of cellulose [54]. Oxygen is one of the important factors that influence on the rate and yield of cellulose production. When oxygen tension is greater than 40%, growth rate of *G. xylinus* and production rate of cellulose are higher as compared to the bacteria cultured at condition of 15% oxygen tension. Oxygen tension also affect to the branching of the cellulose network. When the oxygen tension is about 50%, a denser cellulose network is produced compared to cellulose network produced at lower oxygen tension [96].

The thickness of the cellulose is only affected by the branching of the network. Prior to cell division, the cellulose-synthesizing complexes are doubled and activated after division. Cellulose ribbon don't be broken at that time, just create a branching point [81].

The degree of polymerization (DP) of BC is around 2000-4000 and the cultivation conditions can influence on the DP of the cellulose. In a static culture, the DP of the cellulose produced is higher than for cellulose produced in an agitated culture. The decrease in DP, in case of agitated condition, due to an increase in the activity of endoglucanases which can have an effect on decreased DP [96].

The pH also should be concerned for cellulose production. The optimized pH for BC production is between pH 4 and 5. When the bacteria are cultured under pH3.5, cellulose is not produced and the proliferation of the bacteria is negatively affected [97].

The components of the medium also give a significant effect on BC production. The addition of lactate to the medium increases the cellulose production because it is associated with the TCA cycle. Extra energy source (ATP) generated by lactate increases the concentration of bacteria and BC production [54].

The oxidation of ethanol can affect the BC production in the similar way such as lactate. However the efficiency is smaller than using a lactate. In addition ethanol in high concentrations can kill the bacteria [98].

The concentration of the carbon source could also affect the rate of cellulose synthesis. An optimal level of carbon source exists because the utilization of the carbon source decreases when too high concentration of

carbon source is used [99].

The cellulose production is also affected by the production of acetan and levan which are water soluble polysaccharides. When sucrose is used a lot of water soluble polysaccharides are produced. However, in case of glucose medium only small amount of water soluble polysaccharides are produced. Therefore, glucose is the most appropriate source for production of BC [54].

2.2.4. Productivity of BC

It has been known that the limits of bacterial cellulose related to the industrial scale are the yield and rate of the bioprocess. A study was conducted to compare the productivity of cellulose from plants and bacteria [83]. In the research, productivity of cellulose from plants was about 80 ton of cellulose/ha with 7 years from planting to cultivation and yielding 45 % cellulose contents. The research group suggests that the same yield could be achieved with microorganisms to estimate yield of 15 g/L in 50 h of culture in a 500 m³ sized bioreactor in 22 days. The productivity of cellulose from bacteria is more efficient. Also, cellulose from bacteria is more pure and ecologically sustainable comparing to plant cellulose. Especially look up to consider the process for obtaining cellulose nanofibers from the pulp, BC is a much more efficient way since BC is synthesized to cellulose nanofibers from in the first place [53].

Biosynthesized cellulose by bacteria fermentations offers some

advantages compared with the plants celluloses. 1) BC is not dependent on regional and climatic conditions, 2) Microorganisms growth rate can be controlled to produce BC, 3) Cellulose produced by microorganisms contains no lignin or other contaminants so that the additional energy consumption to remove impurities can be avoided, 4) Microorganisms can be genetically modified to produce BC with desired properties, and 5) Agro-industrial wastes can be repeatedly used as a growth medium. To establish favorable production yields and costs, attention needs to know about the species and genetic modification of the bacteria used and the type of reactor for the production process [53].

2.2.4.1. The species and genetic modification of bacteria

There are many species of bacteria that have produced extracellular cellulose, including those in the genera of *Acetobacter*, *Achromobacter*, *Aerobacter*, *Agrobacterium*, *Azotobacter*, *Escherichia*, *Rhizobium*, *Salmonella*, and *Sarcina ventriculi*. Among them, *Acetobacter xylinus* is extensively utilized for research and commercial production of cellulose, recently. Other genetically modified bacteria can produce cellulose with the high quality and yield [83]. For example, De Wulf et al. obtained a ketogluconate by UV mutagenesis. It is non-producing mutant from its parent strain, such that cellulose production increased from 1.8 g/L to 3.3 g/L after 10 days of shaking culture [100]. Another novel method to increase the bacterial cellulose production yield from a *Gluconoacetobacter xylinus* strain was the

mutagenesis caused by high hydrostatic pressure treatment. The yield increased from 106.03 g/L to 158.56 g/L (in the wet state) [101].

2.2.4.2. Types of reactors for the production process

The traditional reactors used for the cellulose production process involve the shake flasks and stirred tanks, but these agitated methods have a potential for mutation of the bacterial strain [102].

Another concern of them is that bacterial cellulose can easily attach on the shaft of reactors, making it hard to collect the product and clean up the reactors [103]. Recently, some effective culture reactors have been designed and used for cellulose production under agitated conditions. Among them, the spherical type bubble column bioreactor [104], air-lift reactor [105], and modified air-lift reactor are most well-known [106] (figure 2-7).

On the other hand, some of reactors, involving the rotary discs reactor, rotary biofilm contactor, aerosol bioreactor, membrane bioreactor and Horizontal Lift Reactor (HoLiR) keep the fermentation process under relatively static conditions to produce bacterial cellulose in the form of sheets and membranes. With rotary discs reactors, an 86.78 % greater yield of cellulose than by using traditional static fermentation can be achieved. In fact, Yong-Jun Kim et al. reported that a yield of BC 6.17 g/L could be attained by using rotary biofilm contactor [107]. Nevertheless it has not been possible to increase the BC

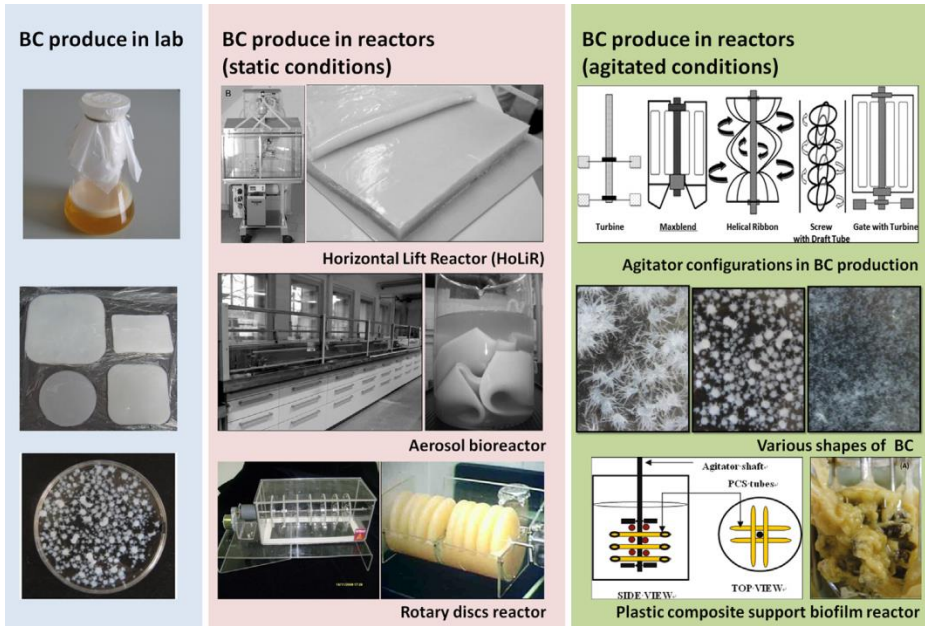


Figure 2-7. BC produced under static and agitated conditions [81].

yield to a satisfactory level. So further improving the yield and lowering the cost for commercial mass production of BC is a challenging goal, which requires further persistent hard work.

2.2.5. Characteristic differences between the plant cellulose and BC

Bacterial cellulose (BC) synthesized by some bacterial strains, has the same chemical structure as plant cellulose composed of linear β -D-glucose unit linked by 1-4 glycosidic bonds (Figure 2-8). However, between BC and plant cellulose, there are a number of differences are existed in the physical and chemical properties (Figure 2-9). The first is its high purity. Unlike the plant cellulose (60~70 % cellulose content) which normally has impurities such as lignin, hemicellulose, and pectin, BC possesses higher chemical purity without any other polymers. As a result, BC does not require extra process to remove these impurities. The second is its high water absorbing property. BC pellicle is produced as a hydrogel form and BCs' water holding capacity (up to 98.5 %) is higher than plant cellulose (up to 60 %). The third is its excellent mechanical property. BC possesses a unique 3D porous network structure, which consists of random assembly of ribbon shaped cellulose fibrils. A diameter of the fibrils is between 20 and 50 nm, containing a bundle of much thinner fibrils. The fibrillar structures provide high mechanical properties. The Young's modulus of single BC filament was measured by a raman spectroscopic technique was 114 GPa, which is higher than those of MFC and MCC [108]. Also, through the AFM, Young's modulus of BC fiber was

reported that 78 ± 17 GPa [109]. The Young's modulus of BC sheets was 15 GPa [110]. The fourth is its high crystallinity. The crystallinity of BC is up to 80 % which is higher than plant cellulose (50~65 %). The fifth is its high thermal stability comparing to plant cellulose. Due to its high crystallinity and purity, BC can be a good material as a thermal stabilizer. The sixth is its unique 3D-networked highly porous structure and controllable shape. The diameters of pores in BC range from several tens to several hundred nanometers, the shape of BC can be easily depending on shapes of the culture dishes [111].

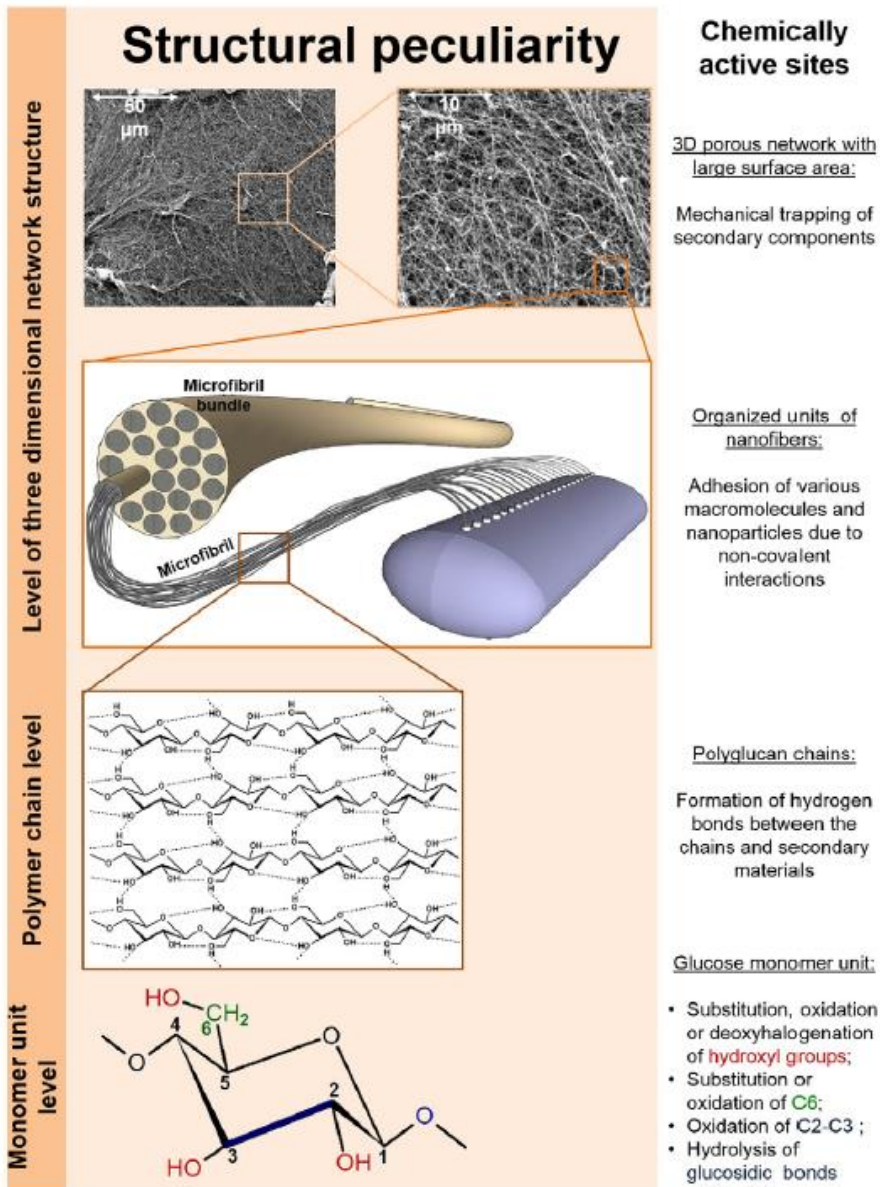
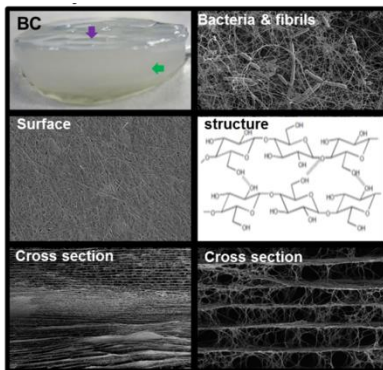


Figure 2-8. General overview of bacterial cellulose structural organization [110].



-
1. High purity
 2. High degree of crystallinity
 3. High tensile strength
 4. High absorbancy
 5. High water binding capacity
 6. High elasticity, resilience, and durability
 7. Nontoxicity
 8. Biocompatibility
 9. Good shape retention
-

Figure 2-9. Unique structures and properties of bacterial cellulose.

2.2.6. Applications of BC

To date, there have been numerous reports on the synthesis of BC composites with functional materials to prepare functional nanocomposites. These functional materials could be divided into a range from nanoparticles to bulk polymers. The BC composites have been widely used in various applications including clothes, food, cosmetics, electronics and biomedical field. There are some examples of BC composites that have led to improvements in physicomechanical properties, biomedical applications, and conducting capabilities of BC.

2.2.6.1. Composites with high mechanical strength

BC nanocomposites with high mechanical properties have potential applications in a various industries. BC composite with pulp significantly enhanced the strength and fire resistance properties of the pure paper sheets. Thus, these composites could be a good candidate in the quality paper fields [113]. Nanocomposites with improved properties based on PLA matrix and BC were reported [114]. Acetylated BC was mixed with melting PLA. The acetylation of BC increases its compatibility and adhesion with the PLA matrix. PLA-BC nanocomposites have considerably improved mechanical properties as evidenced by the significant increase both in the Young's modulus and in the tensile strength. The preparation and characterization of chitosan (CH) and BC nanocomposite films were described [115]. The

purpose of CH-BC films is improved mechanical properties while keeping their thermal stability and transparency. Novel pullulan-BC (PBC) nanocomposite films were reported [116]. The incorporation of BC nanofibers into the pullulan matrix improves considerably both Young's modulus and tensile strength. The mechanical properties of phenolic resin/BC composites were studied. It was found that BC composites are stronger than MFC composites. BC nanocomposites with acrylic resins were transparent and had great potential for utilization in optoelectronic devices [117].

2.2.6.2. Separation and waste purifications

BC has the potential to be used as a membrane for purification or separation. BC composite with acrylic acid (AAc) was prepared for ion exchange. The BC-AAc composite membranes possessed excellent absorption capability for heavy metals [118]. BC molecularly imprinted polymers (MIP) composite membranes were developed for the separation of S-propranolol enantiomer. The composites were successfully utilized for enantioselective separation [119]. BC and MIP composite membrane have great potential for application as a transdermal enantioselective system for racemic propranolol [119].

2.2.6.3. Conducting materials and electrical devices

BC, non-conducting in nature, could be converted to electrically conductive materials by incorporation of some conductive materials. The

MWCNTs-BC was prepared by dipping a BC pellicle in an aqueous MWCNT dispersion containing a CTAB surfactant [120]. Recently, the polyaniline (PANI)/BC and polypyrrole (PPy)/BC composites have been intensively studied [121, 122]. The resulting nanocomposites had higher bulk conductivity. These types of nanocomposites has potential applications in biosensors, flexible electrodes, flexible displays, platform substrates to evaluate the effects of electrical signals on cell activity, and to guide desired cell function for tissue engineering applications [121, 123].

Organic light emitting diode (OLED) devices based on flexible BC substrate have been reported [124]. Moreover, OLED displays based on cellulose and acrylic resin nanocomposite was successfully fabricated. These devices are useful in numerous applications including e-newspapers, e-book, dynamic wall papers, and learning tools [125]. BC composite with graphene oxide (BC-GO) greatly enhanced the conducting properties while imparting increased mechanical properties. The flexible and electrically conductive BC-GO composite film with striking mechanical properties is a candidate for advanced biochemical and electrochemical devices [126]. Potential applications of BC for fuel cells have been studied [127]. They found that BC possesses reducing groups capable of catalyzing the precipitation of palladium from aqueous solution. Their experiments showed that palladium-BC can catalyze the generation of hydrogen when incubated with sodium dithionite and can generate an electrical current from hydrogen. This technique may be

available in fuel cell development.

AuNPs are used in electronics, sensors, catalysis, and several related fields. BC-Au composites using BC nanofibers as biotemplates were used for the construction of H₂O₂ biosensors [80].

2.2.6.4. Biomedical applications

Application of BC in the biomedical field have been gaining relevance in the last years [128]. BC is widely used as a dressing material in medical fields. BC composites with polymeric or nonpolymeric compounds were prepared to impart antimicrobial and biocompatible properties in BC. BC-Chitosan composites increased the cell adhesion and proliferation properties with antibacterial effect. BC/Chitosan can be applied to the treatment of skin ulcers, bedsores, burns, and wounds dressing [129]. BC-gelatin composites produced similar effects during cell adhesion and proliferation. Fibroblast cells showed definite adhesion and proliferation when incubated with BC-gelatin composite for 48 h. The composite biocompatibility was much better than that of pure BC. Accordingly, the prepared BC-gelatin scaffolds are bioactive, indicating that they can be used for wound dressing and as tissue engineering scaffolds [80]. Tissue replacement through newly developed biomaterials is an important aspect of the present advances in biomedical fields. However, the replacement materials should possess mechanical properties equivalent to those of body tissues. BC composites with polyvinyl alcohol were prepared

for development of such biomaterial devices that could replace the tissue [131]. BC/collagen composites were synthesized for potential tissue engineering applications through an *in situ* composite synthesis strategy. The high biodegradability, low antigenicity and cell-binding properties of collagen are important characteristics for a biomaterial from a medical point of view [129]. BC/polyethylene glycol (PEG) composite prepared by immersing wet BC pellicle in PEG aqueous solution was reported [132]. These novel BC/PEG scaffolds showed the potentiality to be used for wound dressing or tissue engineering applications. Similar strategy was developed for BC in presence of alginate, and the BC/alginate hybrid matrix is able to increase 3 times the load of the anticancer drug doxorubicin and the device showed molecular controlled release of the load [133].

2.2.6.5. Food applications

BC is hydrogels and its rheological properties have led to uses in the food application as gel called Nata de coco which is eaten as a healthy dietary dessert. Similarly, a cellulose synthesized in black or green tea containing sucrose named Kombucha. After a period of two-weeks, the cellulose membrane on surface is removal and the liquid phase ready to drink. Additionally, BC can be used as thickening agent, stabilizing agent, gelling agent in some foods [83].

Food packaging is another application of BC composites. Addition of BC

fibers in starch and PLA film increased thermoresistance, transparency and reduces diffusibility of gases and water sensitivity [134, 135].

Chapter 3

**Electromagnetic BC nanocomposite using
magnetite nanoclusters and polyaniline**

3.1. Introduction

Since electromagnetic interference (EMI) induced by electric and magnetic fields causes energy losses and bad effects on human health, EMI shielding materials have attracted attention recently. It is known that conducting materials can effectively shield electromagnetic waves, while electromagnetic waves generated from a magnetic source, particularly at low frequencies, can only be effectively shielded by magnetic materials [136]. Thus, a composite of a conducting polymer and magnetic material used as an EMI shielding material can have excellent shielding effectiveness for various electromagnetic sources. However, it is critical to develop reinforced composites due to the relatively poor mechanical properties of conductive polymers [121, 137-141]. Bacterial cellulose (BC) provides an ultrafine nanosized 3D network fibrous structure that could serve as a potential reinforcing matrix of composites.

In this chapter, electromagnetic BC composites were synthesized using magnetite nanoparticles (MNPs) and polyaniline. In biosynthesis method, nanoparticles are dispersed in the culture medium to produce BC composites. In this case, it is important to consider dispersibility and the size of particles because non-dispersed particles make it difficult to obtain uniform composite and too small particles about smaller than tens of nanometer sized nanoparticles may come out through the space between BC 3D-network. For preparing electromagnetic composite, magnetic BC was synthesized firstly.

After synthesizing magnetic BC composites previously, a conductive polymer was synthesized at the surface of the BC fiber. At that time, magnetic nanoparticles should be placed between the networks of BC fibers. Therefore the biosynthesis method was chosen for preparing electromagnetic composite. In this process, MNP clusters uniformly dispersed with about 200 nm size using amphipathic polymer. Subsequently, PANi was synthesized on the magnetic BC fibers by chemical oxidative polymerization (Figure 3-1).

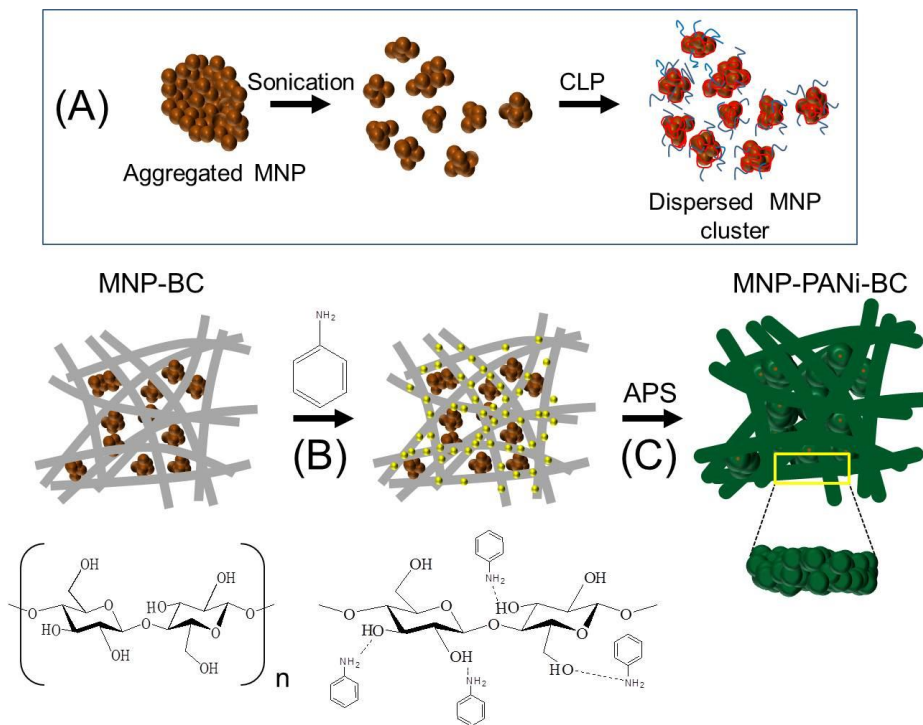


Figure 3-1. Preparation of electromagnetic BC nanocomposites. (A) Dispersion mechanism of MNPs using CLP stabilizer, (B) addition of aniline to BC membrane, and (C) oxidative polymerization by ammonium persulfate.

3.2. Materials and method

3.2.1. Preparation of highly dispersive magnetite nanoparticles (MNPs)

A comb-like polymer (CLP) as a polymer surfactant was synthesized via free radical polymerization as previously described. Methyl methacrylate (MMA, Sigma Aldrich), poly(ethylene glycol) methacrylate (Sigma Aldrich, Mn 360 g/mol, n = 6), poly(ethylene glycol) methyl ether methacrylate (Sigma Aldrich, Mn 475 g/mol, n = 9) and azoisobutyronitrile initiator (AIBN, Samchun Chemical) were dissolved in 500 mL tetrahydrofuran (THF, Sigma Aldrich), and poured into a four-neck round-bottom flask. The mixture was polymerized for 18 hours at 70 °C with vigorous stirring. The resulting polymer was purified by three precipitations in 8:1 (v/v) petroleum ether/methanol (Sigma Aldrich) and dried in a vacuum drying oven at 40 °C for 24 h.

MNPs were prepared by a coprecipitation method. First, 0.2 mol $\text{FeCl}_2 \cdot 4\text{H}_2\text{O}$ (99 %; Sigma Aldrich) and 0.4 mol $\text{FeCl}_3 \cdot 6\text{H}_2\text{O}$ (98 %; Aldrich) were dissolved in 10 mL deionized water. This solution was added drop-wise to an aqueous solution of ammonium hydroxide (28 %; Duksan) with vigorous stirring. The precipitated MNPs were washed three times with deionized water by centrifugation and sonication. The washed MNPs were dispersed using CLP solutions with different concentrations.

3.2.2. Biosynthesis of MNP-incorporated BC (MNP-BC) nanocomposites

G. xylinus (KCCM 40216) was obtained from the Korean Culture Center of Microorganisms. The bacteria were cultured on a mannitol medium composed of 2.5 % (w/w) mannitol, 0.5 % (w/w) yeast extract, and 0.3 % (w/w) Bacto Peptone. The culture media were sterilized in an autoclave at 120 °C for 20 min. A single *G. xylinus* colony grown on agar culture medium was transferred to a Petri dish filled with liquid mannitol medium and incubated for one day to create a cell suspension. Then, the cell suspension was introduced into the MNP-dispersed culture medium at 28 °C and incubated for five days. The MNP-incorporated BC (MNP-BC) membrane that was biosynthesized in the medium was purified by 1 wt% sodium hydroxide for 24 h at room temperature. Subsequently, the membrane was washed repeatedly with distilled water until its pH was 7.0 and then stored in distilled water.

3.2.3. Polymerization of polyaniline (PANi) on the MNP-BC (PANi-MNP-BC) nanocomposites

Aniline (Sigma Aldrich) was added to 50 mL of 1 N HCl solution containing 0.1 g of BC and MNP-BC membranes. Then, the solution was stirred for 10 min to enable the aniline monomer to disperse well within the BC membrane. Next, 0.2 mol of ammonium persulfate (APS; Duksan Pure

Chemical) as the oxidant was added to the solution for polymerization. The polymerization of aniline was carried out at 4 °C for 2 h. After polymerization, the composites were purified by a methanol, distilled water and HCl solution.

3.2.4. Characterizations of nanocomposites

The polymer compositions were characterized by nuclear magnetic resonance spectrometry (¹H-NMR; 500 MHz, Avance 500, Bruker) using deuterated acetone. The molecular weights (M_w) of the polymers were determined by gel-permeation chromatography [GPC; KF 804 column, intelligent refractive index detector (RI930), intelligent HPLC pump (PU980), Jasco]. The long-term stability of the MNP suspensions was characterized by measuring the optical density at 350 nm (OD₃₅₀) of tightly sealed samples in a single cuvette using an Optizen 2120UV UV-VIS spectrophotometer (Mecasys Co.). The chemical structures of the samples were characterized by Fourier transform infrared spectroscopy (FTIR; M2000; Midac, Hamamatsu) from 4000 to 400 cm⁻¹ using powdered samples pressed into KBr pellets. The surface morphologies of the samples were observed at an acceleration voltage of 5 kV using field emission scanning electron microscopy (FE-SEM; JSM-6330F, JEOL). Thermal degradation of the samples was measured by thermogravimetric analysis (TGA; TGA Q5000, TA Instruments). The degree of magnetization in the samples was measured with a superconducting quantum interference device (SQUID)-based magnetometer (MPMS-XL; Quantum Design). The electrical conductivity of the samples was measured

by a four-probe technique with a picoammeter containing an internal voltage source (2400 Source Meter, Keithley).

3.3. Results and discussion

3.3.1. Enhancement of the colloidal stability of MNP solutions

The stable dispersion of MNPs in an aqueous solution is critical for practical applications due to their strong tendency to aggregate. We used a polymeric surfactant of amphiphilic CLP based on an MMA backbone for the dispersion of MNPs (Figure 3-2A). The CLP was characterized by ¹H-NMR to confirm its chemical composition. The composition ratio of MMA:HPOEM:POEM was determined to be 4:1:1 by comparing the specific peaks in the spectra, and the *M_w* as measured by GPC was 45,000 (polydispersity index = 2.73).

In Figure 3-2A, MNPs are temporarily untangled by mild sonication and form nanoclusters in aqueous solution. The attachment of CLP molecules to MNP nanoclusters enables long-term stability of the colloidal dispersion because the hydrophilic side chains are released freely into the aqueous environment, thereby impeding the aggregation of the MNPs. The CLP-modified MNP solutions maintained their well-dispersed state for a long time due to the repulsive interactions among the polymer-decorated particles. All MNP solutions (10 mg/mL) prepared with different concentrations of CLP were well dispersed initially after sonication. However, visible aggregation

was observed after one week in the MNP solutions prepared with 2-8 mg/mL CLP. On the other hand, MNPs dispersed in CLP solutions over 10 mg/mL maintained their colloidal stability for two weeks (Figure 3-2B). Figure 3-2C was filtration result of MNP solution and CLP-modified MNP solution. After mild sonication, each solution was filtered using a 0.8 μm pore sized syringe filters. The MNPs in no CLP solution was almost filtered and the color of filtered solution was transparent pale yellow. But, the MNPs in the CLP-MNPs solution could pass through the filter and the color of the filtered solution was same as the initial solution. The distinct difference in colloidal stability was clearly indicated by relative UV absorbance, as shown in Figure 3-2D. The solution of unmodified MNPs showed rapid aggregation in one day, while MNPs modified with a CLP solution (10 mg/mL) showed good colloidal stability for a long period. For successful fabrication of BC membranes embedded with MNP clusters, the MNP clusters should be sufficiently dispersed during the incubation and embedding processes.

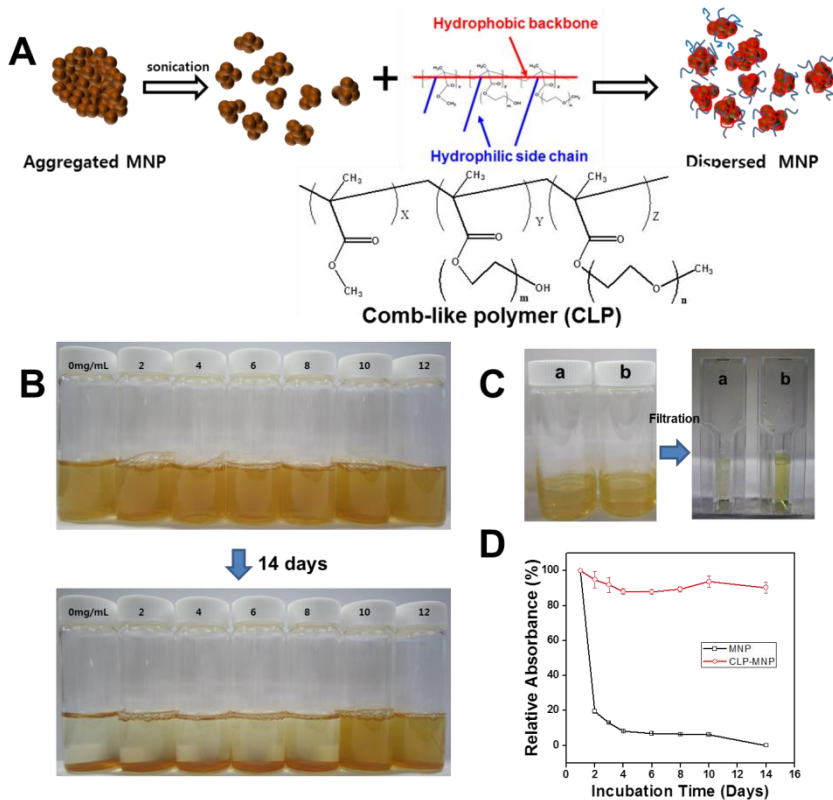


Figure 3-2. (A) Dispersion mechanism of MNP using CLP stabilizer, (B) Optical images of an aqueous MNPs solution at different concentration of CLP, (C) Filtration test of (a) MNP solution and (b) CLP-modified MNP solution, and (D) Relative UV absorbance of MNP and CLP-MNP solution as a function of storage time (SD, n=5).

3.3.2. Biosynthesis of MNP-BC nanocomposites

The pre-cultured bacterial cell suspension was introduced into a culture medium containing CLP-MNPs and incubated under static conditions for five days. As shown in Figure 3-3B, yellow BC pellicles formed and were compared with BC pellicles biosynthesized in the culture medium without MNPs (Figure 3-3A).

For successful fabrication of BC membranes embedded with MNP clusters, the MNP clusters should be sufficiently dispersed during the incubation and embedding processes. The hydrophobic MMA backbone of CLP can be chemophysically attached to the surface of MNP clusters and the hydrophilic side chains can be released freely toward the aqueous solution. This approach is advantageous over other methods because it is nontoxic and can minimize damage to the inherent properties of the nanoparticles. The hydrophobic MMA backbone of CLP can be chemophysically attached to the surface of MNP clusters and the hydrophilic side chains can be released freely toward the aqueous solution. This approach is advantageous over other methods because it is nontoxic and can minimize damage to the inherent properties of the nanoparticles.

The morphologies of the MNP-BC composites were investigated using FE-SEM. Figure 3-4A shows the FE-SEM image of BC membrane surface. The BC membrane consists of nanofibers with diameters ranging from 10 to 50 nm, which forms an ultrafine network structure. Figure 3-4B shows MNP-

BC cultured in an unmodified MNP solution. The MNPs tended to aggregate rapidly in an aqueous solution and large MNP aggregates were adsorbed on the surface of the BC fibers. In contrast, MNP clusters cultured with CLP-MNP were tightly embedded in a BC nanofiber network like a “fishing net”. Figure 3-4C shows FE-SEM images of MNP-BC composites incubated in a medium containing CLP-MNP; MNP clusters 200 nm in size were tightly bound inside the BC network, creating a porous 3D structure.

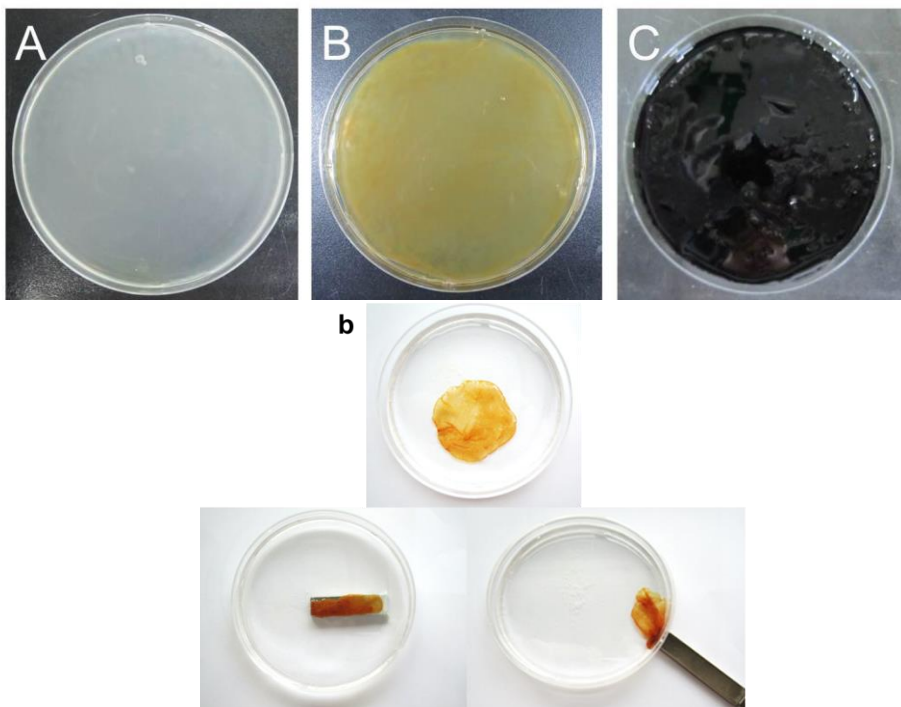


Figure 3-3. Optical images of (A) pure BC, (B) MNP-BC, and (C) PANi-MNP-BC. (b) is optical images for showing the magnetic property of MNP-BC using a magnetic bar.

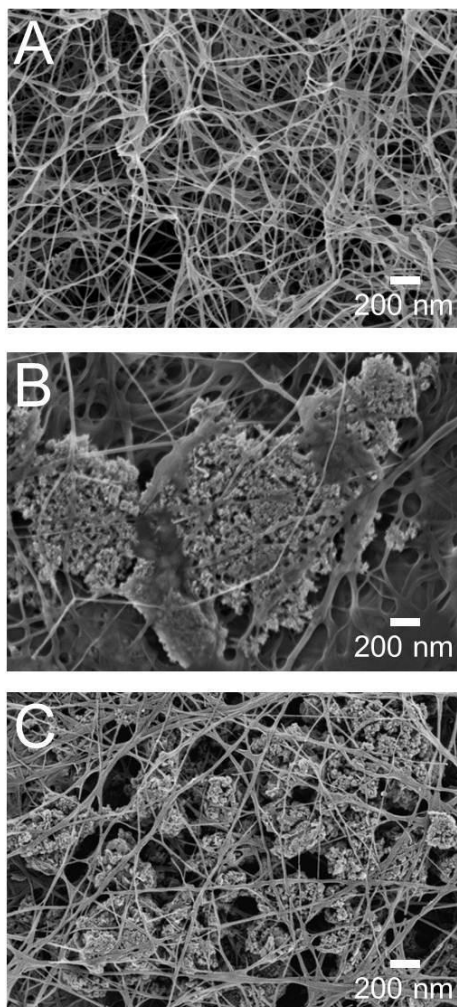


Figure 3-4. SEM images of (A) pure BC, (B) MNP-BC without CLP and (C) MNP-BC with CLP.

3.3.3. Synthesis of PANi-MNP-BC nanocomposites

The surface of the BC “fishing net” was used as a template for the synthesis of conductive polymers. Using the surface of BC fibers as polymerization sites, PANi nanoparticles were created, forming a 3D network (Figure 3-5). The SEM images show that MNP nanoclusters are embedded well in the bacterial cellulose enabling the uniform coverage of PANi in the nanofibrous membrane without the development of surface roughness during the polymerization of PANi. The hydrogen bonds between the hydroxyl groups of BC and the amine groups of aniline might serve as a traction force to assist the growth of continuous PANi fibers over cellulose and to help prevent aggregate formation [121, 123]. We found that the nanofibers acted as a suitable template for polymerization.

The aniline was able to permeate through the inner structure of the BC membranes. At the same time, the hydroxyl groups of the BC molecules were able to interact with the amine groups of aniline to form hydrogen bonds. Right after the oxidant solution was added, PANi was polymerized on the fibers of BC and some of the PANi particles were adsorbed on the MNPs, as illustrated in Figure 3-1B and C. As shown in Figure 3-3C, the PANi on the BC showed a characteristic dark green, verifying the successful polymerization of the aniline monomers.

A strong peak at 3410 cm^{-1} arose from the stretching of hydroxyl groups in BC [19]. The peaks at 2900 cm^{-1} originated from C-H stretching and the

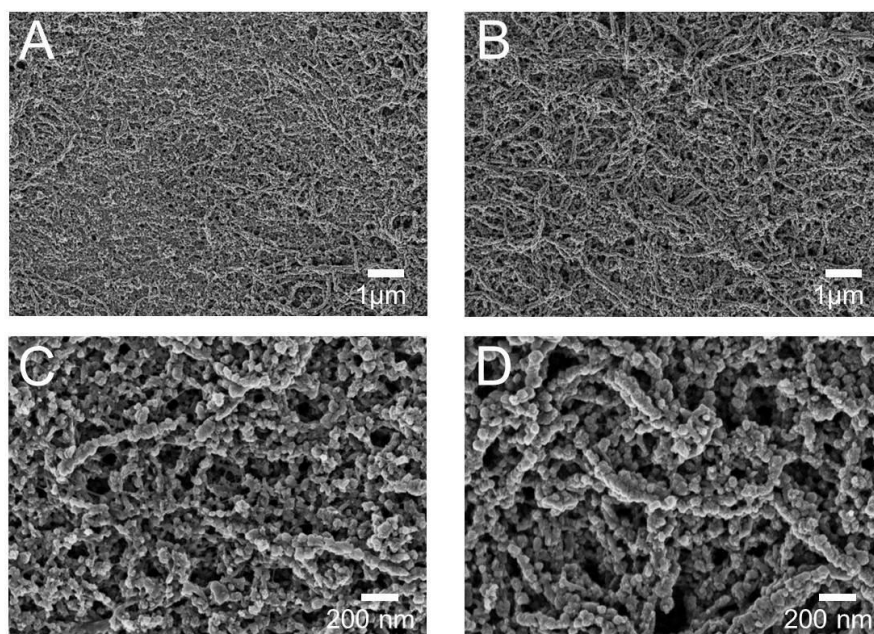


Figure 3-5. SEM images of (A) PANi-BC and (B) PANi-MNP-BC, (C) magnified image of A and, (D) magnified image of B.

peak at 1372 cm^{-1} is attributed to the O-H bending (Figure 3-6). The peak at 1157 cm^{-1} corresponds to the C-O asymmetric bridge stretching. The strong peak at 1060 cm^{-1} was due to the C-O-C pyranose ring skeletal vibration. The characteristic peak of pure PANi appears at 803 cm^{-1} , corresponding to the out-of-plane bending vibration of the C-H band of the p-disubstituted benzene ring [142]. Peaks at 1121 and 1294 cm^{-1} due to the stretching of the C-N band and vibration of C-H in the benzene ring, respectively, were also observed (Figure 3-6). The peaks around 1486 and 1578 cm^{-1} are assigned to the stretching vibrations of N-B-N and N=Q=N structures, respectively (B and Q represent benzenoid and quinoid moieties in the PANi chains) [24]. Compared with the spectra of MNP-BC, it was found that the absorption peak at 3410 cm^{-1} in the spectrum of BC was shifted to 3350 cm^{-1} in the spectrum of the PANi-MNP-BC composite. The shift resulted from the activation of BC by acids and cleavage of intermolecular hydrogen bonds [121]. This implies that more hydroxyl groups became accessible, enabling the uniform dispersion of PANi in the nanofibrous membrane. Overall, the intensity of the characteristic absorption peaks in BC became weaker with the introduction of PANi on the BC surface, confirming the complete surface coverage.

Figure 3-7 shows the TGA curve of the BC, MNP-BC, PANi-BC and PANi-MNP-BC. TGA can be used to characterize the weight change upon heating and to detect the phase changes due to decomposition processes. The BC underwent one main degradation at about $342\text{ }^{\circ}\text{C}$, apart from a minor

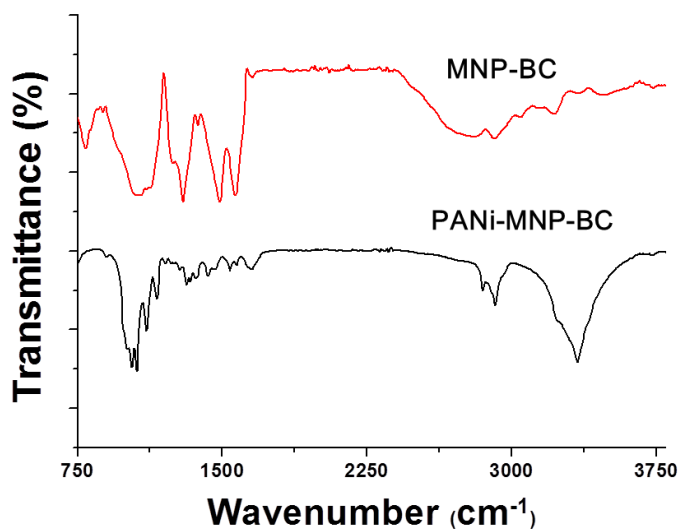


Figure 3-6. FT-IR spectra of (A) BC and (B) PANi-MNP-BC.

mass loss at about 100 °C, which can be attributed to water evaporation. Thermal degradation of the MNP-BC occurred at 100 °C and 341 °C, as for BC alone. However, since MNPs have high thermal stability, its weight loss was smaller than that of BC. The PANi-BC composite also showed first-stage weight loss at 100 °C and second-stage weight loss at 216 °C due to the BC, impurities, or polyaniline side chains. This resulted from the weaker inter- and intramolecular hydrogen bonding of BC in the PANi-BC. The third weight loss stage was evident at 340 °C and was due to the thermal-oxidative degradation of the main polyaniline chains. The PANi-MNP-BC degraded at 273 °C due to the same reasons as for PANi-BC, showing the best thermal stability among the samples.

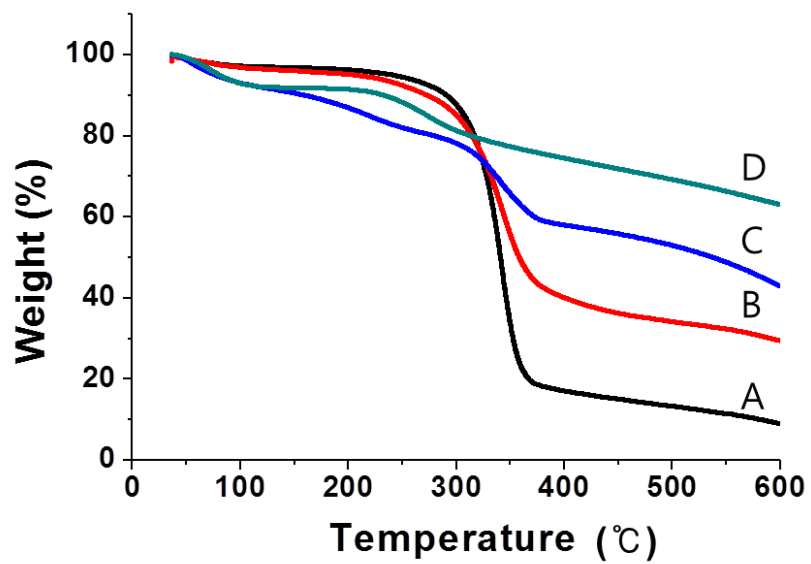


Figure 3-7. TGA curves of (A) BC, (B) MNP-BC, (C) PANi-BC and (D) PANi-MNP-BC.

3.3.4. Electromagnetic properties of nanocomposites

To investigate the magnetic behavior of the nanocomposites, magnetization measurements were taken using SQUID. Figure 3-8 shows the hysteresis curves obtained with the nanocomposites. The saturation magnetizations of MNP, MNP-BC and PANi-MNP-BC as determined by the hysteresis loops were 10 emu/g, 8.4 emu/g and 2 emu/g, respectively, which confirmed the characteristic superparamagnetic properties of the MNPs. As the magnetic field decreased, the degree of magnetization decreased to zero and the saturation magnetizations of MNP-BC and PANi-MNP-BC showed the same characteristic superparamagnetic properties as MNP. The electrical conductivities of PANi-BC and PANi-MNP-BC were 0.31 S/cm and 0.43 S/cm, respectively, whereas BC was insulating. The increase in conductivity with PANi-MNP-BC resulted from the MNPs connecting the BC fibers coated with the conducting polymer, PANi.

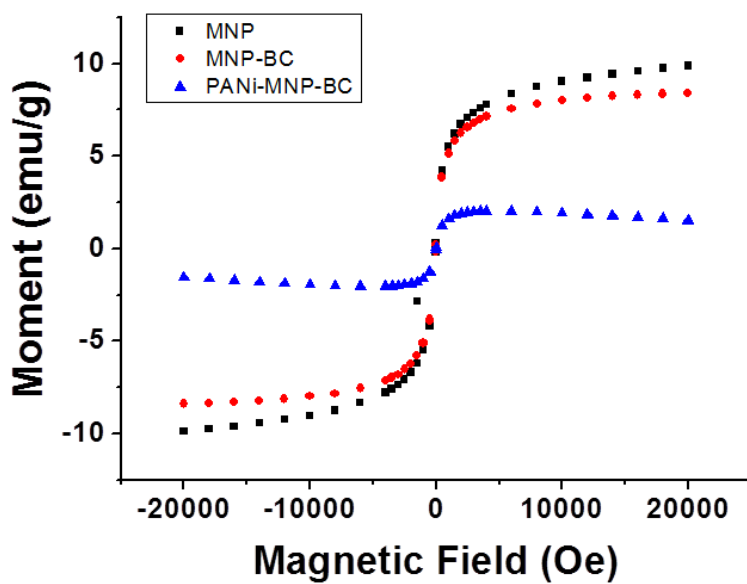


Figure 3-8. Magnetic hysteresis curves of BC nanocomposites.

3.4. Summary

The amphiphilic polymer surfactant was effective in increasing the colloidal stability of magnetic nanoparticle clusters for a long period. Magnetic BC was biosynthesized by culturing *Gluconacetobacter xylinus* in a medium containing well-dispersed MNPs. Conductive and magnetic BC was synthesized by the chemical oxidative polymerization of aniline on the BC fibers with MNPs, which were embedded in the networked fiber structure. BC fibers were fully coated with PANi particles and the introduction of MNPs and PANi enhanced the thermal stability of the composites. Magnetic and electrical measurements confirmed that the PANi-MNP-BC composite is electromagnetic and can be a potential shielding material.

Chapter 4

**Flexible conductive BC combined with
silicon nanoparticles and polyaniline**

4.1. Introduction

Lithium ion batteries (LIBs) are one of the most promising systems for energy storage. [143, 144]. Due to increasing demand for LIBs with low cost, high energy density and long cycle life, the development of new materials with high performance is required [145, 146]. The energy density of LIBs is able to be improved by replacing the graphitic carbonaceous anode with advanced anode materials which yield much higher capacities.

Silicon is a very promising anode material for Li-ion rechargeable batteries because its specific capacity is higher than that of graphite [147-149]. However, silicon has poor conductivity and exhibits significant volume expansion upon Li-ion insertion, and these properties have restricted its application in anode materials [150, 151]. Recently, major efforts have been undertaken to address the conductivity problems of SiNPs using conducting polymers [152-154]. PANi is a popular option for increasing the conductivity of anode materials because it is chemically stable, lightweight and easy to synthesize. However, PANi is brittle and therefore cannot be used in applications like flexible batteries [155, 156]. The fracture of electrodes can be prevented by introducing a flexible supporting matrix, which can dissipate stresses around the structure. A three-dimensionally networked fibrous structure can provide both flexibility and stress dissipation. BC can be a good supporting matrix for flexible conductive composites because of its unique 3D-networked structure and high mechanical and flexible properties [24, 157,

158].

In this part, dipping method was used for synthesis Si/BC composite. Biosynthesis method has a drawback that the silica nanoparticles (SiNPs) could melt during the purification process using NaOH. *In situ* method for synthesis SiNPs is difficult and has harsh condition. However, dipping method is very simple and gives less damage to BC unlike the biosynthesis or *in situ* method. In addition, SiNPs can be introduced into the BC network due to its size about 100nm. Therefore, dipping method was chosen for introduction of silicon nanoparticles (SiNPs) to BC network structure and the conformal coating of polyaniline (PANi) to the SiNPs-bound BC composites (Si-BC) for application in flexible electrode of LIBs (Figure 4-1).

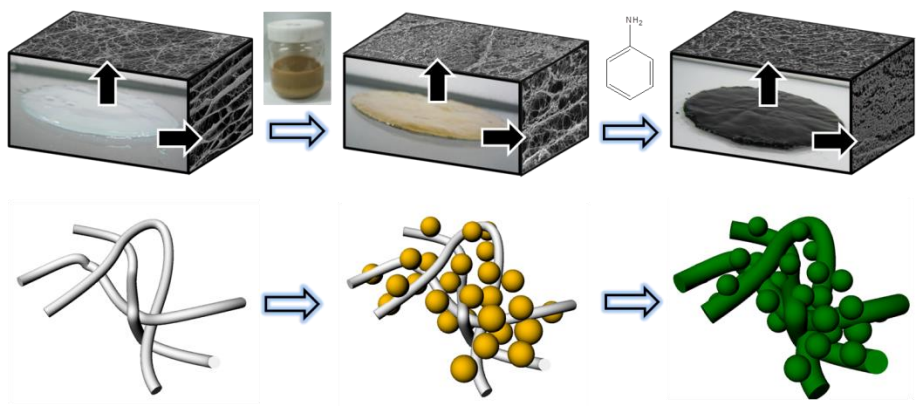


Figure 4-1. Schematic representation of the process for preparing PANi-Si-BC composite.

4.2. Materials and method

4.2.1. Preparation of the silicon nanoparticle-embedded BC (Si-BC) nanocomposites

Forty milligrams of silicon nanoparticles (SiNPs) (APS \approx 100 nm, Alfa Aesar, USA) were dispersed in 100 mL deionized water by ultrasonication for 3 min. Subsequently, 200 μ L phytic acid (Sigma-Aldrich, USA) was added and the mixture was vigorously agitated using a magnetic stirrer for 1 h at room temperature. These SiNPs were collected by centrifugation at 1000 rpm and re-dispersed in the DI-water. BC pellicles were cut into 4 cm x 4 cm square pieces, which were then immersed in the SiNPs dispersion solution for 1 day with stirring. The Si-BC composite was washed with deionized water and stored in water for further experiments.

4.2.2. Polyaniline (PANI) polymerization with BC (PANI-BC) and Si-BC nanocomposites (PANI-Si-BC)

Aniline (0.91mL, Sigma Aldrich, USA) was added to 50 mL of a 0.5 N HCl solution containing BC and Si-BC composites. Then, the solution was stirred for 1 h to disperse the aniline monomers in the BC membranes. Subsequently, 2.28 g of ammonium persulfate (Duksan pure chemical, APS, Korea), was added to the solution as an oxidant to initiate the polymerization. The polymerization of aniline was carried out at 20 °C for 1 h. After

polymerization, the composites were purified using methanol, distilled water and a 0.1 N HCl solution. The samples were dried in a vacuum oven or in a freeze dryer. Before characterization of the composites, All samples were stored in the desiccator that maintained 20 % relatively humidity at room temperature to minimize the effect of moisture on cellulose characterization of the composites.

4.2.3. Characterization of nanocomposites

The morphologies of the samples were observed using field emission scanning electron microscopy (FE-SEM, SUPRA 55VP, Carl Zeiss, Germany). The freeze-dried samples were cut into 1 cm x 1 cm sized pieces and were placed on conductive adhesive tape on aluminum stubs. To obtain the cross-sectional images of a BC hydrogel and SiNPs bound BCs, the samples were broken immediately after dipping in liquid nitrogen. The sample surfaces were coated with platinum using a sputter coater (SCD 005, BAL-TEC GmbH, Germany) before imaging. The imaging was performed in the “Inlens mode” at an acceleration voltage of 2 kV.

Electron transmission images of samples were captured by energy-filtering transmission electron microscopy (EF-TEM, LIBRA 120, Carl Zeiss, Germany). The Si-BC, PANi-BC, and PANi-Si-BC samples were immersed in separate vials with DI water and were ultrasonicated (VCX130, Sonic & Materials, USA) for 3 min at 40 W. Then, the solution with dispersed particles

was dropped onto copper grids. The images were obtained at an acceleration voltage of 200 kV.

The crystal structure of the SiNP bound BCs was determined using a high-resolution x-ray diffractometer (XRD, D8 DISCOVER, Bruker, Germany). For XRD experiments, 1 cm x 1cm samples were cut from vacuum dried specimens. X-ray diffractometry (XRD) was performed using Cu K α radiation.

Thermal degradation stability was measured by thermogravimetric analysis (TGA, TGA Q5000, TA Instruments, USA). About 10 mg of a vacuum dried sample was placed in an alumina crucible and was heated from room temperature to 600 °C at a heating rate of 10 °C min⁻¹ under flowing nitrogen.

The electrical conductivity of the composites after exposure to flexural stress was measured by bending the samples using a universal testing machine (UTM, GB/LRX Plus, Lloyd, UK). To perform this test, 4 cm x 1 cm vacuum dried specimens were loaded into the machine and were bent at a constant speed of 50mm min⁻¹ in constant temperature and humidity room which had 20% relative humidity at 24 °C. A 3 cm x 1 cm piece of aluminum foil was bonded to each end of the sample using silver paste (ELCOAT P-100, CANS, Korea) to allow connection of a digital multimeter (Chekman, Tae Kwang Electronics, Korea) for measuring the electrical conductivity. The bending

radius of the samples was calculated as suggested in the literature [159]. Specifically, the radius of the curvature (bending radius) was calculated as follows:

$$R = (d^2 + 4h^2)/8h$$

Here, d and h are the diameter and height of a dome, respectively. The change in electrical conductivity of the composites was measured after 100 repetitive bending cycles.

The percentage change in resistance was calculated as follows:

$$\Delta R (\%) = \{(R_0 - R_n)/R_n\} \times 100$$

where R_0 is the electrical resistance of the pristine composite, and R_n is the electrical resistance of the composite after bending n times.

4.3. Results and discussion

4.3.1. Preparation of the Si-BC composites

The adsorption of phytic acid on the SiNP surfaces resulted in a phosphoric acid-tagged SiNP surface. This allowed for immobilization of SiNPs onto the BC fibers through hydrogen bonding between the phosphoric acids of SiNPs and hydroxyl groups in the cellulose nanofibers (Figure 4-2). Figures 4-3A and B show optical images of the pure BC and a Si-BC

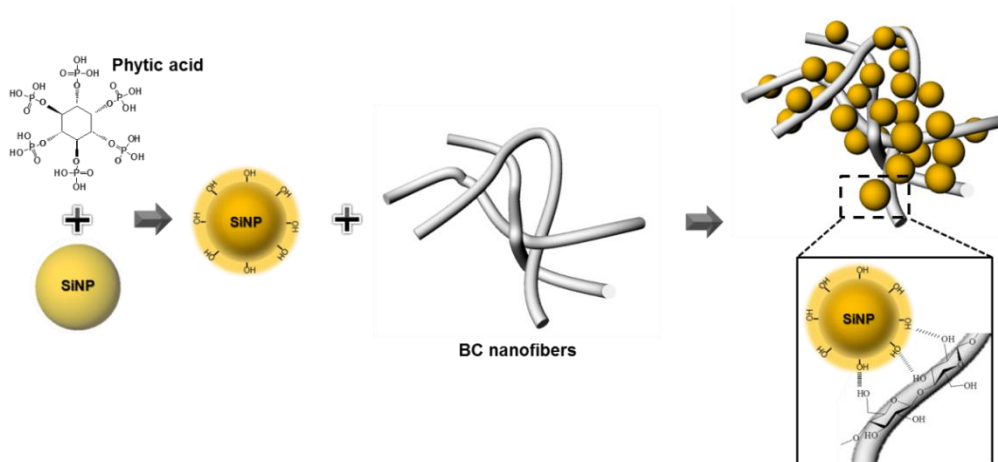


Figure 4-2. Hydroxyl groups were introduced on the surface of SiNPs as a result of modification with phytic acid. Hydroxyl groups of SiNPs can form hydrogen bonds with BC nanofibers.

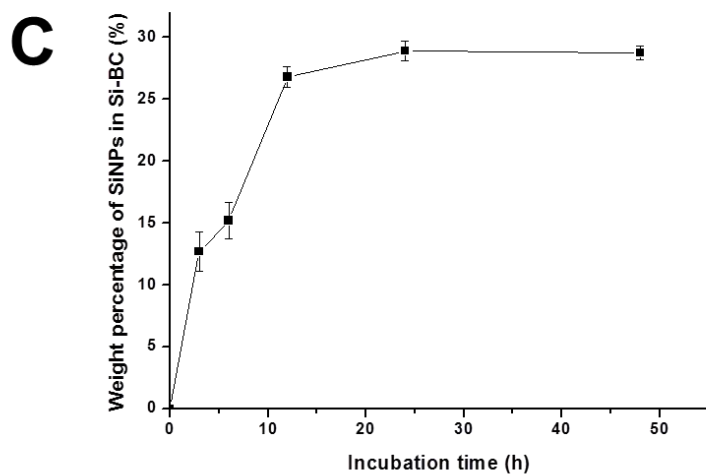
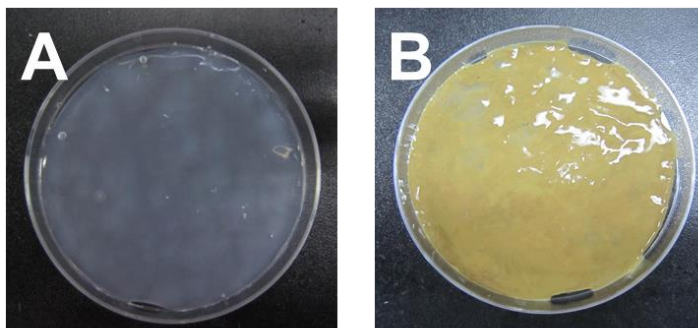


Figure 4-3. Optical images of (A) pure BC, (B) Si-BC composite and (C) the weight percentage of SiNPs bound to BC in Si-BC composite as a function of incubation time in SiNPs-dispersion solution.

composite. SiNPs were introduced into a BC hydrogel by immersing the biosynthesized BC hydrogel into a well dispersed SiNP solution containing phytic acid for 1 day. The initially translucent BC hydrogel became opaque and brown because of the adsorption of SiNPs into the BC nanofibers. The content of SiNPs in Si-BC was about 28.9 % of the total weight by comparing the weights of BCs before and after SiNPs adsorption (Figure 4-3C). Silicon dioxide formed on the surface of SiNPs can interact with the phosphoric acid groups of phytic acid via hydrogen bonding (Figure 4-2) [160]. Though the hydrogen bonding between silicon dioxide and phosphoric acid is weak, the six phosphoric acid groups on a single phytic acid provide stable interactions between the phytic acid and SiNPs [160]. Oxygen atoms in silicon dioxide can act only as acceptors during hydrogen bonding, but SiNPs modified with phytic acid have numerous hydroxyl groups that can serve as hydrogen bonding acceptors and donors [161]. Therefore, more SiNPs were adsorbed on the BC nanofibers after the modification of SiNPs with phytic acid than pure SiNPs during preparation of Si-BC. FT-IR spectrum of Si-BC was compared with that of BC bound with pure SiNPs without phytic acid to confirm the increase of hydrogen bonding between SiNPs and cellulose fibers. Unfortunately, it was not possible to obtain the evidence for the increased hydrogen bonding because the signal to noise ratio from the SiNPs surfaces was very low.

BC had a unique 3D-networked nanofiber structure, wherein the fiber

diameters were several tens of nanometers (Figure 4-4A). Cross-sectional images of BC showed a multilayered structure of cellulose with a spacing of about 5 μm as shown in Figure 4-4C. SiNPs were well distributed over the BC membranes and were attached to the surface along the BC nanofibers without severe aggregation (Figure 4-4B). We found SiNPs bound to the inner layer, the surface (through the relatively large pores), and the spacing between layers (Figure 4-4D). Severe aggregation of SiNPs was not observed in the inner layers, and the space between the cellulose layers remained even after the attachment of SiNPs.

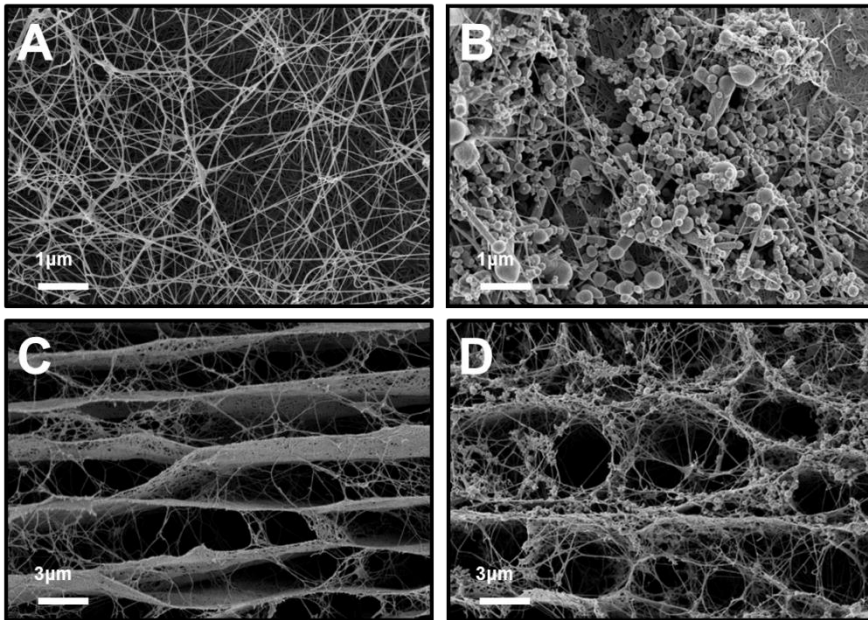


Figure 4-4. FE-SEM images of BC and Si-BC composite. (A) Surface and (C) cross section of freeze-dried BC. (B) Surface and (D) cross section of freeze-dried Si-BC composite.

4.3.2. Synthesis of PANi-Si-BC nanocomposites

To impart conductivity to the Si-BC composite, PANi was polymerized at the nanofiber surface, which served as a template for PANi polymerization. First, Si-BC was dipped into the aniline solution. The aniline monomers permeated into the porous BC membranes, and amine groups on the aniline monomers formed hydrogen bonds with the hydroxyl groups of BC [121] and the phosphoric acid groups of SiNPs coated with phytic acid[160]. After adding an oxidant solution of APS, PANi polymerized on both the BC nanofibers and SiNPs (Figure 4-5). The optimal conditions of polymerization (reaction time: 1h, molar ratio of APS to aniline: 1:1, reaction temperature: 20 °C) were obtained by varying the molar ratio of APS to aniline monomer, the reaction temperature and the reaction time at the constant HCl concentration (Figure 4-6). The amount of PANi increased as the molar ratio of APS to aniline increased, but the conductivity of the composites showed a maximum value at the molar ratio of APS to aniline of 1. The conductivity of PANi increased as PANi was polymerized on the BC nanofibers. The conductivity did not increase at the longer polymerization time than 1h. The weight percent of PANi did not increase at the polymerization time longer than 1h. The temperature of PANi polymerization was optimized at 20 °C because the conductivity of the composites showed a higher value at 20 °C, while the amount of PANi polymerized was similar at the temperature of 5, 20 and 40 °C.

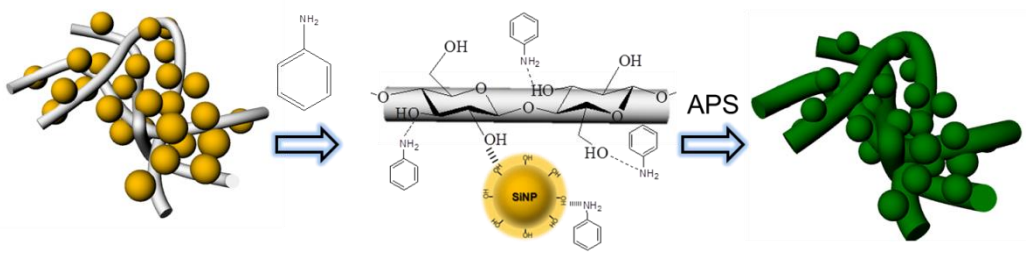


Figure 4-5. After adding aniline monomer and APS, PANi was polymerized on both BC nanofibers and SiNPs. The BC structure can serve as the template for both the adsorption of SiNPs and the polymerization of PANi.

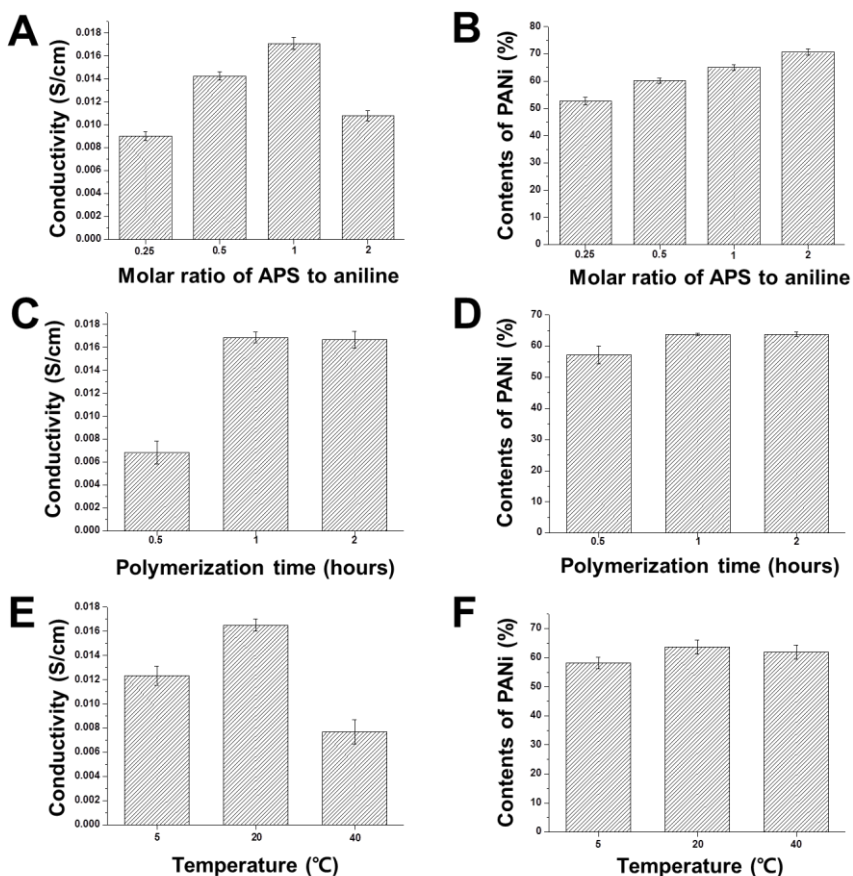


Figure 4-6. (A and B) Conductivity and contents of PANi/BC with molar ratios of APS to aniline from 0.25 to 2. (Polymerization time was 1h and reaction temperature was 20 °C), (C and D) Conductivity and contents of PANi-Si-BC with reaction time from 0.5h to 2h. (Molar ratio of oxidant (APS) to monomer (aniline) was 1 and reaction temperature was 20 °C), and (E and F) Conductivity and contents of PANi-Si-BC with different reaction temperature 5 °C and 30 °C. (Molar ratio of oxidant (APS) to monomer (aniline) was 1 and reaction time was 1h.

Compared with PANi on BC nanofibers alone (PANi-BC), PANi polymerized on Si-BC (PANi-Si-BC) had thicker granular structures along the fibers (Figure 4-7). The typical spherical structure of SiNPs was not observed in PANi-Si-BC, but the surface of SiNPs was coated with PANi, which formed a porous, granular structure (Figure 4-7B). The porous structure of PANi at the SiNPs enhanced the Li-ion diffusion and electrolyte penetration into the electrode, and provided free space for volume expansion of the SiNPs during electrochemical cycling when the material is used in Li-ion batteries. As shown in the cross-sectional image of PANi-Si-BC, aniline monomers diffused inside of the BC pellicles and polymerized to form highly porous PANi, which filled the spaces in the BC pellicles (Figure 4-7C).

SiNPs coated with PANi were observed in the TEM images shown in Figure 4-8. SiNPs were immobilized on the surface of the networked BC nanofibers, which showed reasonable stability after harsh ultrasonication (Figure 4-8A). When aniline monomers were polymerized with unmodified SiNPs, PANi was not observed on the surface of the SiNPs. Instead, PANi with a branch-like morphology was formed in the bulk, as shown in Figure 4-8B. SiNPs were encapsulated well by PANi when aniline monomers polymerized in the presence of phytic acid, (Figure 4-8C). The increased affinity of SiNPs to PANi could be attributed to the hydrogen bonding between phosphoric acid groups of phytic acid at the SiNPs surface and amine groups of aniline monomers (Figure 4-5). The gaps between the SiNPs in the

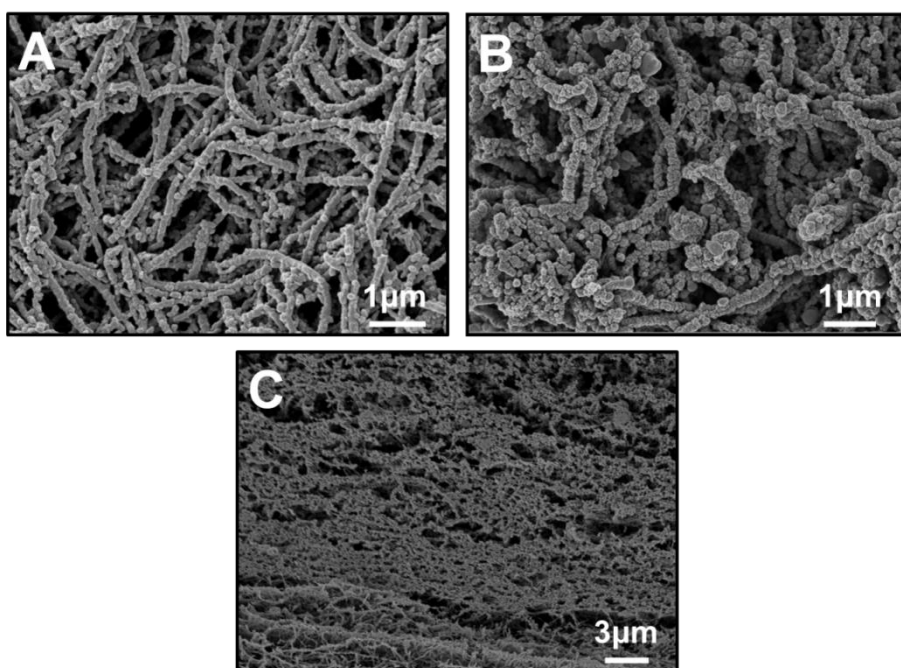


Figure 4-7. SEM images of composites. (A) Surface image of PANi-BC, (B) surface image of PANi-Si-BC, and (C) cross sectional images of freeze-dried PANi-Si-BC.

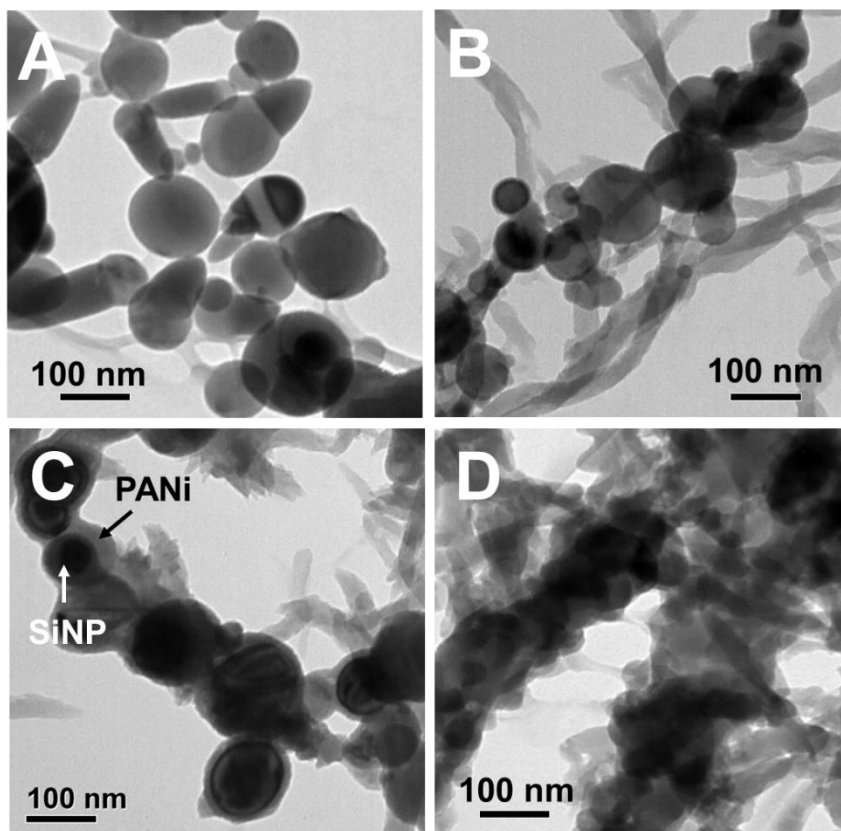


Figure 4-8. TEM images of composites. (A) Si-BC and (B) PANi-Si without phytic acid. (C) PANi-Si and (D) PANi-Si-BC with phytic acid.

Si-BC samples were filled with PANi, which would provide the composite with better conductivity due to its compact structure (Figure 4-8D).

The presence of SiNPs in the PANi-Si-BC composites was confirmed by XRD analysis (Figure 4-9A). The XRD spectrum of the BC had two characteristic peaks at $2\theta = 14.6^\circ$, 22.6° , indexed to (1 $\bar{1}$ 0) and (200) reflections of cellulose I, respectively [162]. PANi-BC showed broad peaks at $2\theta = 14.7^\circ$, 20.3° , 25.2° , but the degree of crystallinity of the PANi was very low. The two broad peaks at 20.3° and 25.2° were caused by the periodicity parallel and perpendicular to the polymer chain, respectively [122, 163]. The intensity of the BC peaks decreased as the amorphous PANi was synthesized on the BC nanofibers. PANi-Si-BC showed three additional peaks indexed to the (111), (200) and (311) planes of Si while PANi-BC without SiNPs did not show the assigned peaks for Si [164, 165]. These observations confirmed that the SiNPs were well encapsulated in PANi on the BC composites. However, the presence of SiNPs in the composites reduced the ratio of the peak intensity at $2\theta = 14.6^\circ$ to the peak intensity at $2\theta = 22.6^\circ$ while the ratio of the peak intensities didn't change for pure BC and phytic acid treated BC (Figure 4-9B). It resulted from the restricted intermolecular interactions between the cellulose nanofibers whose space was occupied with ~100 nm size of SiNPs.

Figure 4-10 shows TGA curves of the BC, Si-BC, and PANi-Si-BC. All samples showed a weight reduction of about 4 % below 150 °C, which was attributed to water evaporation. The degradation of BC occurred at about

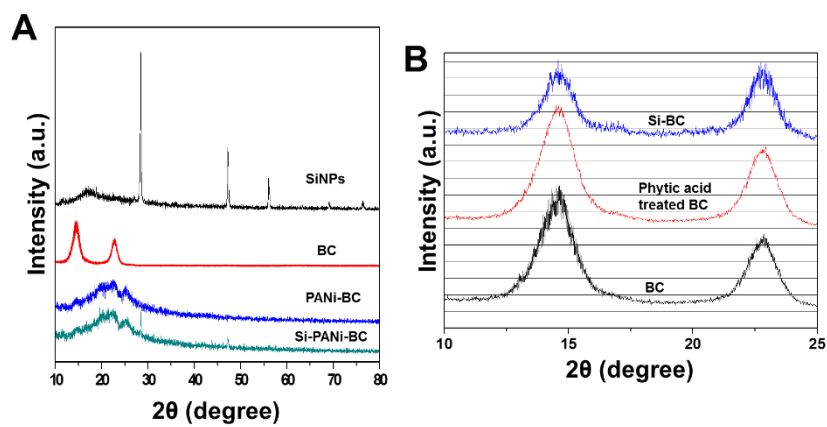


Figure 4-9. XRD patterns of composites. (A) SiNPs, BC, PANi-BC, and PANi-Si-BC. (B) Change of crystallinity after the incorporation of SiNPs in BC.

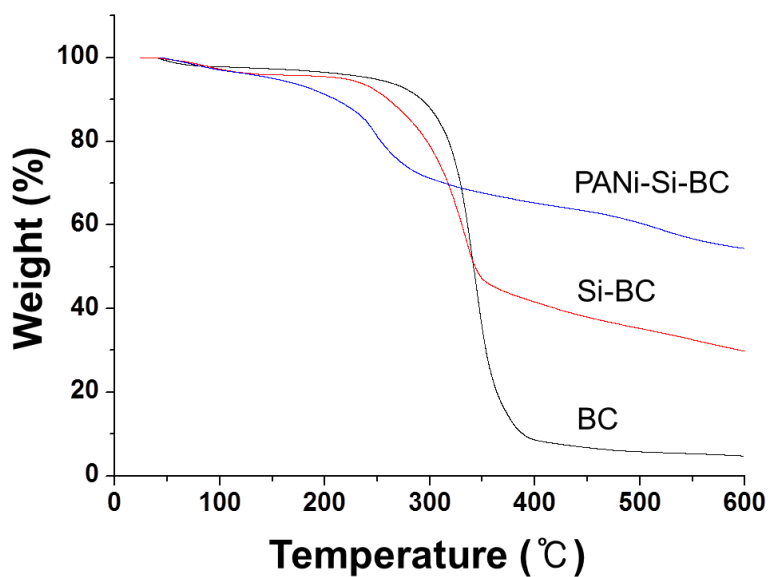


Figure 4-10. Thermal stability of the composites. Thermogravimetric curves of BC, Si-BC and PANi-Si-BC were obtained using 10 mg of a vacuum dried sample in the range of temperature from 25 °C to 600 °C at a heating rate of 10 °C min⁻¹ under flowing nitrogen.

342 °C due to the cleavage of cellulose chains [166]. The residue of BC was 4.7 % of the total weight at 600 °C. When normal BCs are dried, inter- and intramolecular hydrogen bonding occurs between the cellulose chains [167]. In the case of Si-BC, the presence of SiNPs restricted the packing of cellulose chains during dehydration. For this reason, the first thermal degradation of Si-BC occurred at 331 °C, which was about 11 °C lower than the BC. However, the weight loss of Si-BC was smaller than BC due to the high thermal stability of SiNPs.

The weight residue of the Si-BC (initial weight percent SiNPs 28.9 %, BC 71.1 %) was 30.7 % of the total weight at 600 °C (Figure 4-10). Considering 4.7 % of BC residue at 600 °C in the TGA curve, the weight residue of BC in Si-BC composite would be 3.3 %. Therefore, the actual weight residue of SiNPs in the Si-BC composite was determined to be 27.4%. It was in agreement with 28.9 % of the initial weight percent of SiNPs in the Si-BC composites.

The first degradation of PANi-Si-BC (initial weight percent PANi 63.5 %, SiNPs 10.5 %, BC 25.7 %) occurred at 248 °C, which was much lower than normal BC or Si-BC. The degradation at lower temperature was associated to the weakened intermolecular hydrogen bonding of BC in the PANi-BC composite [121], low molecular weight of polyaniline and dopant evaporates [168, 169]. The weight loss at 517 °C was attributed to the thermal degradation of polyaniline chains, and the weight residue of PANi-Si-BC was

54.4 % at 600 °C [122, 163].

The effect of phytic acid on the degradation of cellulose was investigated by the morphological change of the cellulose which was immersed in 0.2 % phytic acid solution for 1 day (Figure 4-11A). Since the phytic acid was used for the modification of SiNP surfaces rather than for the modification of cellulose fibers, the possibility of the direct degradation or catalytic degradation of cellulose chains would be negligible. XRD data didn't show any significant difference between the BC and phytic acid treated BC confirming the chemical stability of BC. We also confirmed the thermal stability of BC immersed in phytic acid solution through the thermal decomposition behavior by TGA (Figure 4-11B). The phytic acid treated BC showed a similar thermal decomposition behavior to normal BC and no significant difference could be found in the TGA curves.

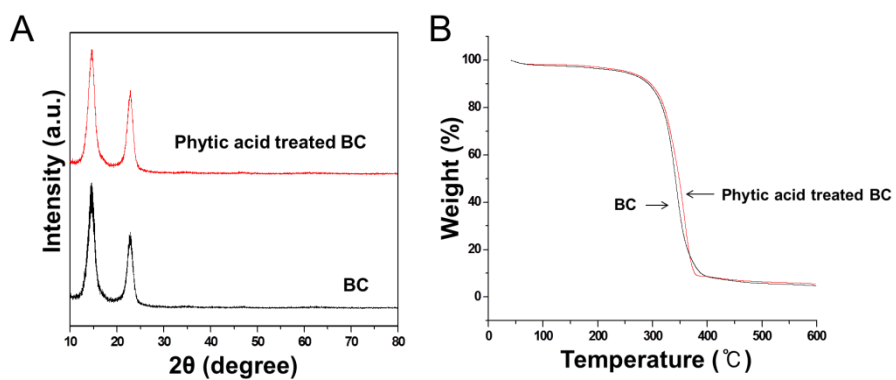


Figure 4-11. Effect of phytic acid on the composites. (A) Morphological change and (B) the thermal stability of composites.

4.3.3. Conductivity of nanocomposite under bending stress

Stable electrode conductivity is a critical factor because the brittleness of PANi is the main barrier to its use in flexible batteries. Therefore, we investigated the conductivity of BC composites under bending stress. Prior to the conductivity measurement, we found out that the electrical properties of the composites could be changed by the moisture adsorption due to the sensitivity of cellulose to the moisture. First, samples were stored in desiccator until the use and the measurement of electrical conductivity was performed at 20% relative humidity and room temperature. PANi-Si-BC composites were bent while the conductivity was continuously measured. The radius of curvature was calculated based on a diagram of a dome formed during application of the bending stress (Figures 4-12A). As shown in Figure 4-12B, PANi-Si-BC composites did not show significant changes in resistance over the whole range of bending curvature. Based on these data, we concluded that BC provided mechanical stability to the composites by providing a characteristic 3D networked structure. Stable conductivity under repetitive bending stress is important for reliable electrical applications. PANi-Si-BC retained its initial conductivity for 100 bending stress cycles, which confirmed its reliability as a flexible electrical component (Figure 4-12C).

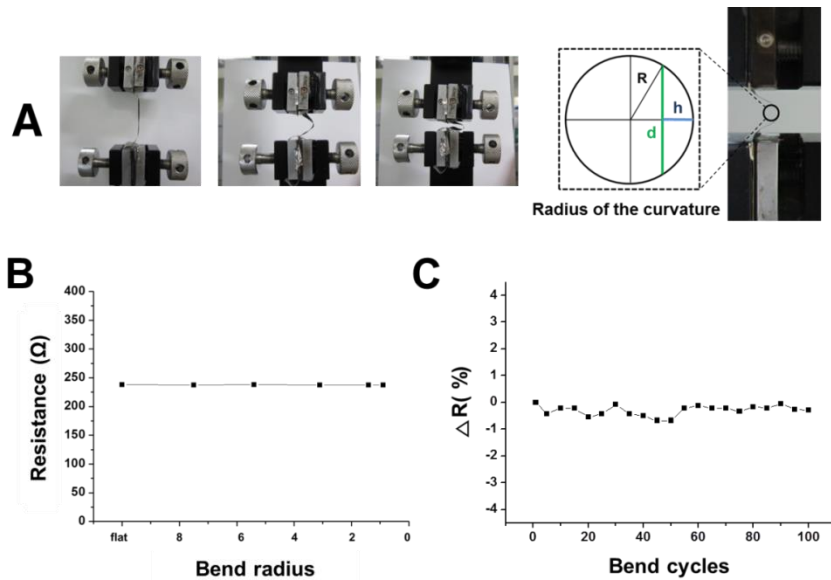


Figure 4-12. Electrical stability of the composites to bending stress. (A) Optical images of bending process using UTM and parameters for the calculation of the bending radius, (B) resistance variation of PANi-Si-BC composite for changes in bending radius, and (C) the percentage of resistance change of the composite according to bending cycles up to 100 cycles.

4.4. Summary

BC was used both as a binding template for SiNPs and as a template for in situ polymerization of 3D networked PANi. SiNPs were uniformly attached to the surface of BC pellicles along the nanofibers. Phytic acid enhanced the binding efficiency of SiNPs to both BC nanofibers and aniline by providing increased hydro-gen bonding. The conductive PANi-Si-BC composite showed stable conductivity under repetitive bending stresses, which confirmed its potential for use as a flexible anode component in flexible recharge-able batteries.

Chapter 5

Surface-enhanced Raman scattering sensor based on a BC hydrogel

5.1. Introduction

Surface-enhanced Raman scattering (SERS) has drawn great attention as a sensitive and label-free analytical tool due to its high sensitivity, specificity, and rapid response in the detection of chemical and biological analytes [170-172]. Critical to the organization of the SERS-sensor is increasing the density of SERS hot spots, which have relevance to the strong electromagnetic field associated with the surface plasmon resonance of metal metal nanostructures [173]. Hot spots are normally formed at the interstices adjoining metal nanoparticles, and enhance the Raman signal of the adsorbed analytes [171]. Many studies have been conducted on the design of 2D SERS substrates; controlling the size and shape of the nanoparticles, as well as the interparticle distances for the optimization of hot spots [174-176]. 3D SERS substrates are currently receiving attention because of their potential to maximize hot spot numbers when compared with 2D substrates [171, 173]. A variety of substrates, such as AgNPs-decorated Au-nanotip arrays for label-free DNA detection, AgNPs-decorated ZnO-nanorod arrays for polychlorinated biphenyls detection, porous structures of nanowire networks, vertically-aligned CNTs, and AuNPs-deposited filter papers, have been investigated [177-181]. In comparison with 2D nanostructures, 3D nanostructures have the associated advantages of larger surface area, allowing a larger number of SERS hot spots as well as sites for adsorbing analytes [182]. 3D substrates can also supply spaces for capturing analytes, which 2D substrates cannot

capture effectively.

The application of cellulose as a template for the synthesis of metal nanoparticles has been attempted [183-186]. BC is considered a better candidate for metallic support than other plant cellulose [187-190]. Since the nanoparticles were synthesized and immobilized on the substrate, the aggregation of nanoparticles in the process of detection was avoided. Another advantage of this process is that the contraction of BC layers was also determined to be part of the process used to confirm the advantages of BC-metal hybrids. A logical expectation was that variations in deformation would generate SERS hot spots and enhance the SERS intensity.

In this part, increasing of SERS intensity as driven by the spatial deformation of AuNPs-BC hydrogels was described. The interlayer distances of AuNPs-BC could influence the SERS signal due to the decrease of inter-particle distance of AuNPs within BC. For preparing AuNPs-BC hydrogel, *in situ* synthesis method was used. In this process, BC nanofibers were used not only as a template, but also as an immobilized reducing agent to synthesize the high density of AuNPs with 20nm size. Many hydroxyl groups of BC fibers could provide reducing power for metal synthesis without a reducing reagent (Figure 5-1).

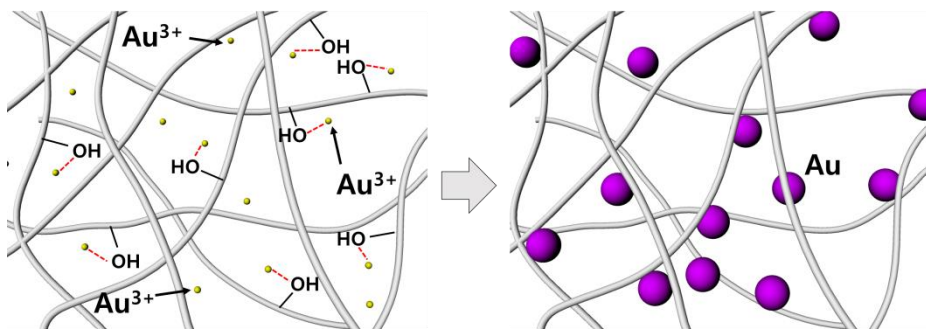


Figure 5-1. Schematic representation of the process for preparing AuNPs-BC hydrogel.

5.2. Materials and method

5.2.1. *In situ* synthesis of gold nanoparticles (AuNPs)-BC

AuNPs-BC hydrogels were synthesized via the reduction of H₂AuCl₄ on the BC fibers. A mixed solution of 46.7 μ L of H₂AuCl₄ (21.4 %) and 99 mL of DI water was heated to boiling. After a yellowish suspension was formed, the purified BC hydrogel (5 mm \times 5 mm \times 3 mm) was added to the solution with vigorous stirring. AuNPs were grown on the BC for 10, 30 and 60 min, and washed with DI water to stop the reaction. The AuNPs-BC hydrogel was stored in DI water until use.

5.2.2. Characterization of AuNPs-BC nanocomposites

The UV-Visible absorption spectra of the samples were obtained using a UV-Visible spectrophotometer (Optizen 2120UV, Mecasys), and the crystal structure of the samples was determined using a high-resolution x-ray diffractometer (XRD, D8 DISCOVER, Bruker). Transmission electron microscopy (TEM, Leo-EM912 Omega, Carl Zeiss) was conducted at an acceleration voltage of 200 kV. The surface and cross-sectional morphology of the samples was obtained at an acceleration voltage of 2 kV using field emission-scanning electron microscopy (FE-SEM, JSM-6330F, JEOL). Raman measurements were taken using a micro-Raman system (JY-Horiba, LabRam 300) equipped with a thermoelectrically-cooled (-70 °C) CCD

detector. The signal was collected by a $\times 50$ objective lens (Olympus, 0.55 NA) with back-scattering geometry. The 647 nm laser line from a Kr ion laser (Coherent, Innova 300C) was used as the excitation source. An acquisition time of 1 s was used with a laser power at the sample of 0.55 mW.

5.2.3. SERS experiments

Solutions of 4-FBT and PAA at different concentrations (10^{-7} and 10^{-3} M) were prepared in water. The AuNPs-BC hydrogel was immersed into 1 mL of solution for 30 min. After soaking in analyte solution, the samples were rinsed several times with DI water and freeze-dried or heat-dried at 80 °C for 3 h. AuNPs-attached cover glass was prepared as a control surface for the SERS substrate. For Raman measurement, an excitation laser source of 647 nm was employed due to the plasmon absorption of AuNPs within the BC hydrogel. The acquisition time was 1 s, and the power at the sample was 0.55 mW for each measurement.

5.3. Results and discussion

5.3.1. *In situ* synthesis of AuNPs-BC hydrogel

BC nanofibers were used not only as template but as immobilized reducing agent to *in situ* synthesize the AuNPs-BC hydrogel. This method is a simple and environment-friendly hydrothermal synthesis technique because lots of hydroxyl groups of BC fibers could provide reducing power for metal

synthesis without reducing reagent [172, 190]. After the BC hydrogel was added into the boiling HAuCl_4 solution, the reaction occurred immediately and the color of the BC hydrogel gradually changed from white to purple, which is characteristic of surface plasmon resonance of AuNPs, and indicated the formation of the AuNPs in the BC hydrogel (Figures 5.2A and B). Pure BC hydrogel showed no absorption bands in the range from 400 to 800 nm. However, AuNPs-BC hydrogel showed a typical plasmon extinction of AuNPs at 550 nm (Figure 5.2C). Since the color of the solution did not change at all during the reduction process, the color change of BC hydrogel revealed that AuNPs had grown on the surface nanofibers within BC hydrogel. This result indicated that cellulose was able to reduce Au^+ ions to Au under hydrothermal environment. The XRD spectrum of pure BC nanofibers (Figure 5.2D) had three peaks at 14° , 16° , 22° , indexed to $(1\bar{1}0)$, (110) , and (200) reflections of cellulose I, respectively [188, 191]. Besides these peaks of BC, the XRD spectrum of the AuNPs-BC hydrogel had additional four peaks indexed to the (111) , (200) , (220) , and (311) planes of face-centered cubic (fcc) Au [188]. The XRD analysis confirmed that AuNPs were well synthesized on the BC nanofibers in the composites.

The AuNPs were immobilized stably on the nanofiber surface even after the harsh ultrasonication. The AuNPs synthesized at different reaction time on the BC fibers of hydrogel were characterized by TEM. The size of AuNPs was less than 15 nm in diameter at the reaction time of 5 min but it increased as

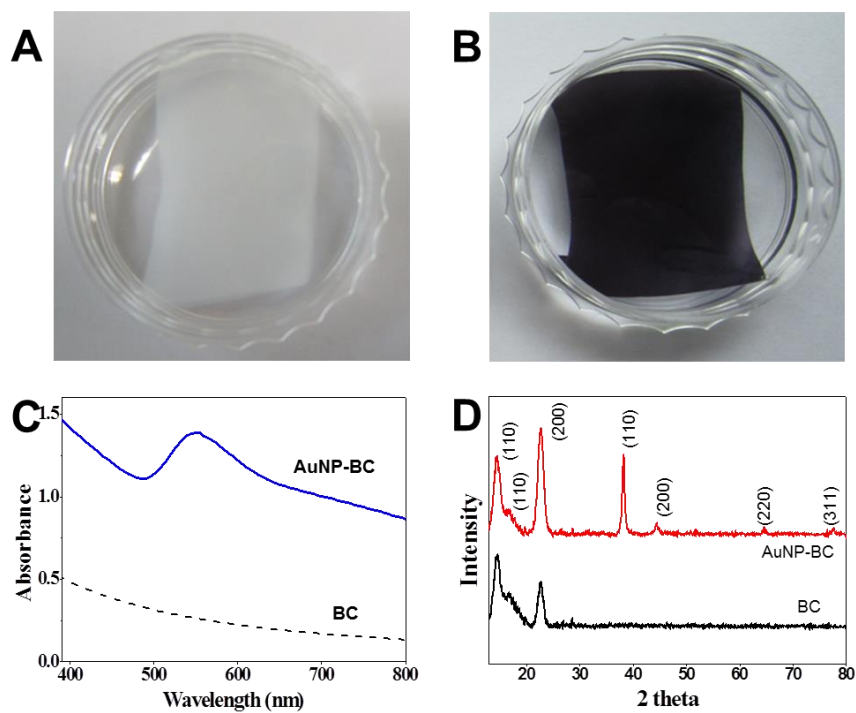


Figure 5.2. Preparation of highly dispersed AuNPs-BC. Optical image of normal BC (A) and AuNPs-BC (B). (C) Absorption spectra of AuNPs-BC and normal BC and (D) characteristic XRD peaks of AuNPs-BC and normal BC.

the reaction time increased. (Figure 5.3) Although the particle density in the hydrogel also increased as the reaction time increased, the size distribution of AuNPs became broader at the reaction time of 30 min (Figure 5.3C). For the uniformity of AuNPs ($20.67 \text{ nm} \pm 3.62 \text{ nm}$), the AuNPs-BC prepared at the reaction time of 10 min was used for the further experiments. Figure 23 D shows the energy-dispersive spectrum (EDS) from SEM of same sample of figure 2B. This spectrum had only C, O and Au elements in the composites. It means that the AuNPs-BC composites have been fabricated successfully by *in situ* synthesis of AuNPs.

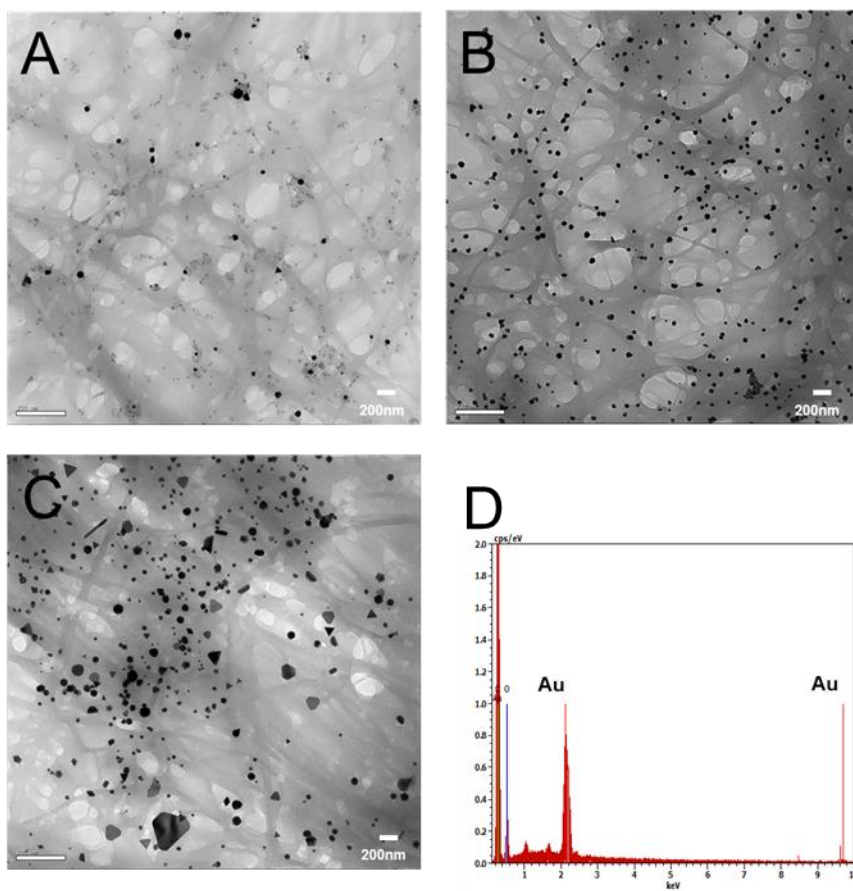


Figure 5.3. TEM images of AuNPs-BC synthesized with different reaction time. (A) 5, (B) 30 and (C) 60 min. Inserted micrographs are SEM images of each samples. (D) EDS spectrum from SEM image of sample (B)

5.3.2. SERS measurement using undeformed AuNPs-BC

The BC hydrogel had a unique 3D network structure consisting of nanofibers whose diameter was several tens of nanometers. Cross-sectional image of freeze-dried AuNPs-BC hydrogel showed a unique multilayered structure of ultrathin layers spacing regularly by 6.25 μm apart (Figures 5-4A and B). Figure 5-4C is graph of thickness of BC hydrogel as a function of cultivation time. 2 days cultured BC was not well formed and very thin almost 62 μm . The thickness of 3 days cultured BC was 180 μm , 4 days cultured BC was 277 μm , and 6 days cultured BC was 304 μm . In figure 33, 32 layers are existed in 208 μm size. Therefore the number of layers and the thickness of each sample could be calculated. The number of BC layers increased proportionally as the cultivation time increased. Four BC hydrogels with different number of layers (about 10, 30, 40 and 50 layers) were prepared for AuNPs formation. Because of a highly porous structure, gold ions could be easily infiltrated into the interlayer of BC hydrogel and formed a homogeneous 3D AuNPs-BC hydrogel with SERS activity. The SERS intensity could be influenced by the number of BC layers. Raman signals of 4-FBT were measured with undeformed AuNPs-BC substrates that had different number of BC layers. Typical SERS spectrum was obtained as shown in Figure 5-5A. Increasing the BC cultivation time caused the larger number of layer, which increased the capacity of AuNP-BC for 3D SERS substrates (Figure 5-5B).

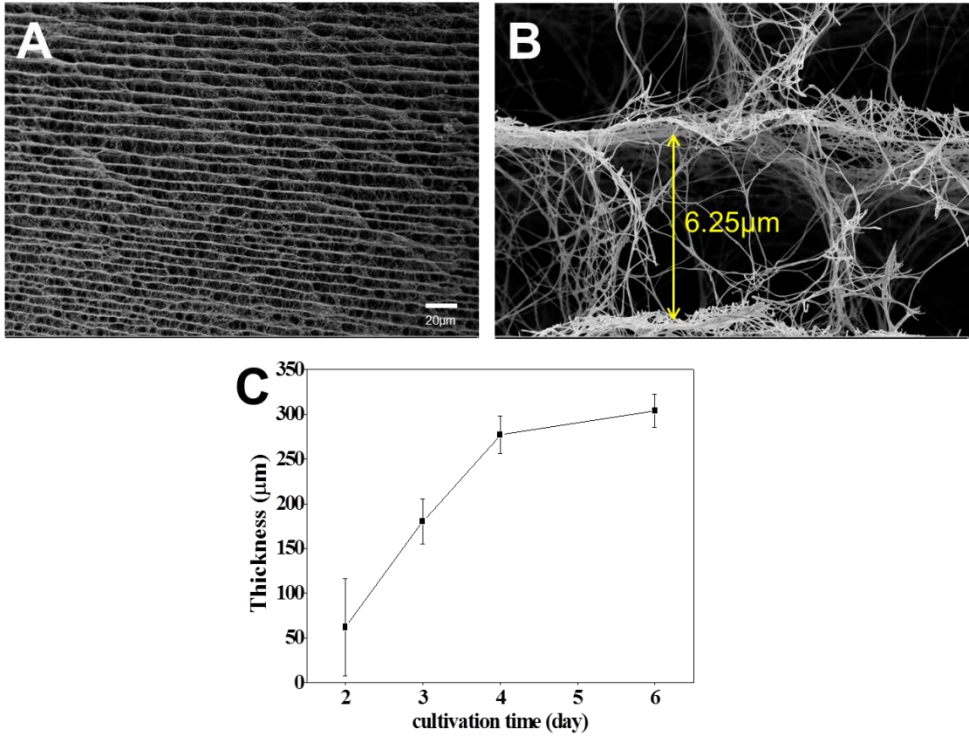


Figure 5.4. The multilayer structure of the BC hydrogel. (A) The cross-sectional SEM image of the freeze-dried BC hydrogel, (B) spacing between BC layers, and (C) the thickness of the BC hydrogel as a function of cultivation time.

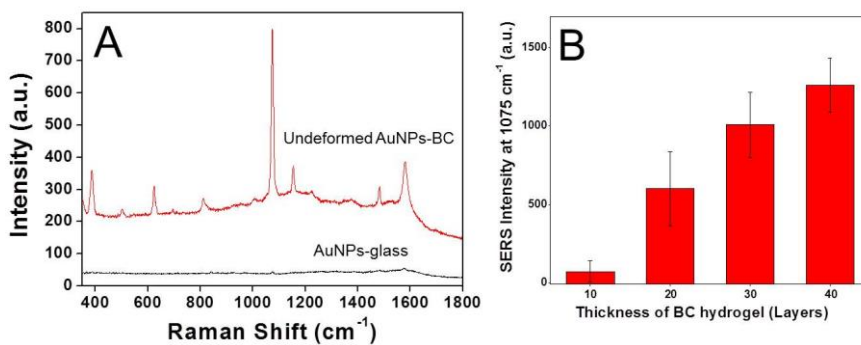


Figure 5-5. SERS measurement with undeformed AuNPs-BC hydrogel. (A) Typical Raman spectrum 4-FBT on AuNPs-glass and undeformed AuNPs-BC. (B) Effect of layer number on SERS intensity. SERS signal at 1075 cm⁻¹ was compared.

Also, SERS intensity depending on concentration of 4-FBT shows linearity in the range from 1.0×10^{-6} M to 1.0×10^{-3} M (Figure 5-6) thus this substrates is expected to make quantitative measurements possible. For comparison, detection of 4-FBT using two dimensional SERS substrate also attempted. 2D substrate was fabricated on the 3-aminopropyltriethoxysilane-coupled glass with ~ 20 nm AuNPs in a simple way. The 2D substrates were treated with analyte solution in the same way as AuNPs-BC and the SERS measurement condition was also same, but the result was quite different. Any trend in intensity of SERS spectra for different concentration of 4-FBT could not be observed well (figure 5-6A). Control of hot spot in this type of 2D substrate seemed to be difficult and also the signals were weak relatively. Au NPs should be heavily attached for large signal enhancement, which causes heterogeneous sensor surfaces and randomly located hot spots. On the other hand, the tendency of signal intensity displayed in AuNPs-BC (figure 5-6B) is thought to arise from controlled fabrication of many hot spot sites utilizing 3D networked BC substrates containing AuNPs.

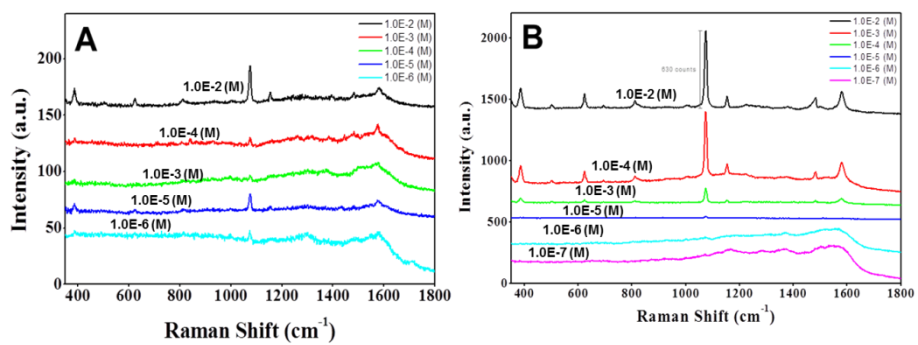


Figure 5-6. SERS spectra of different concentrations of 4-FBT obtained with (A) two dimensional AuNPs-attached glass substrate, and (B) undeformed AuNPs-BC.

5.3.3. SERS measurement using deformed AuNPs-BC

Enhancement of SERS signal depends on the density of SERS hot spots that are located at nanogap between particles and sharp edge of nanostructures. From the feasibility test, we found out that SERS hot spot density within the AuNPs-BC could be increased by contracting the 3D structure of AuNPs-BC hydrogels. In natural, AuNPs-BC shrinks in the drying process and the interlayer distance tends to decrease. The morphological difference between hydrated and dehydrated AuNPs-BC hydrogels was clearly observed in the SEM images (Figure 5-7). BC nanofibers of hydrated BC were loosely tangled and each layer was spatially separated by 6.5 nm (Figure 5-7A and B). In the middle of dehydration of BC hydrogels, AuNPs in the BC layers could be closely packed as shown in Figure 5-7C and D. Furthermore, the close packing of AuNPs could increase the possibility for the analytes confined between the BC layers to be detected by SERS. The effect of contracting AuNPs-BC on SERS enhancement was significant as shown in Figure 5-8 and 5-9. The SERS intensity of AuNPs-BC increased up to 10 times by spatial deformation (5-8).

Figure 5-9D shows that the SERS intensities comparison for three substrates and the signal intensity can be significantly amplified by change of dimensional characteristics due to increase of analyte molecules in the focal volume.

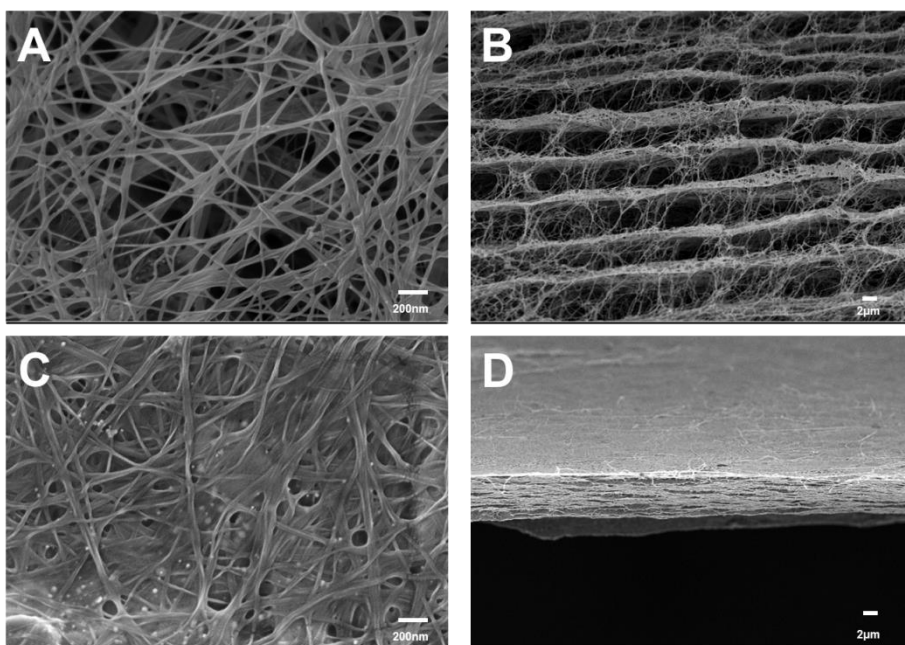


Figure 5-7. FE-SEM images of AuNPs-BC composites. Top view (A) and cross-section (B) of hydrogel-state of Au30-BC. Top view (C) and cross-section (D) of spatially deformed Au30-BC.

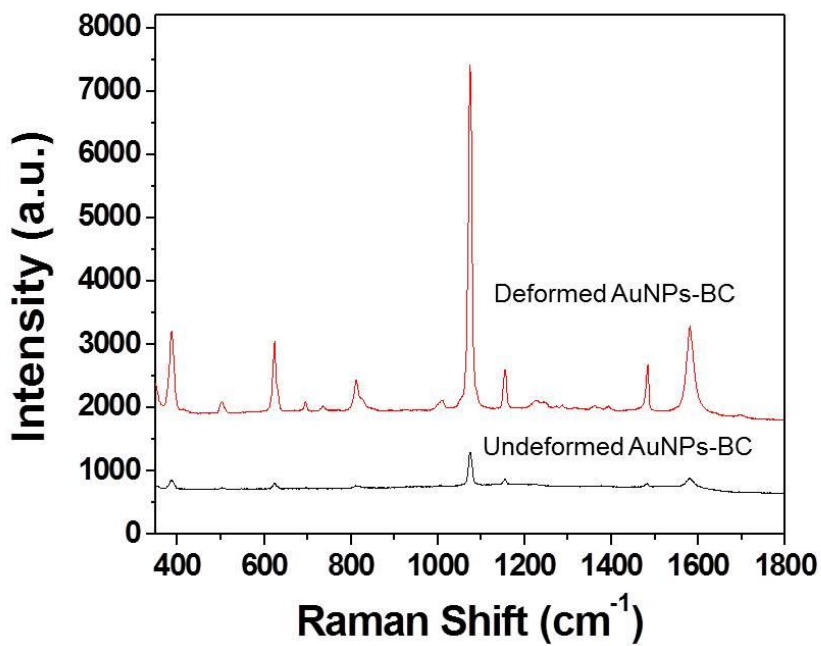


Figure 5-8. Effect of spatial deformation of AuNPs-BC hydrogel on SERS signal. SERS spectra of 4-FBT obtained with undeformed AuNP-BC, and spatially deformed AuNP-BC. 4-FBT concentration: 10^{-3} M.

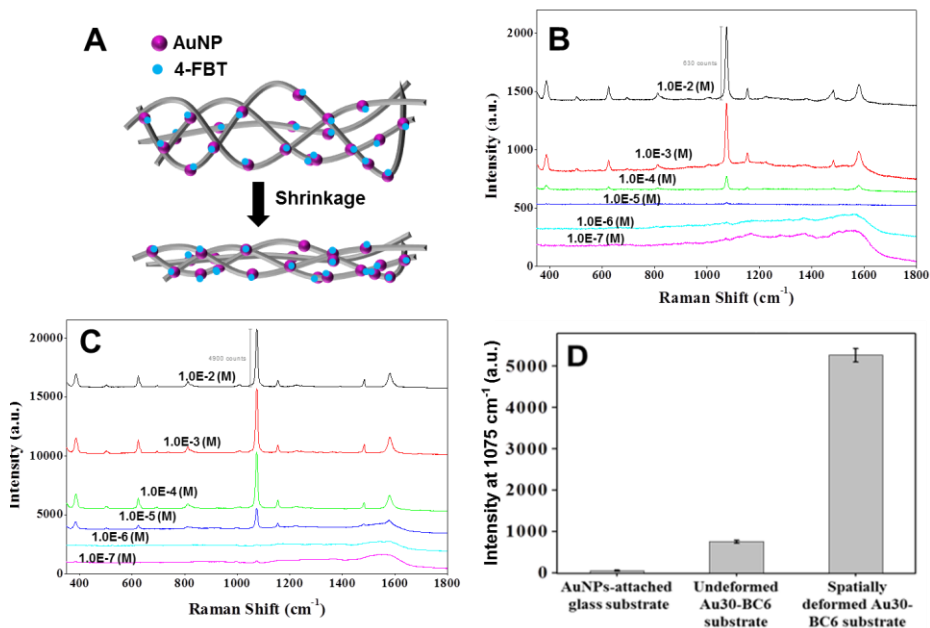


Figure 5-9. Detection of 4-FBT with AuNPs-BC composites (A) Schematic description for additional enhancement of SERS in case of the molecules which have strong affinity to noble metal surface such as 4-FBT (B) SERS spectra of 4-FBT obtained with undeformed AuNP-BC substrates, (C) SERS spectra of 4-FBT obtained with spatially deformed AuNP-BC substrates, and (D) SERS intensities comparison for three substrates.

5.3.4. Detection of molecules with weak affinity to Au surfaces

In general, SERS effect is less significant for chemicals which have little affinity to metal surface. PAA is one of the chemicals showing weak affinity to the gold surface. This analyte was chosen for the feasibility study of contraction-mediated SERS enhancement (5-10). As shown in Figure 5-10D, no specific band was observed from PAA (1×10^{-7} M) with undeformed AuNPs-BC. On the contrary, several characteristic SERS signals were detected clearly with a spatially deformed AuNPs-BC hydrogel as shown in Figure 5-10D. Specifically, a band at 997 cm^{-1} could be assigned to in-plane bending mode and a broad band at $1500 \sim 1600 \text{ cm}^{-1}$ was determined to be a characteristic feature of photo-decomposed carbons of benzene ring [192-194]. The significant enhancement of SERS signal resulted from locating the molecules in a close proximity to AuNPs by contracting AuNPs-BC hydrogel (Figure 5-10).

The 3D networked structure of BC hydrogel interposes water due to its highly nanoporous structure and characteristic of fibers which displays a good sorption of water. Because most biomolecules are active in wet condition, AuNPs-BC hydrogel can be a good substrate for functional SERS detection. SERS signal enhancement in wet condition is in progress.

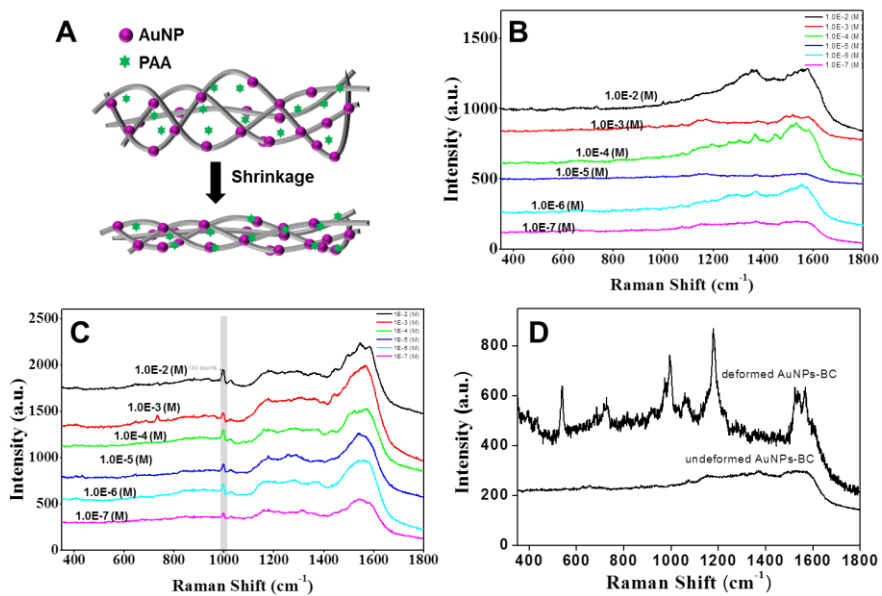


Figure 5-10. Detection of PAA with AuNPs-BC composites (A) Schematic description for additional enhancement of SERS in case of molecules which have weak affinity to noble metal surface such as PAA (B) SERS spectra of PAA obtained with unmodified AuNP-BC substrates and (C) SERS spectra of PAA obtained with spatially deformed AuNP-BC substrates (D) SERS spectrum of PAA with concentration of 1×10^{-7} M.

5.4. Summary

AuNP-BC hydrogels were fabricated via the reduction of AuNPs on BC fibers. The SERS signal could be significantly enhanced by spatially deforming the hydrogels in the process of drying. The BC hydrogel had a unique microstructure of multilayers with regular spacing. The spacing between layers could be reduced in the process of drying, and AuNPs on the BC nanofibers could form a number of hotspots as a result. SERS signal enhancement was confirmed with 4-FBT and PAA. PAA in particular, which did not have affinity for the AuNP surface, could be successfully detected by contracting the AuNP-BC hydrogels.

Chapter 6

Oxidized BC/alginate hydrogel for cell encapsulation

6.1. Introduction

Cell encapsulation has been interested in a technology to provide immunoprotection for transplanted cells. The cells are able to be protected from the immune systems by semipermeable membrane that let nutrients and secreted proteins permeate while isolating the cells from hostile immune reaction. Therefore transplantation of encapsulated cells has been suggested to be a promising cell-based treatment for a variety of diseases such as diabetes, metabolic deficiencies, liver failure, cancer, and neurodegenerative and cardiovascular diseases [195-198]. Alginate is a biopolymer that forms a hydrogel in the presence of divalent cations, such as Ca^{2+} [199]. Because alginate hydrogels have excellent biocompatibility, they have been preferentially used to protect transplanted cells from immune rejection and as a matrix to increase the cell viability in cell encapsulation. However alginate has not sufficient mechanical and chemical resistance properties to achieve long-term transplantation. Consequently many researches are conducted to overcome the limitation by adding other polymers such as chitosan, cellulose, pectin, starch in alginate matrix.

Superior properties of BC make it as a promising material for not only reinforcing matrix but also functional materials. However, BC is difficult to convert into materials for components of composites due to its high crystallinity and interconnected 3D structure owing to large number of hydrogen bonds. Thus, so far various systems have been investigated to make

individualized cellulose fibrils dispersed in water. Such modifications could make it possible to loosen the adhesion between cellulose fibrils by breaking the interfibril hydrogen bonds. Among the many methods, TEMPO-oxidation process is a good way to modify some surface of cellulose for obtaining well dispersed fibrils without significant aggregation cellulose due to the electrostatic repulsion of nanofibers. TEMPO-oxidation method is easily reacted under mild condition, environment friendly compared to other methods.

Therefore, in this part, a novel approach to design alginate-cellulose membrane for cell encapsulation was attempted. 6,6-tetramethylpiperidine-1-oxylradical TOBC was used to obtain improved properties of hydrogel for cell encapsulation. Both TOBC and alginate have similar chemical structure and they can participate in divalent calcium ions (Ca^{2+}) crosslinking process. Carboxyl groups on the surface of TOBC can participate in the forming of an alginate based composite and play important roles in the structural, mechanical and chemical stability (Figure 6-1).

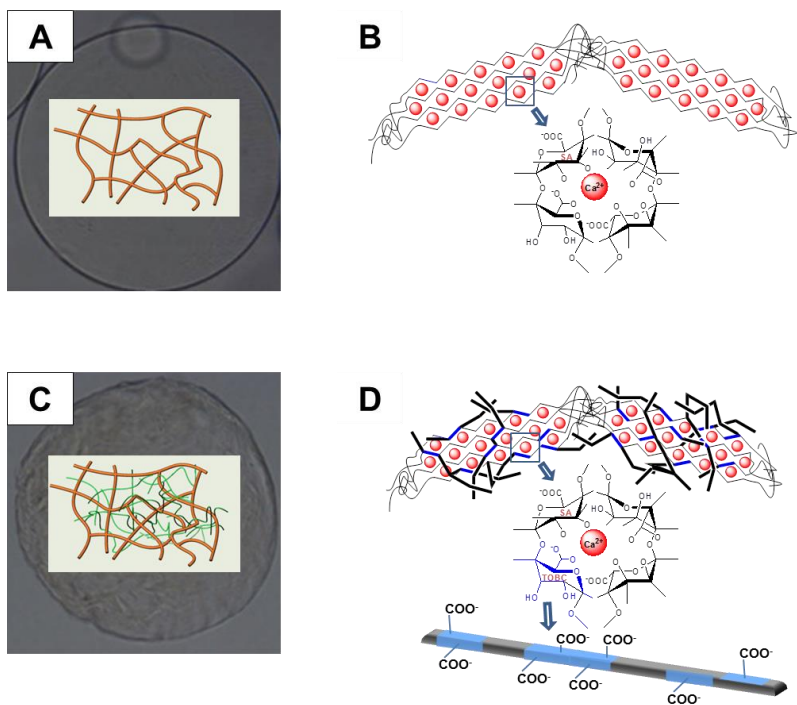


Figure 6-1. Schematic representation of alginate and TOBC beads. (A) Optical microscopy image of alginate bead and scheme of surface structure of alginate bead, (B) scheme of the structure of egg-box junction zones of alginate. (C) Optical microscopy image of alginate/TOBC bead and scheme of surface structure of alginate/TOBC bead, (D) scheme of the structure of egg-box junction zones of alginate/TOBC.

6.2. Materials and method

6.2.1. Preparation of TEMPO-mediated oxidized BC (TOBC)

The bacterial cellulose were oxidized by a 2,2,6,6-tetramethylpiperidine-1-oxyl (TEMPO)-mediated system. To obtain TEMPO-oxidized BC, 20 g hydrogels (wetting weight) were cut into small pieces then suspended in 500 mL distilled water containing 20 mg TEMPO and 0.5 g NaBr. And 15 mL 5% NaClO solution was added to the BC suspension to start the oxidation. The pH value was maintained at 10 using a NaOH solution. The mixture was vigorously agitated using a magnetic stirrer bar for 1 day. At the end of a reaction time, the oxidation was quenched by adding ethanol to the suspension. The products were collected by centrifugation at 15000rpm for 15min and dialyzed in a cellulose tube (Spectra/Por® , Spectrum Laboratories, Inc., USA, molecular weight cut off 12,000-14,000) against circulating purified water for 2 days at room temperature, and finally autoclaved at 120 °C for 20 min.

6.2.2. Preparation of alginate/TOBC beads

The extrusion technique was used for the preparation of the alginate/TOBC beads. Briefly, 2mL of cell suspension was mixed with 2 mL of autoclaved (121 °C, 20 min) sodium alginate solution containing with various content of TOBC. The cell suspension/polymer mixture (1 mL) was extruded through a capillary and dropped with N₂ gas blowing into a calcium chloride (2 %) bath for gelation. Following the encapsulation step, beads were

transferred to a tissue culture plate. The CaCl_2 solution was removed and the beads were washed with PBS (Gibco). The PBS was removed and replaced with cell culture medium.

6.2.3. Characterization of alginate/TOBC beads

Transmission images of both alginate/TOBC beads and encapsulated cells were captured under light microscope. Transmission electron microscopy (TEM, Leo-EM912 Omega, Carl Zeiss) was conducted at an acceleration voltage of 200 kV to observe the morphology of BC and TOBC. The morphologies of the samples were observed at an acceleration voltage of 2 kV using field emission scanning electron microscopy (FE-SEM, JSM-6330F, JEOL). The mechanical properties of alginate/TOBC beads (compression test) were investigated using a dynamical mechanical analyzer fitted with a 10 N load cell. For compression testing, the samples were prepared as sphere 2 mm in diameter and compressed to 40 % of their original thickness with a constant crosshead speed of 0.005 mm/s at room temperature. Three specimens were tested for each sample. Means and standard deviations are reported. Chemical resistance property was observed by soaked the beads for 1 h in 40 mM sodium citrate solution. Morphological changes of the beads were observed after soaking.

To evaluate the diffusion properties of alginate/TOBC beads, model molecules with different molecular weights were used; Dextran (Mw 4 kDa)

conjugated FITC, dextran (Mw 150 kDa) conjugated FITC. These were incubated 2 h with alginate/TOBC beads and their permeabilities were determined using confocal microscopy.

6.2.4. Viability and proliferation of encapsulated cells

Encapsulated cells were cultured in a humidified 5 % CO₂ incubator at 37 °C for 1, 3, and 5 days until examination. After incubation as function of days, encapsulated cells in same volume medium were recovered using 80mM sodium citrate and trypsin followed by centrifugation. The cells were calculated used by Petroff-Hausser counting chamber. To investigate the viability of encapsulated cells, cells were recovered using 80mM sodium citrate and centrifugation. And then Live/Dead fluorescence assay was performed and observed by an Olympus fluorescence microscope.

6.3. Results and discussion

6.3.1. Preparation of alginate/TOBC beads

The selective oxidation of BC at the C6 carbon was successfully performed using TEMPO (Figure 6-2). Figure 6-2B shows a relationship between the amount of added NaClO as the primary oxidant and carboxylate content. The carboxylate content was clearly increased by the addition of 5% NaClO up to 12 mL and slight increase in carboxylate content was observed during the addition of NaClO from 18 to 24 mL. The carboxylate content at

the point of 18 mL was 0.938 mmol/g which corresponded to approximately one carboxylate group per 3 cellulose repeating units on average. FT-IR spectra presented the modification of chains by carboxyl group asymmetric stretching band at 1602 cm^{-1} . On the other hand, stretching vibration band of C–H at $2896\sim 2990\text{ cm}^{-1}$ and stretching vibration band of –OH groups around $3345\sim 3539\text{ cm}^{-1}$ were reduced after the modification into TOBC [200-202] (Figure 6-2C). The effect of oxidation on the crystalline structure of BC was further investigated with XRD and TEM analysis. Because the TEMPO mediated oxidation of BC fibers only occurred at the surface of cellulose fibers, the original morphology such as aspect ratio of fibers and the integrity of the crystal were maintained. As shown in Figure 6-2D, TOBC still distinctly presented the diffraction peaks of BC at 2θ angles around 14, 16, and 22 [188, 200].

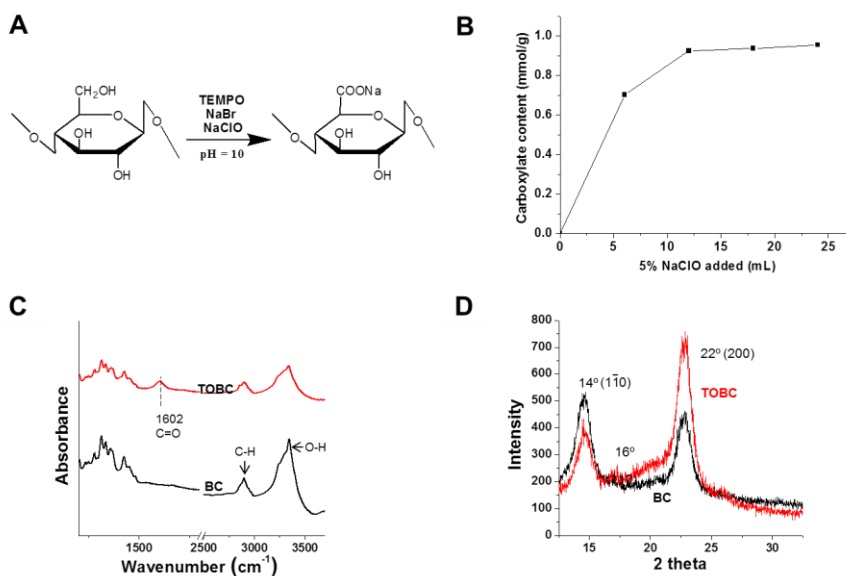


Figure 6-2. Selective oxidation of C6 primary hydroxyls of cellulose to carboxylate groups by TEMPO/NaBr/NaClO oxidation in water at pH 10. (A) Chemical structures of pure BC and TOBC, (B) A relationship between the amount of NaClO and the carboxylate content of the oxidized cellulose, (C) FT-IR spectra for pure BC and TOBC, and (D) X-ray diffraction patterns of the pure BC and TOBC.

Figure 6-3 showed the changes of morphology and dimension of BC before and after oxidization. Pure BC exhibited an entangled network-structure with a several micrometer in length and tens of nanometer in diameter. Although the length of fibers was slightly decreased, the fiber structure was maintained. The introduction of carboxyl groups at the surface of the BC fibrils increased the gaps between adjacent fibers as a result of repulsive interaction of anionic charges, thus forming a well dispersed state. TOBC nanofibers with a high aspect ratio were morphologically similar to the BC fibers but less bundles and networkings were observed due to the lack of adhesion between nanofibers.

Figure 6-4 shows the SEM images of the beads formed with different amount of TOBC in alginate/TOBC composite. While the surface of alginate beads was porous, the surface of alginate/TOBC beads became nonporous after TOBC was introduced into alginate because the mixture of TOBC nanofibers and alginate created the networked structure by coupling with divalent ions.

The intermolecular interactions between alginate and TOBC components were confirmed by FTIR analysis (Figure 6-5A). The peak at 1598 cm^{-1} is a characteristic carbonyl group of alginate. As the amount of TOBC added to alginate increased, the characteristic band shifted toward higher wavelength. Specifically, a peak located at 1598 cm^{-1} in alginate shifted to 1603 cm^{-1} with adding TOBC. The shift indicated that the carboxylic groups in TOBC could

be attributed to crosslinking network with alginate through ionic interactions [200]. Although alginate showed an amorphous structure, the crystallinity of alginate/TOBC composites gradually increased with the increase of cellulose content. It was confirmed from the diffraction peaks at 14°, 16°, and 22°, which were characteristic to the crystalline cellulose (Figure 6-5B).

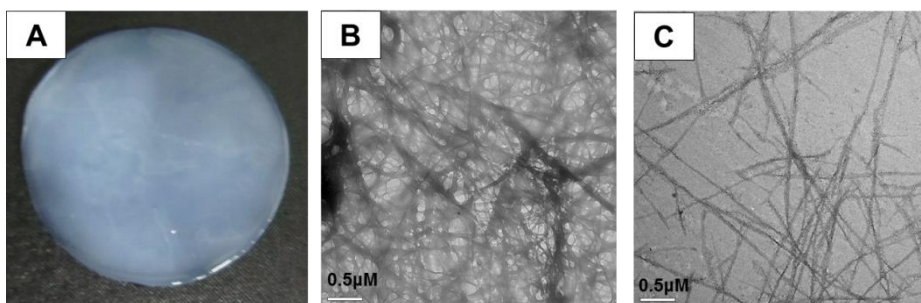


Figure 6-3. Preparation of the TOBC. (A) Optical image of pure BC, (B) TEM images of pure BC, and (C) TOBC.

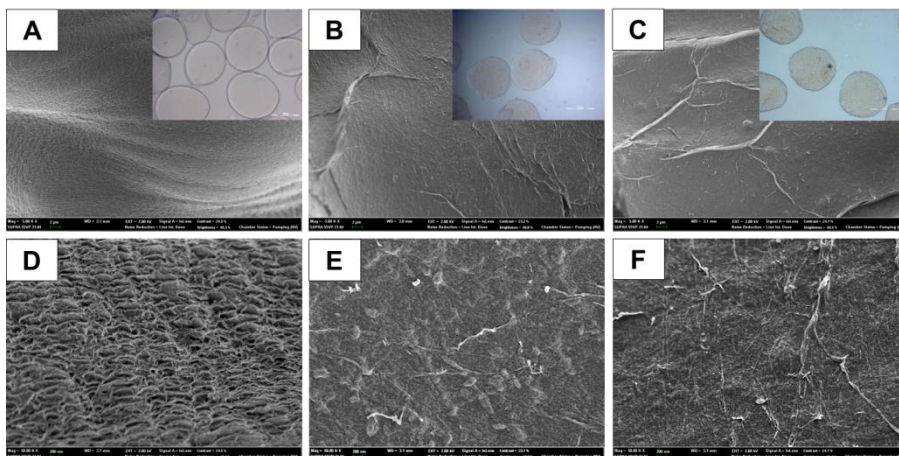


Figure 6-4. SEM images of surface morphology of alginate/TOBC microbeads regarding the TOBC content. (A) alginate beads, (B) alginate /TOBC10 beads and (C) alginate /TOBC20 beads. Inserted micrographs are optical images of each samples. (D~F) are magnified images of (A~C).

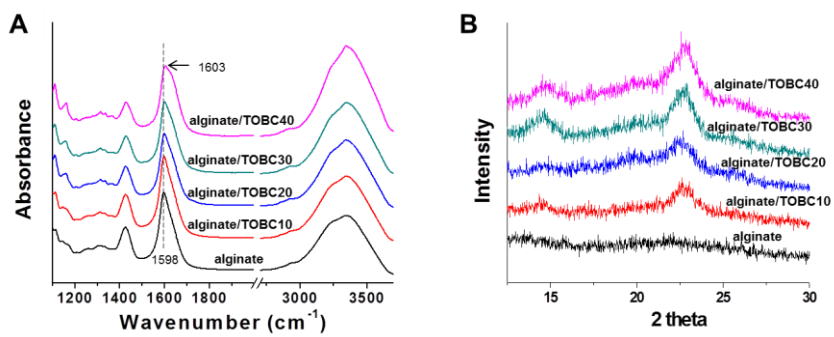


Figure 6-5. (A) FT-IR spectra for alginate /TOBC composites with various cellulose contents. (B) XRD patterns for alginate/TOBC composites with various TOBC contents.

6.3.2. Mechanical and chemical stability of alginate/TOBC

The compressive mechanical property of the alginate/TOBC composites was evaluated. As expected, the mechanical property of the composites depended on the contents of the TOBC. The compressive stress–strain curves showed that the addition of less than 20 % of TOBC formed more robust beads than the beads formed with alginate only. The compressive modulus of beads also increased as the contents of TOBC increased up to 20 % (Figure 6-6B). The results showed that introducing low content TOBC in the alginate hydrogel matrix enhanced the mechanical strength of the composites. TOBC could participate in the crosslinking reaction and make good conjunction with alginate playing a role of structural frames. However, the addition of more than 30 % of TOBC deteriorated the compressive strength of beads (Figure 6-6A). It was caused by the smaller number of COO^- groups in TOBC available for the ionic crosslinking with the alginate. The TOBC chains not involved in crosslinking made the composite have low mechanical strength.

The chemical stability of the beads was evaluated by soaking the beads in an aqueous solution of 40 mM sodium citrate for chelating with calcium. The morphological changes of the gel beads were observed after 6 and 60 min (Figure 6-7). The alginate beads soaked for 6 min in the solution were disintegrated and lost their spherical shape due to drastic swelling caused by the chelation of calcium ions (Figure 6-7B). 40 mM sodium citrate was found to be sufficient to extract most of calcium ions from alginate beads.

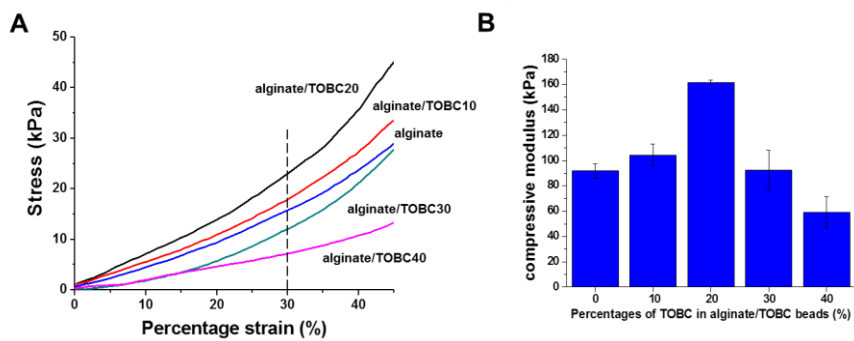


Figure 6-6. (A) Compressive stress-strain curves for various alginate/TOBC beads. (B) Compressive Modulus of various alginate/TOBC beads.

It is undesirable in biomedical applications because it would lead to lose immunoprotective properties and enhance host responses in body. The further exposure of the alginate beads to the sodium citrate solution for 60 min made them completely dissolved (Figure 6-7C). In contrast, the alginate/TOBC beads were observed to keep their spherical shape even after 60 min (Figure 6-7E and F). The existence of TOBC was effective in protecting from the swelling of alginate beads due to the tightly packed nanofibric structure (Figure 6-7G and H).

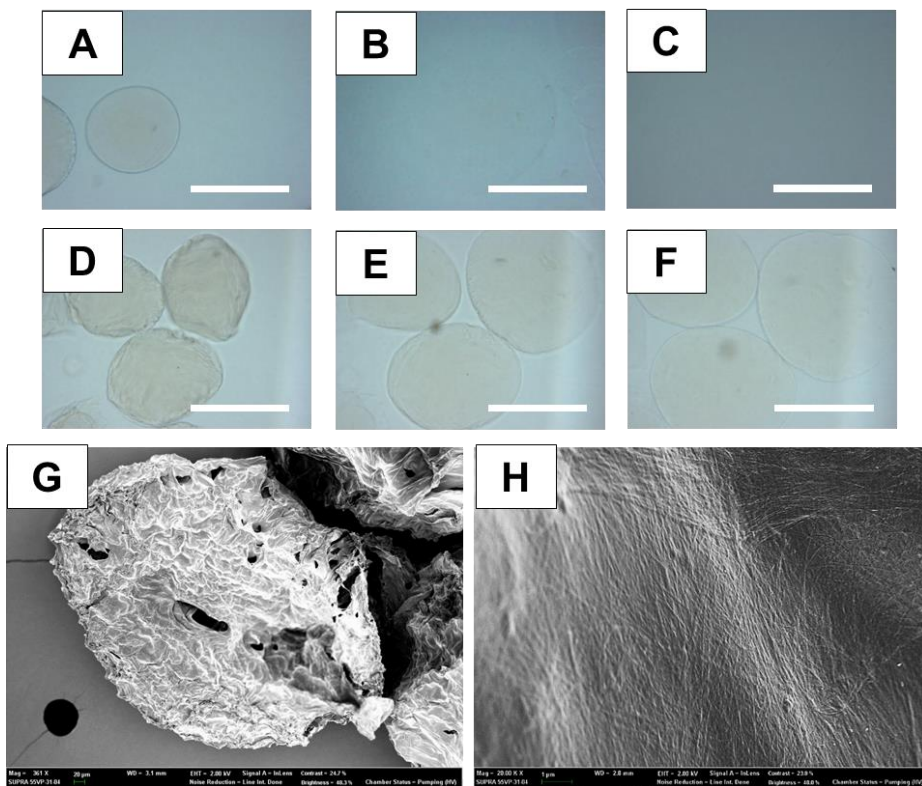


Figure 6-7. Microscopy images of alginate and alginate /TOBC20 microbeads as formed (A, D), after being exposed to 40mM sodium citrate in 6min(B, E) and 60min (C, F). Scale bar = 500 μ m (G) SEM images of alginate /TOBC20 microbeads after being exposed to 40mM sodium citrate in 60min. (H) is magnified images of (G).

6.3.3. Permeability of alginate/TOBC beads

Alginate/TOBC composite membrane could be permeable to small molecules like oxygen (16 Da), glucose (180 Da) or large molecules (growth factor ~30 kDa) for maintenance of cellular viability and function. Also, the BC composite membrane should not be permeable to host IgG antibodies (150 kDa) to protect the encapsulated cells from the host immune system. In addition, the alginate/TOBC composite membrane must be permeable to the therapeutic molecules (dopamine 153 Da, insulin 6 kDa) for the clinical application. To find out the permeable property of BC composite membrane, the permeability of alginate/TOBC beads was evaluated using 4 and 150 kDa FITC-dextran. Figure 6-8 is fluorescence microscopic images of beads containing 4 and 150 kDa FITC-dextran. Samples were incubated in water to investigate the permeability of samples. In all cases, 4 kDa FITC Dextran could release out of the beads. While, 150 kDa FITC-Dextran could not release out of the beads. Therefore, green fluorescence only existed inside of beads. Figure 6-9 is cross-sectional confocal images of beads to illustrate the permeability of different molecular weight FITC-dextran for all samples. Small molecules (4 kDa FITC-dextran) could penetrate the entire all beads within 2 h. Images showed high permeability of 4 kDa FITC-dextran for all samples (Figure 6-9A, C, and E). However after 2 h incubation, the bigger sized molecules (150 kDa FITC-dextran) could not penetrate into all beads. Therefore green fluorescence only existed outside of beads and the inside of the beads looked black (Figure 6-9 A, C, and E). Such a semi-permeable

property of alginate/TOBC would play an important role in protecting encapsulated cells from immune biomolecules but permeating oxygen and low molecular weight of biological compounds and secretory proteins needed the cells to survive and function [203].

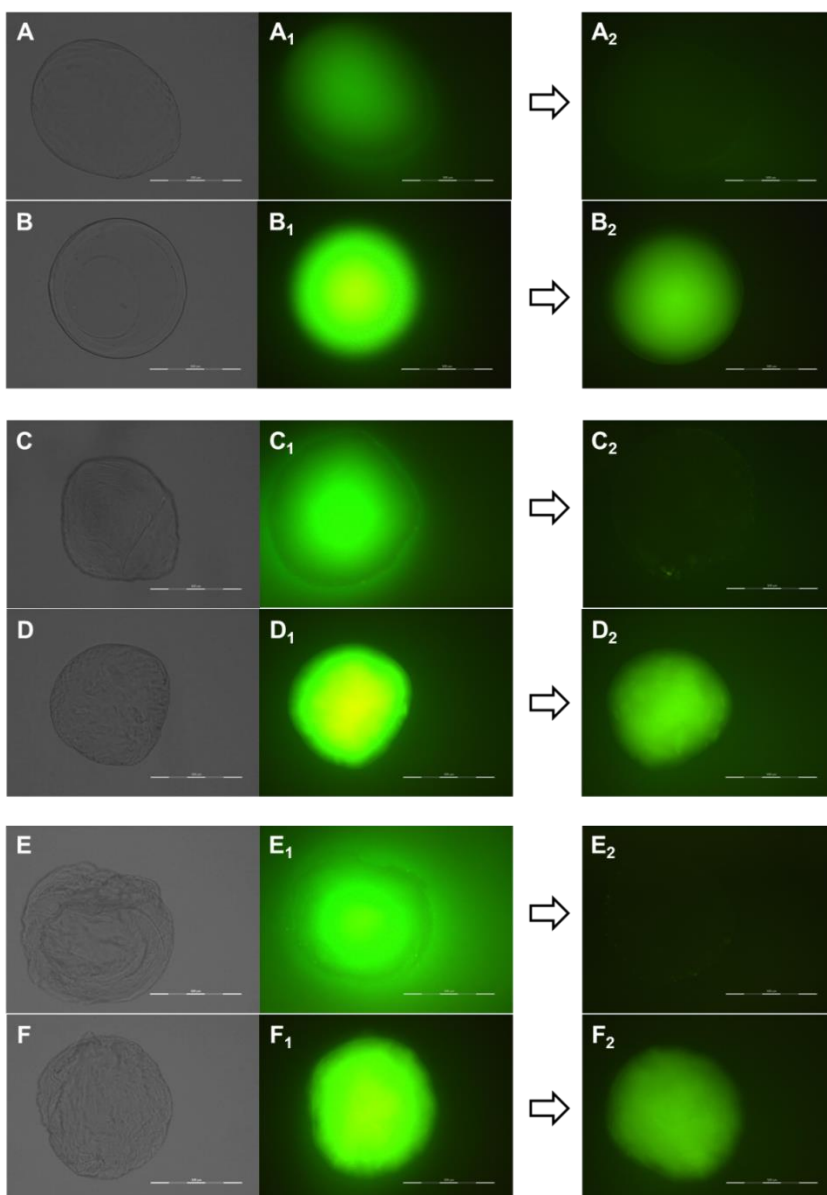


Figure 6-8. Fluorescence microscopic images for permeability assessment of various alginate/TOBC microbeads. Alginate beads with 4kDa FITC-Dextran (A) and 150kDa FITC-Dextran (B) was immersed in water. After 30min, 4kDa FITC-Dextran was released out of the beads (A2). 150kDa FITC-Dextran could not be released out of the beads. (B2). (C) and (D) are alginate/TOBC10 samples. (E) and (F) are alginate/TOBC20 samples.

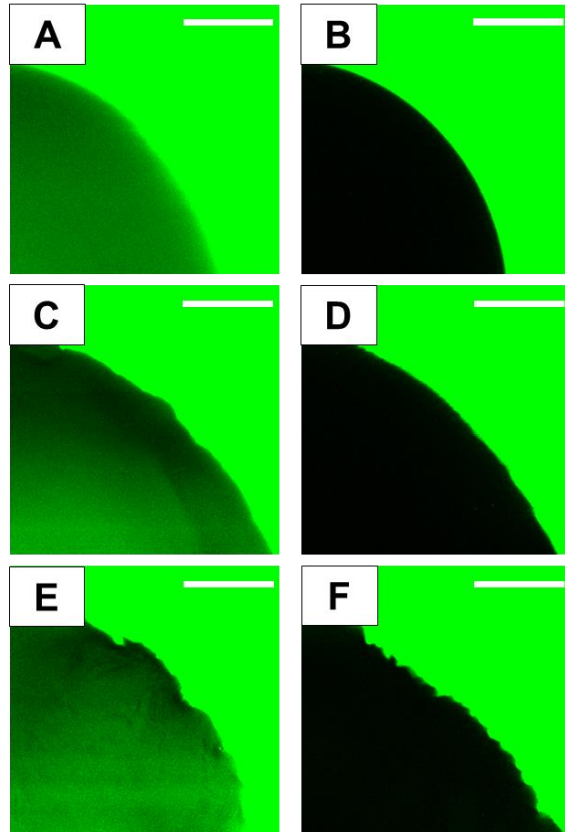


Figure 6-9. Confocal microscopy section images for permeability assessment of various alginate/TOBC microbeads. Alginate beads incubated with 4 kDa FITC-Dextran (A) and 150 kDa FITC-Dextran (B). Alginate/TOBC10 beads incubated with 4 kDa FITC-Dextran (C) and 150 kDa FITC-Dextran (D). Alginate/TOBC20 beads incubated with 4 kDa FITC-Dextran (E) and 150 kDa FITC-Dextran (F). Scale bar = 50 μm

6.3.4. Viability and proliferation of encapsulated cells

Figure 6-10 A to C are optical microscopy images of cells encapsulated in alginate, alginate/TOBC10, and alginate/TOBC20 beads after the incubation for 5 days. Cells were well encapsulated in each bead and proliferated by forming cell clusters as shown in the images. The cells from each bead incubated for a different day were collected and counted (Figure 6-10D). Cells encapsulated in alginate/TOBC10 and alginate/TOBC20 were more proliferated than cells in alginate beads.

Live/Dead staining experiments were conducted to investigate the viability of the cells encapsulated in beads (Figure 6-11). Cells recovered from the beads were still alive and the number of cells encapsulated in the beads containing TOBC nanofibers was larger than alginate beads. The cells could efficiently be encapsulated within the alginate/TOBC beads, retained a high level of cell viability and preserved their ability to proliferate. General, isolated single cells encapsulated in beads showed lower cell viability than aggregated cells. It meant that forming 3D aggregated cells was helpful to survive and proliferate since the nanofibrous structure of TOBC could improve the cell proliferation.

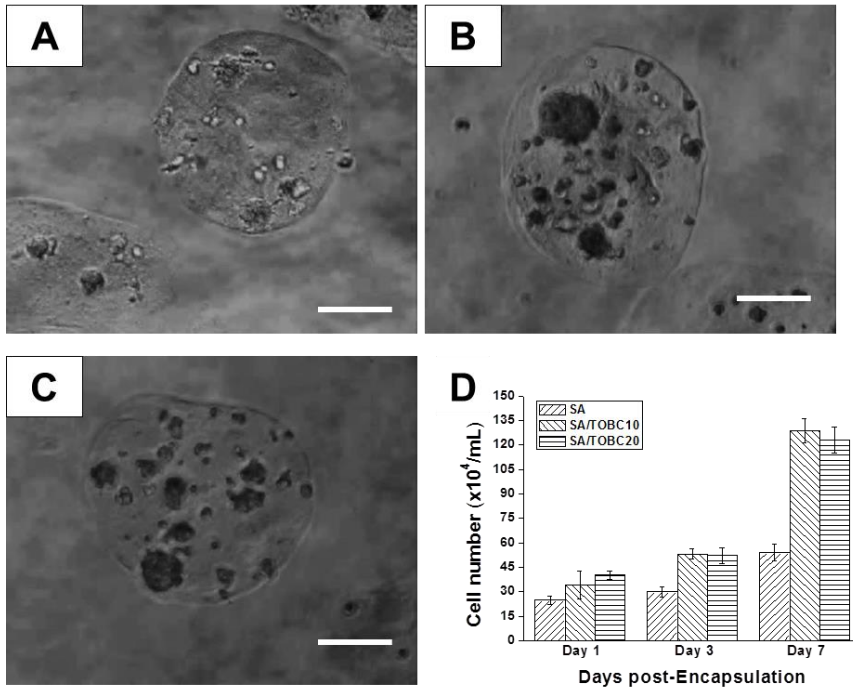


Figure 6-10. Optical microscopy images of cells encapsulated in alginate (A), alginate/TOBC (B), and alginate/TOBC20 (C). Cell numbers for various alginate/TOBC beads as function of cultured days. Scale bar=250 μ m

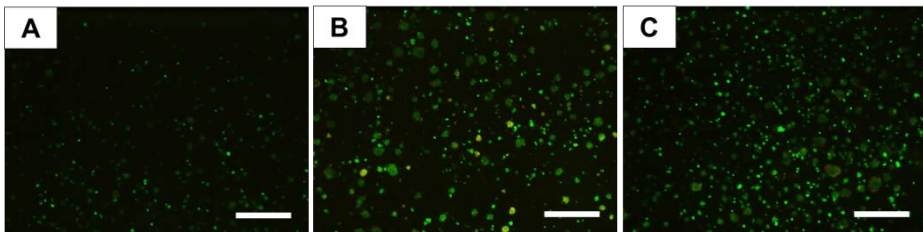


Figure 6-11. After recovering the cells from beads, Live/Dead staining were conducted. The fluorescence images are the staining results of cells encapsulated in alginate (A), alginate/TOBC10 (B), and alginate/TOBC20 beads (C). Scale bar=250 μ m

6.4. Summary

TEMPO-mediated oxidized bacterial cellulose (TOBC) improved the mechanical and chemical stability of the alginate beads. The incorporation of TOBC and SA was confirmed via the analysis of the chemical structure and crystallinity of the composite. The cells encapsulated in the beads tended to aggregate and form a cluster. Specifically, the cells encapsulated in the alginate/TOBC beads were more viable and proliferated more readily than were the cells in the SA beads due to the 3D fibrous contribution of TOBC, which was similar to the extracellular matrix. Alginate/TOBC composites are a potential candidate for the encapsulation of cells.

Chapter 7

**Thermoresponsive hybrid hydrogel of oxidized BC
using a elastin like polypeptide**

7.1. Introduction

Cellulose nanofibers-based hydrogel can be fabricated from disintegrated cellulose suspensions [35, 204], cellulose derivatives [205, 206], and cellulose-polymer blending [207, 208]. Recently, stimuli responsive cellulose-based hydrogels have been fabricated through chemical modifications or incorporating of polymers [209, 210]. Interestingly, carboxymethyl cellulose can be pH-responsive, with pKa around [186, 211]. Hydroxypropylmethyl cellulose is a temperature-responsive cellulose derivative exhibiting a sol-gel transition in aqueous solution at 41 °C [212, 213]. However, the gelation temperature is too high to encapsulate cells. UV light or electron-beam irradiation was reported for the fabrication of responsive cellulose hydrogels, but *in situ* encapsulation would be harmful to cells [209, 210].

Elastin-like polypeptide (ELP), an artificial smart polypeptide, has successfully prepared by a number of different strategies. ELPs are biopolymers of the pentapeptide repeat Val-Pro-Gly-Xaa-Gly derived from human tropoelastin, where the “guest residue” Xaa can be any of the natural amino acids except for Pro. Besides biocompatibility, biodegradability, and non-immunogenicity, stimuli-responsive characteristics, in particular their thermo-responsive characteristic, make ELPs a very promising candidate for drug delivery and other biomedical applications [214-217]. ELPs are soluble in aqueous solution below the inverse transition temperature (T_i), and once the

temperature is increased above T_t , ELPs will undergo a sharp phase transition accompanied by aggregation.

In this part, a thermoresponsive polysaccharide hydrogel based on BC and ELP was prepared for cell encapsulation. The thermoresponsive polysaccharide hydrogel of TOBC and ELP is unique because of reversible sol-gel transition by temperature and noncytotoxicity. Compared to permanent hydrogels using smaller size of crosslinkers, the polysaccharide hydrogel of TOBC and ELP is dissolvable to medium by simply decreasing a temperature. When TOBC and ELP were mixed together at lower temperature than T_t of ELPs, positively-charged ELPs were spontaneously grafted on the surface of negatively-charged TOBC due to the electrostatic interaction. ELPs took a role of “rope”, they folded and coacervated when temperature increased above T_t , leading TOBCs to be roped together and thereby a porous hybrid hydrogel of ELP and TOBC was formed (Figure 7-1). It will be a promising material in biotechnology and life sciences requiring smart properties such as cell encapsulation, tissue engineering and controlled drug release in the future.

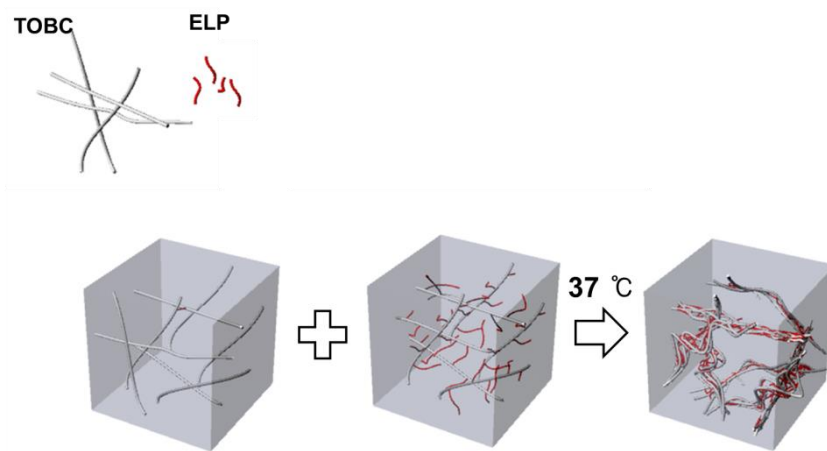


Figure 7-1. Schematic representation of the process for preparing ELP/BC hydrogel.

7.2. Materials and method

7.2.1. Elastin like polypeptide (ELP) synthesis

The ELP gene [(VPGVG)₁₄(VPGKG)]₈[VPGVG]₄₀ was oligomerized by recursive directional ligation and transformed into *E. coli* strain BLR (DE3) (Novagen, USA) for expression. The ELP was purified by inverse transition cycling and the collected ELP was freeze dried.

7.2.2. Sol-gel transition

TOBC/ELP solution (2 wt%, TOBC:ELP = 1:1) was prepared at 4 °C and then transferred to an incubator at 37 °C to trigger sol–gel phase transition. For comparison, pure TOBC and ELP solutions with a concentration of 1 wt% were also prepared at 4 °C and transferred to an incubator at 37 °C. After these solutions were heated to 37 °C and equilibrated for 30 min, the sol–gel transition was determined by vial inversion, which is a visual inspection of the sol–gel phase transition. After invert the vials, if samples can flow to the bottom, corresponding to solution, whereas, lack of flow corresponding to gel.

7.2.3. Characterization of ELP/TOBC

To determine the T_t of ELP and TOBC/ELP solution, OD_{350} was monitored by a UV–visible spectrophotometer equipped with a water circulating temperature controller (Mecasys, South Korea). The samples were

heated at a rate of 1 °C /min.

To further confirm hydrogel formation, dynamic rheological analysis was performed to determine the change in sample viscoelasticity as a function of temperature. Rheological measurements of ELP (2 wt%), TOBC (2 wt%) and TOBC/ELP (2 wt% for a 1:1 TOBC–ELP mixture) were performed using the Advanced Rheometric Expansion System (Rheometric Scientific, UK). Measurements were carried out by increasing temperature in the range of 25–40 °C at an angular frequency of 1.0 rad/s and a shear stress of 2.0 Pa.

Secondary ELP structure was determined by circular dichroism (CD) (Applied photophysics, UK) at different temperatures. ELP (0.5 mg/mL) and TOBC/ELP (1 mg/mL for a 1:1 TOBC-ELP mixture) solutions were prepared for CD analysis.

Zeta-potentials of ELP, TOBC and TOBC/ELP complexes were measured by dynamic light scattering (Zetasizer Nano, Malvern, UK) to determine the electrophoretic mobility of samples. All samples were suspended in deionized water, and measurements were carried out at 20 °C with folded capillary cells. Sample surface morphologies were imaged by atomic force microscopy (AFM, Park Science) with a non-contact mode (tip model, spring constant 42 N/m) in air. The pure TOBC and TOBC/ELP solutions were casted on a mica surface and dried at room temperature prior to AFM imaging. The inner morphologies of the TOBC solution, the TOBC/ELP

solution and the TOBC/ELP hydrogel were observed by imaging the cross-section of the samples by scanning electron microscope (SEM). SEM images were acquired with a SUPRA 55VP fieldemission SEM (Carl Zeiss, Germany). After samples were equilibrated at given temperatures, they were dipped into liquid nitrogen and freeze-dried. Freezedried samples were coated by gold sputter prior to SEM observation.

7.2.4. Cell viability and proliferation

NIH-3T3 fibroblast cells were chosen to perform MTT assay. The cells were maintained in Dulbecco minimal essential medium (DMEM) supplemented with 10 % fetal bovine serum (FBS), penicillin (100 U/mL), streptomycin (100 µg/mL), and HEPES (7.5 mM). Briefly, 200 µL of NIH-3T3 fibroblast cells were seeded on a 96 well plate at a density of 4×10^4 cells /well and incubated (37 °C, 5% CO₂) overnight to allow the cells to attach to surface of the wells. Sequentially, the medium was removed and the wells were washed with PBS. And then, 100 µL of fresh medium was added to each well followed by adding 100 µl of sterilized TOBC/ELP aqueous complex at a concentrations of 0.02–5 mg/mL, leading to a final concentrations of 0.01, 0.1,0.5,1.0, and 2.5 mg/mL. As a control, instead of TOBC/ELP aqueous complex, 100 µl of sterilized DW was added to the well and mixed with 100 µl fresh medium. And then, incubated for another 48 h in 5 % CO₂ at 37 °C. 20 µl of MTT solution (5 mg/mL in PBS) was added to each well and incubated for another 4 h. Next, the medium containing MTT

solution was aspirated and the crystallized product was dissolved in 100 μ L of DMSO and the absorbance of the suspension was measured at 570 nm using a plate reader. Cell viability (%) was calculated as (OD value of experimental sample/OD value of control sample) X 100 %.

The encapsulated cell's viability and proliferation was also evaluated. TOBC/ELP aqueous complex for cell encapsulation was autoclaved. NIH-3T3 fibroblast cells were seeded into the TOBC/ELP aqueous complex at 20 °C with a final concentration of 2×10^6 cells/mL. And then, the cell-containing TOBC/ELP complex was transferred to 37 °C humidified environmental incubator and incubated for 30 min in order to trigger the sol-gel transition. After confirming the cells were entirely encapsulated, the cells-containing gel was rinsed with pre-warmed DMEM medium prepared with the same method as mentioned in MTT assay section for several times in order to eliminate the remained water inside hydrogel. Encapsulated cells were cultured in a humidified 5 % CO₂ incubator at 37 °C for 2, 5, or 7 days until examination.

A live/dead viability fluorescence assay was performed by staining cells with a live/dead viability/cytotoxicity kit for mammalian cells (Invitrogen, USA). The combined live/dead assay reagents were added to cover hydrogel containing cells and then incubated for 30 min at room temperature in the dark. Cell viability was observed by fluorescence microscopy (BX51, Olympus, Japan). Fibroblast cells seeded and spread in a hydrogel were fixed with 2 % aqueous glutaraldehyde solution for 30 min followed by washing

with DI water and freeze-drying. Cell morphology in hydrogel was observed by FE-SEM (Carl Zeiss, Germany).

7.3. Results and discussion

7.3.1. Gel formation of ELP/TOBC

Pure ELP, pure TOBC and ELP/TOBC mixture solutions in vials all showed fluid-like states when the vials were inverted at 20 °C. The turbidity of pure ELP solution abruptly increased at 37 °C due to the hydrophobic aggregation of ELP molecules, but this mixture was still a fluid-like ELP suspension. Conversely, the temperature increase enabled hydrogel formation from the ELP/TOBC mixture, as shown in Figure 7-2. To determine the critical temperature that induces hydrogel formation, changes in the turbidity of ELP/TOBC mixtures were measured with thermo-regulated UV/vis spectrometer at 350 nm as a function of temperature. The phase transition of ELP/TOBC complexes started at around 26 °C, a much lower temperature (Figure 7-3B) than the pure ELP solution (Figure 7-3A). ELPs were adsorbed onto the surface of TOBCs due to electrostatic interactions, leading to a very high local concentration of ELPs on the surface of TOBC.

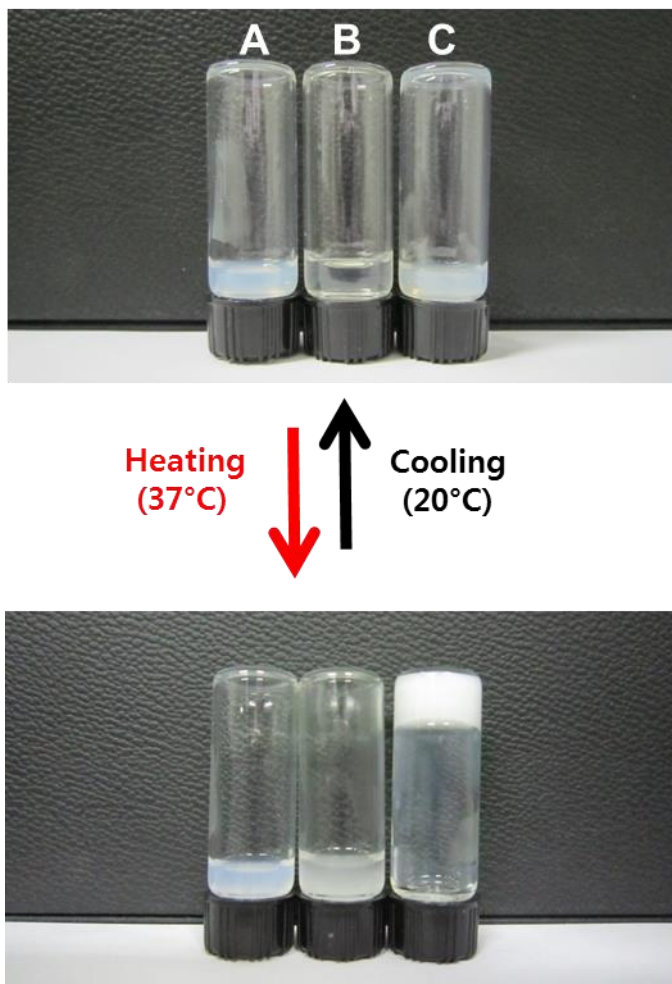


Figure 7-2. Temperature-triggered sol-gel transition of the ELP/TOBC complex. (A) TOBC only, (B) ELP only, and (C) ELP/TOBC.

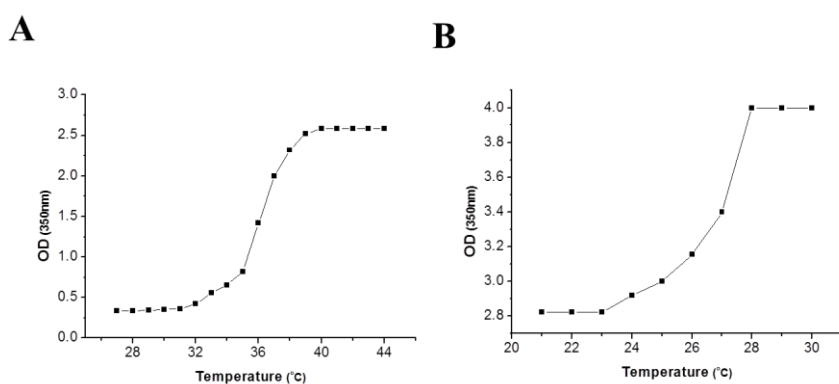


Figure 7-3. Turbidity variations of ELP (A) and ELP/TOBC (B) solution as a function of temperature (OD at 350 nm, Heating: 1 °C/min).

7.3.2. Rheological analysis of ELP/TOBC hydrogel

Dynamic rheology is one of the most direct and reliable way to determine the sol–gel transition of polysaccharide hydrogels [218, 219]. The rheological properties of the cellulose suspensions [220] and the aggregation of the cellulose fibers [221] have been studied by mixing different polymers with cellulose suspension. Hydrogel formation was confirmed by dynamic rheological analysis, which determined the change in sample viscoelasticity as a function of temperature. Measurements were carried out at angular frequency of 1.0 rad/s and shear stress of 2.0 Pa. For both TOBC/ ELP complex and pure TOBC solutions, the elastic modulus (G') was always higher than the viscous modulus (G'') throughout the whole temperature range, as shown in Figure 7A and B, indicating that elasticity was dominant at both low and high temperatures [219]. In other words, either the TOBC/ELP complex or the pure TOBC solution was not a free-flowing fluid but a viscous semi-solid or semi-transparent swollen gel at temperatures lower than the T_t of ELP [49, 220]. This is possibly due to the high concentration and relatively large size of TOBCs. For the TOBC/ELP complex, G' increased dramatically as temperature increased. This is due to the transition of semitransparent swollen gel to nontransparent shrunken/solid gel. The decline of both G' and G'' at temperatures above the T_t of ELP was due to phase separation, leading to the formation of a biopolymer-rich phase and water-rich phase. The sharp enhancement of G' at around 30 °C was caused by the folding and

coacervation of ELPs adsorbed onto the surface of TOBC, which acted as a physical crosslinker between TOBC chains. Meanwhile, G' and G'' of TOBC/ELP complex were significantly decreased after the transition compared with pure ELP solution (Figure 7-4A and C). It resulted from relatively stiff cellulose nanofibers to hinder aggregation of ELP molecules adsorbed onto the surface [220]. The sharp enhancements of both G' and G'' were not observed for pure TOBC solution as temperature increased (Fig. 3b). However, a sharp enhancement in G' was observed for pure ELP solution as temperature increased. This indicates that colloidal ELP particles precipitated when the temperature increased, leading to a gel-like film on the detecting plate surface.

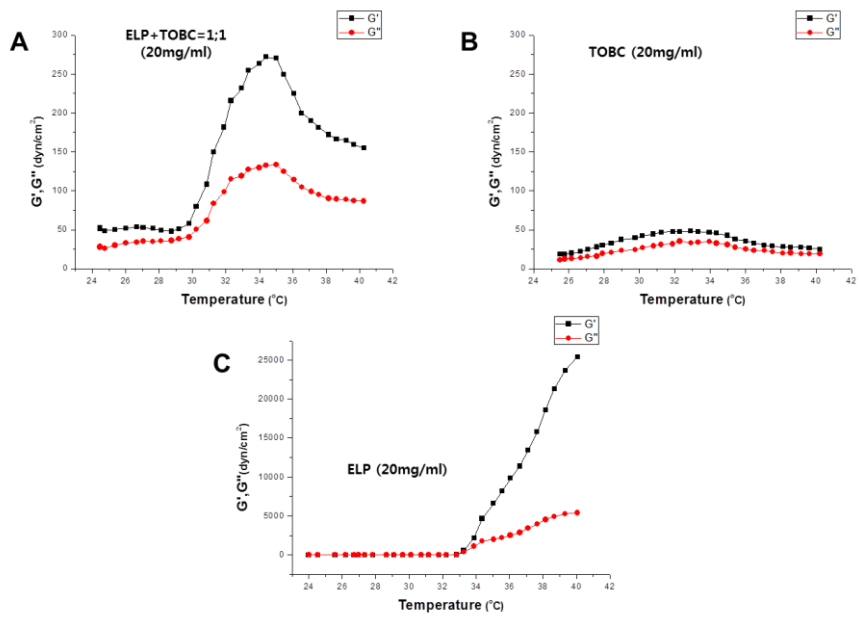


Figure 7-4. Oscillatory temperature ramp measurements to confirm hydrogel formation. (A) ELP/TOBC complex, (B) pure TOBC solution, (C) pure ELP solution. (Heating rate: 2 °C /min. Concentration of samples: 2 wt%).

7.3.3. Morphological analysis of ELP/TOBC hydrogel

After the temperature change of TOBC solution, TOBC/ELP solution and TOBC/ELP hydrogel, the samples were immediately dipped into liquid nitrogen and then freeze-dried to keep the morphological differences at the temperatures. As shown in FE-SEM images, TOBC fibers were closely packed in pure TOBC (Figure 7-5A and A₁). The density of TOBC fibers stored in TOBC/ELP solution at 20 °C was lower than the density in pure TOBC solution (Figure 7-5B and B₁). TOBC, ELP and water were evenly mixed together to form a single aqueous phase system. The phase separation phenomenon occurred as the hydrogel was formed at 37 °C, leading to two aqueous phases inside the hydrogel, the biopolymer (ELP and TOBC)- rich phase and water-rich phase. The water-rich phase formed pores after freeze-drying due to the removal of water from the region (Figure 7-5C and C₁). ELPs were adsorbed onto the surface of TOBCs by electrostatic interactions (Figure 7-5B₂), just as with previously reported protein/polysaccharide systems [222-224]. When the temperature increased above T_t , ELP transitioned from hydrophilic to hydrophobic states by exposing its hydrophobic side groups, driving ELPs to fold and coacervate by hydrophobic interactions. Therefore, TOBCs were held together when temperatures increased above T_t due to the coacervation of ELPs adsorbed onto their surface. In addition, strong hydrophobic interactions between ELPs led to the formation of TOBC/ELP hybrid hydrogel by crosslinking TOBCs tightly (Figure 7-5C₂). Due to high water content in the water-rich phase, pores were

left by water sublimation after lyophilization, as shown in Fig. 7-5C and C₁.

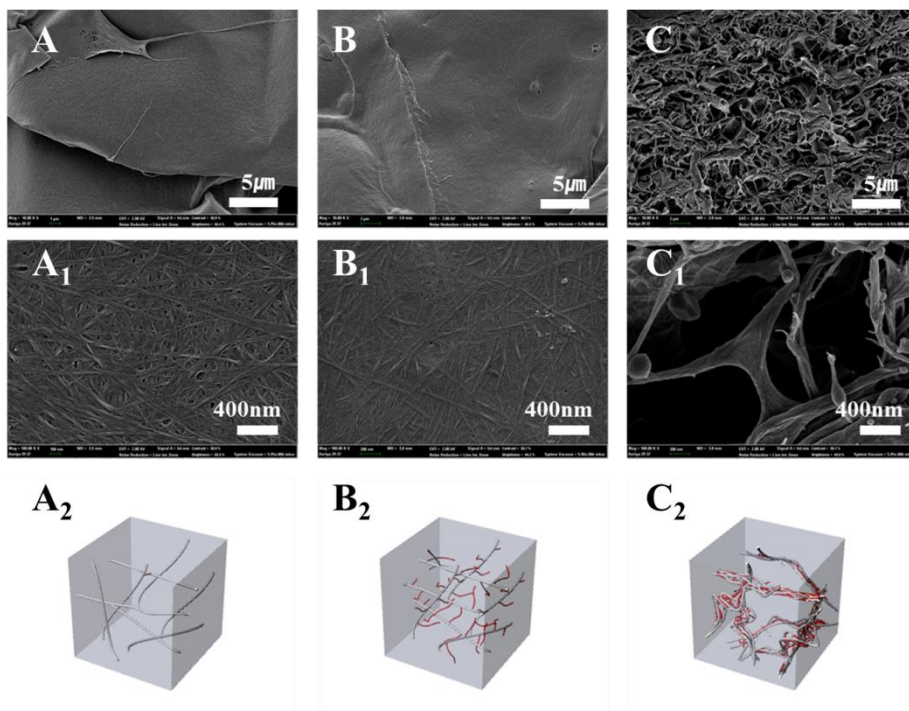


Figure 7-5. FE-SEM images of freeze-dried TOBC (A and A₁), ELP/TOBC solution (B and B₁), and ELP/TOBC shrunken hydrogel (C and C₁). Schematic representation of TOBC (A₂), ELP/TOBC solution (B₂), and ELP/TOBC hydrogel (C₂).

7.3.4. Mechanism of TOBC/ELP hydrogel formation

Zeta potential is widely used for quantification of the magnitude of the electrical charge at the double layer. Although zeta potential is not equal to the electric surface potential in the double layer, zeta potential is often the only available path for characterization of double-layer properties. From the experimentally-determined electrophoretic mobility, pure ELP showed a positive surface potential (or surface charge) in distilled water at pH 6 due to its lysine residues (Figure 7-6A). Conversely, TOBC had a very strongly negative surface potential at pH 6 as a result of TEMPO-oxidation. When TOBC and ELP were mixed together, this strongly negative surface potential became weakened dramatically. AFM height images verified the morphological differences between pure TOBC and TOBC/ELP complex (Figure 7-6B). The root mean square roughness (R_q) of a TOBC/ELP layer was ~11 nm. It showed a smoother surface compared with a TOBC layer (R_q ~ 13 nm). TOBC nanofibers became thicker due to ELP molecules adsorbed onto the surface. The obvious difference in morphology was another strong evidence that positively-charged ELPs were spontaneously adsorbed onto the surface of negatively-charged TOBC nanofibers through the electrostatic interaction.

When the positively charged ELPs were deprotonated at high pH, the TOBC/ELP mixture lost its ability to form a hydrogel. The pKa of the α -amino group at the ELP N-terminus and the ϵ -amino group in the ELP lysine

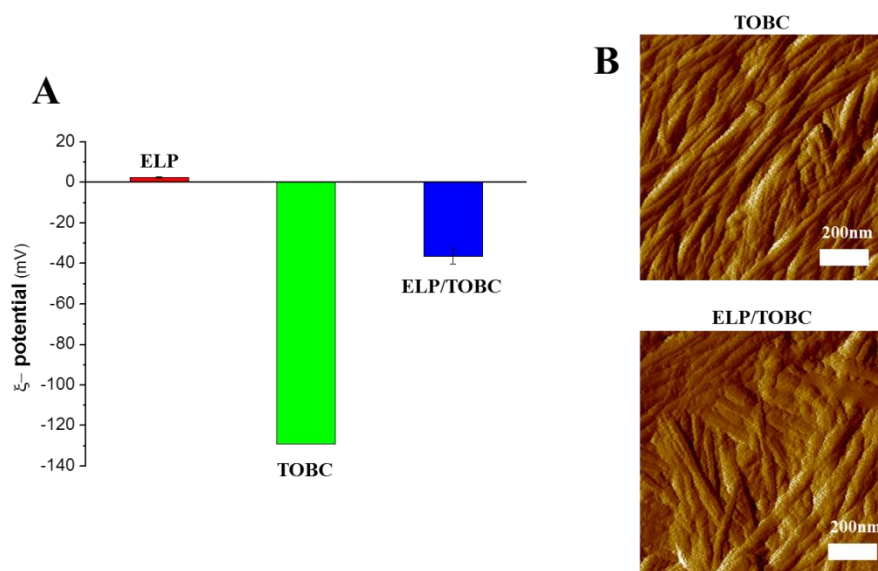


Figure 7-6. (A) Zeta potential for individual biopolymers and biopolymer composites at 20 °C, and (B) AFM images of TOBC and ELP/TOBC composites.

are 8.9 and 10.5, respectively. The medium was adjusted to pH 12 to eliminate positive surface charges of ELP derived from primary amines. As shown in Figure 7-7, a free-flowing milky suspension was formed instead of a shrunken hydrogel when the temperature increased to 37 °C. This was similar to the behavior of pure ELP solution, shown in Figure 7-2. ELPs were adsorbed onto the TOBC surface through electrostatic interactions at pH 6 to form a polypeptide-polysaccharide complex [224]. Although phase separation is a very common phenomenon in biopolymer mixtures, many researchers have demonstrated that this is not the case for mixtures consisting of protein/polypeptide and charged polysaccharide [225-227]. To confirm whether ELP chains were adsorbed onto the surface of TOBC backbones, the secondary ELP structure was determined through CD and fluorescence measurements in the presence and absence of TOBC (Figure 7-8). Pure ELP had a disordered secondary structure with a negative peak around 198 nm at 10 °C. However, the intensity of this negative peak was enhanced when pure ELP was mixed with TOBC, indicating that the random-coil based disordered structure of ELP increased dramatically. Altered secondary structure in the presence of TOBC was consistent with previous reports by other groups that reported that the extent of protein secondary structures increased with interactions between protein and polysaccharide [224]. ELP molecules transitioned into a more ordered state with a positive peak around 212 nm when the temperature increased to 50 °C, indicating a beta-turn structure [228-230]. The more interesting result was that ELPs were more disordered in

the presence of TOBC despite the high temperature. This result was in the opposite direction of pure ELP. This extraordinary phenomenon was attributed to the strong electrostatic interaction between ELP and TOBC.

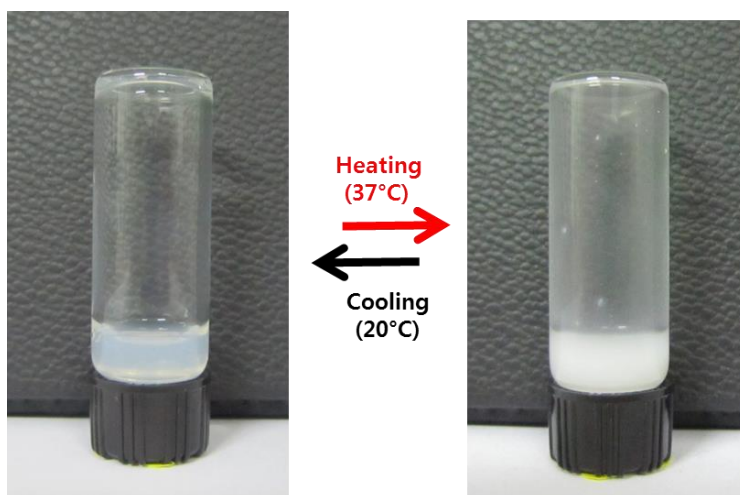


Figure 7-7. Effect of pH at pH12 on the formation of ELP/TOBC hydrogels. The ELP/TOBC solution was adjusted to pH 12 to eliminate positive charges on the ELP molecules. The resulted in the inability to form a hydrogel despite increased temperature.

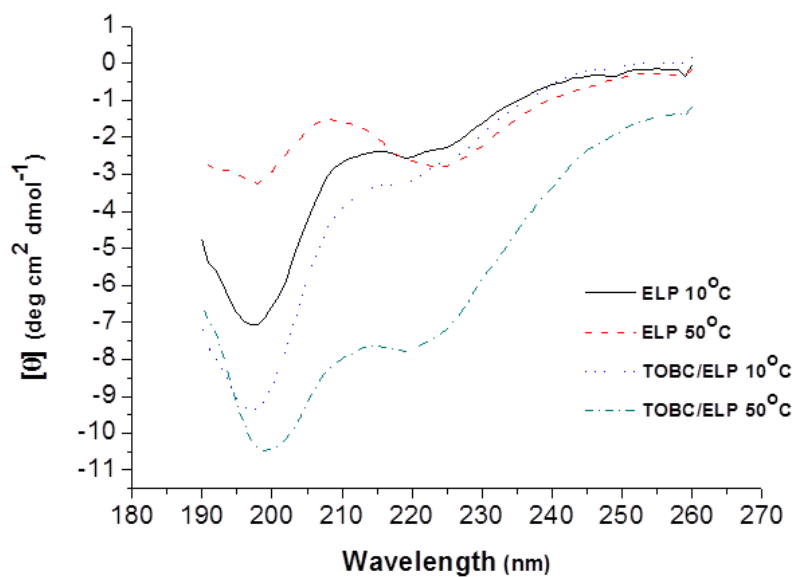


Figure 7-8. CD spectra of ELP/TOBC and ELP obtained at different temperatures in water. ELP concentration was 0.5 mg/mL in both the ELP/TOBC and pure ELP solutions.

7.3.5. Viability and proliferation of cells

MTT assay was used to assess the biocompatibility of TOBC/ELP complexes and the proliferation of NIH- 3T3 fibroblast cells. Cell viability (%) was calculated as the ratio of experimental sample OD value to the control OD value. High fibroblast viability was observed regardless of TOBC/ELP concentration, as shown in figure 7-9A, indicating that the TOBC/ELP complex was not cytotoxic. The viability of encapsulated cells was investigated by live/dead staining. As shown in figure 7-9B and C, the number of green spots inside the hydrogel increased after 7 days of incubation, indicating that most encapsulated cells remained alive and continued to proliferate inside the hydrogel.

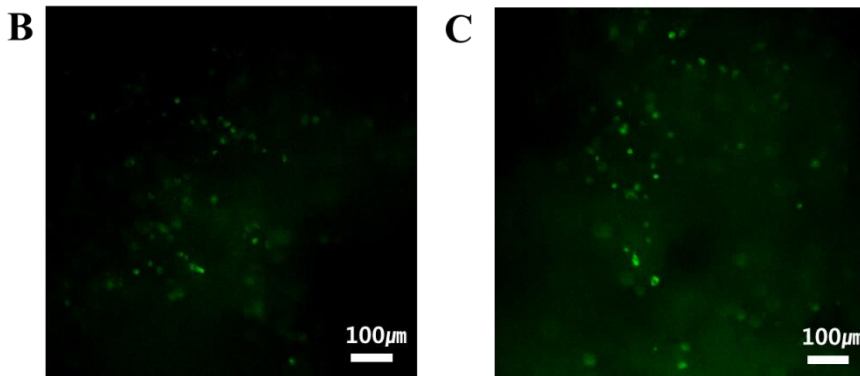
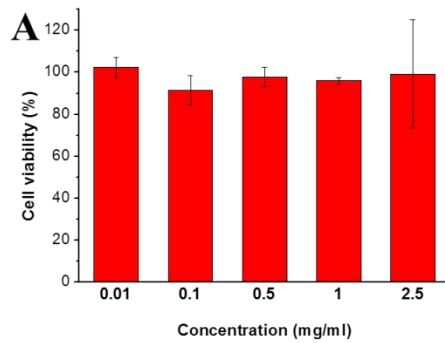


Figure 7-9. (A) MTT results of ELP/TOBC solution, (B, C) Fluorescence microscopic images of fibroblast cells encapsulated in a ELP/TOBC hydrogel after (B) 1 day and (C) 7 days of incubation (cells were live/dead stained).

7.4. Summary

A thermoresponsive hybrid hydrogel was prepared by mixing negatively charged TOBC nanofibers and positively charged ELP molecules containing lysine residues. Positively charged ELPs were bound to the surface of negatively charged TOBC by electrostatic interactions to form a single phase. Increased temperature triggered ELP folding and aggregation, leading to the formation of a TOBC/ELP hybrid hydrogel. Conformational analyses based on CD supported the occurrence of electrostatic interactions between TOBC and ELP. A cytotoxicity test showed that the TOBC/ELP hydrogel was suitable for encapsulating cells, indicating its potential for biomedical applications.

Chapter 8

Conclusions

8. Conclusions

The aim of this study was to design a variety of functional nanocomposites based on BC and motivate the application of BC composites. The studies on the synthetic methods and the applications of the BC nanocomposites were the key factors to contribute in broadening the knowledge about BC. Three different methods were used to introduce nanoparticles in BC: (1) biosynthesis, (2) dipping, and (3) in-situ synthesis method. To select an appropriate method among these, several factors such as the synthesis conditions, size, dispersibility in the nanoparticle medium, and affinity with BC fibers and nanoparticles should be considered. In the biosynthesis method, nanoparticles were dispersed in a culture medium to produce BC composites. In this case, it was important to consider the dispersibility and the size of particles because non-dispersed particles hinder the production of uniform composite and too small-sized particles (<100 nm) could come out from the space between BC 3D-network. Dipping is a simple and mild method for introducing nanoparticles in BC. However, the diameter of the particles used in dipping should be smaller than 200 nm to assure the penetration into the inner parts of the BC membrane, which exhibits a pore size of several tens to several hundred nanometers. With the *in-situ* methods, nanoparticles with a very high density were synthesized on the fibers. In this process, the BC nanofibers were used not only as a template but also as an immobilized reducing agent owing to the presence of abundant hydroxyl

groups on the BC fibers. To obtain homogenous BC composites with biopolymers in solution, the BC fibers were also well dispersed in biopolymer solutions. In this case, the dissolved or colloidal suspended BC could be effective. To produce individual cellulose fibrils dispersed in water, the TEMPO-oxidation process was employed because this oxidation process could reduce the adhesion between the cellulose fibrils by breaking the inter-fibril hydrogen bonds by electrostatic repulsion of nanofibers. In this study, a series of BC based nanocomposites incorporated with inorganic nanoparticles or biopolymers were successfully prepared by employing suitable synthesis methods. Their potential applications in electronics, sensor, and medical fields were examined as follows: (1) composites exhibiting both magnetic and electrical properties, which could be used as an electromagnetic shielding film, were prepared by the biosynthesis method, (2) flexible and conductive composites those could be used as flexible electrodes of lithium ion batteries were prepared by the dipping method, (3) composites for the surface-enhanced Raman scattering (SERS) sensor applications were prepared by the *in-situ* method, (4) composites for improved cell encapsulation, and (5) thermosensitive hydrogel composites for cell encapsulation were prepared by modification and blending method. These BC composites not only improved the natural properties of the materials (such as physical, chemical and biological properties), but also imparted new properties such as magnetic, conductive, sensing, and thermoresponsive properties to BC. The findings in this study indicated that BC exhibits a great potential for producing novel

composite materials, thereby opening new opportunities in the development of nanomaterials with designed functionalities. By combining the unique physicochemical properties of BC and various functionalities of guest substrates, significant synergetic effects can be obtained. The designing of several synthetic methods and the examination of the applications of various BC composites compiled in these studies would provide valuable insights in developing BC composites in the future.

References

- [1] D. Klemm, F. Kramer, S. Moritz, T. Lindstrom, M. Ankerfors, D. Gray and A. Dorris, Nanocelluloses: A New Family of Nature-Based Materials, *Angew Chem Int Edit*, 50 (2011) 5438-5466.
- [2] A. Bendahou, Y. Habibi, H. Kaddami and A. Dufresne, Physico-Chemical Characterization of Palm from Phoenix Dactylifera-L, Preparation of Cellulose Whiskers and Natural Rubber-Based Nanocomposites, *J Biobased Mater Bio*, 3 (2009) 81-90.
- [3] A. Bendahou, H. Kaddami and A. Dufresne, Investigation on the effect of cellulosic nanoparticles' morphology on the properties of natural rubber based nanocomposites, *Eur Polym J*, 46 (2010) 609-620.
- [4] M. Mariano, N. El Kissi and A. Dufresne, Cellulose nanocrystal reinforced oxidized natural rubber nanocomposites, *Carbohydr Polym*, 137 (2016) 174-183.
- [5] S. Varghese and J. Karger-Kocsis, Natural rubber-based nanocomposites by latex compounding with layered silicates, *Polymer*, 44 (2003) 4921-4927.
- [6] X.P. Shen, J.L. Shamshina, P. Berton, G. Gurau and R.D. Rogers, Hydrogels based on cellulose and chitin: fabrication, properties, and applications, *Green Chem*, 18 (2016) 53-75.
- [7] E. Robles, A.M. Salaberria, R. Herrera, S.C.M. Fernandes and J. Labidi, Self-bonded composite films based on cellulose nanofibers and chitin nanocrystals as antifungal materials, *Carbohydr Polym*, 144 (2016) 41-49.

- [8] J. Ma and Y. Sahai, Chitosan biopolymer for fuel cell applications, *Carbohydr Polym*, 92 (2013) 955-975.
- [9] T.H.T. Mahmud, A. Abdul-Aziz and R. Muda, A Review on the Potential Use of Chitosan-Based Delivery System in Mild Facial Cleansing Formulation, *Int J Polym Mater Po*, 64 (2015) 432-437.
- [10] T. Mukherjee and N. Kao, PLA Based Biopolymer Reinforced with Natural Fibre: A Review, *J Polym Environ*, 19 (2011) 714-725.
- [11] Z. Skrbic and V. Divjakovic, Temperature influence on changes of parameters of the unit cell of biopolymer PHB, *Polymer*, 37 (1996) 505-507.
- [12] N. Chiaoprakobkij, N. Sanchavanakit, K. Subbalekha, P. Pavasant and M. Phisalaphong, Characterization and biocompatibility of bacterial cellulose/alginate composite sponges with human keratinocytes and gingival fibroblasts, *Carbohydr Polym*, 85 (2011) 548-553.
- [13] K.H. Bouhadir, K.Y. Lee, E. Alsberg, K.L. Damm, K.W. Anderson and D.J. Mooney, Degradation of partially oxidized alginate and its potential application for tissue engineering, *Biotechnol Progr*, 17 (2001) 945-950.
- [14] Q. Wang, J.P. Zhang and A.Q. Wang, Preparation and characterization of a novel pH-sensitive chitosan-g-poly (acrylic acid)/attapulgit/sodium alginate composite hydrogel bead for controlled release of diclofenac sodium, *Carbohydr Polym*, 78 (2009) 731-737.
- [15] H.P.S.A. Khalil, A.H. Bhat and A.F.I. Yusra, Green composites from sustainable cellulose nanofibrils: A review, *Carbohydr Polym*, 87 (2012) 963-979.

- [16] K. Van de Velde and P. Kiekens, Biopolymers: overview of several properties and consequences on their applications, *Polym Test*, 21 (2002) 433-442.
- [17] C.S.R. Freire, S.C.M. Fernandes, A.J.D. Silvestre and C.P. Neto, Novel cellulose-based composites based on nanofibrillated plant and bacterial cellulose: recent advances at the University of Aveiro - a review, *Holzforschung*, 67 (2013) 603-612.
- [18] S.J. Eichhorn, A. Dufresne, M. Aranguren, N.E. Marcovich, J.R. Capadona, S.J. Rowan, C. Weder, W. Thielemans, M. Roman, S. Renneckar, W. Gindl, S. Veigel, J. Keckes, H. Yano, K. Abe, M. Nogi, A.N. Nakagaito, A. Mangalam, J. Simonsen, A.S. Benight, A. Bismarck, L.A. Berglund and T. Peijs, Review: current international research into cellulose nanofibres and nanocomposites, *J Mater Sci*, 45 (2010) 1-33.
- [19] S. Kalia, A. Dufresne, B.M. Cherian, B.S. Kaith, L. Averous, J. Njuguna and E. Nassiopoulos, Cellulose-Based Bio- and Nanocomposites: A Review, *Int J Polym Sci*, (2011).
- [20] R.J. Moon, A. Martini, J. Nairn, J. Simonsen and J. Youngblood, Cellulose nanomaterials review: structure, properties and nanocomposites, *Chem Soc Rev*, 40 (2011) 3941-3994.
- [21] S. Shankar and J.W. Rhim, Preparation of nanocellulose from micro-crystalline cellulose: The effect on the performance and properties of agar-based composite films, *Carbohydr Polym*, 135 (2016) 18-26.
- [22] M. Ul-Islam, S. Khan, M.W. Ullah and J.K. Park, Bacterial cellulose

composites: Synthetic strategies and multiple applications in bio-medical and electro-conductive fields, *Biotechnol J*, 10 (2015) 1847-1861.

[23] X. Chen, F.S. Yuan, H. Zhang, Y. Huang, J.Z. Yang and D.P. Sun, Recent approaches and future prospects of bacterial cellulose-based electroconductive materials, *J Mater Sci*, 51 (2016) 5573-5588.

[24] I. Siro and D. Plackett, Microfibrillated cellulose and new nanocomposite materials: a review, *Cellulose*, 17 (2010) 459-494.

[25] M.T. Postek, A. Vladar, J. Dagata, N. Farkas, B. Ming, R. Wagner, A. Raman, R.J. Moon, R. Sabo, T.H. Wegner and J. Beecher, Development of the metrology and imaging of cellulose nanocrystals, *Meas Sci Technol*, 22 (2011).

[26] Y. Nishiyama, P. Langan and H. Chanzy, Crystal structure and hydrogen-bonding system in cellulose I beta from synchrotron X-ray and neutron fiber diffraction, *J Am Chem Soc*, 124 (2002) 9074-9082.

[27] H. Yamamoto and F. Horii, In-Situ Crystallization of Bacterial Cellulose .1. Influences of Polymeric Additives, Stirring and Temperature on the Formation Celluloses I-Alpha and I-Beta as Revealed by Cross-Polarization Magic-Angle-Spinning (Cp/Mas) C-13 Nmr-Spectroscopy, *Cellulose*, 1 (1994) 57-66.

[28] A. Dufresne, Nanocellulose: a new ageless bionanomaterial, *Mater Today*, 16 (2013) 220-227.

[29] P. Gatenholm and D. Klemm, Bacterial Nanocellulose as a Renewable Material for Biomedical Applications, *Mrs Bull*, 35 (2010) 208-213.

- [30] T. Zimmermann, E. Pohler and T. Geiger, Cellulose fibrils for polymer reinforcement, *Adv Eng Mater*, 6 (2004) 754-761.
- [31] H. Yousefi, M. Faezipour, S. Hedjazi, M.M. Mousavi, Y. Azusa and A.H. Heidari, Comparative study of paper and nanopaper properties prepared from bacterial cellulose nanofibers and fibers/ground cellulose nanofibers of canola straw, *Ind Crop Prod*, 43 (2013) 732-737.
- [32] R. Mohammadinejad, S. Karimi, S. Iravani and R.S. Varma, Plant-derived nanostructures: types and applications, *Green Chem*, 18 (2016) 20-52.
- [33] A. Endler, C. Sanchez-Rodriguez and S. Persson, GLYCOBIOLOGY Cellulose squeezes through, *Nat Chem Biol*, 6 (2010) 883-884.
- [34] P. Lu and Y.L. Hsieh, Preparation and properties of cellulose nanocrystals: Rods, spheres, and network, *Carbohydr Polym*, 82 (2010) 329-336.
- [35] H.B. Zhao, J.H. Kwak, Z.C. Zhang, H.M. Brown, B.W. Arey and J.E. Holladay, Studying cellulose fiber structure by SEM, XRD, NMR and acid hydrolysis, *Carbohydr Polym*, 68 (2007) 235-241.
- [36] Y. Habibi, Key advances in the chemical modification of nanocelluloses, *Chem Soc Rev*, 43 (2014) 1519-1542.
- [37] T. Abitbol, E. Kloser and D.G. Gray, Estimation of the surface sulfur content of cellulose nanocrystals prepared by sulfuric acid hydrolysis, *Abstr Pap Am Chem S*, 245 (2013).
- [38] S. Beck-Candanedo, M. Roman and D.G. Gray, Effect of reaction conditions on the properties and behavior of wood cellulose nanocrystal

suspensions, *Biomacromolecules*, 6 (2005) 1048-1054.

[39] J.P.F. Lagerwall, C. Schutz, M. Salajkova, J. Noh, J.H. Park, G. Scalia and L. Bergstrom, Cellulose nanocrystal-based materials: from liquid crystal self-assembly and glass formation to multifunctional thin films, *Npg Asia Mater*, 6 (2014).

[40] A.N. Nakagaito and H. Yano, The effect of morphological changes from pulp fiber towards nano-scale fibrillated cellulose on the mechanical properties of high-strength plant fiber based composites, *Appl Phys a-Mater*, 78 (2004) 547-552.

[41] D. Ishii, T. Saito and A. Isogai, Viscoelastic Evaluation of Average Length of Cellulose Nanofibers Prepared by TEMPO-Mediated Oxidation (vol 12, page 548, 2011), *Biomacromolecules*, 13 (2012) 1706-1706.

[42] P. Stenstad, M. Andresen, B.S. Tanem and P. Stenius, Chemical surface modifications of microfibrillated cellulose, *Cellulose*, 15 (2008) 35-45.

[43] A. Alemdar and M. Sain, Isolation and characterization of nanofibers from agricultural residues - Wheat straw and soy hulls, *Bioresource Technol*, 99 (2008) 1664-1671.

[44] K. Abe, S. Iwamoto and H. Yano, Obtaining cellulose nanofibers with a uniform width of 15 nm from wood, *Biomacromolecules*, 8 (2007) 3276-3278.

[45] S. Iwamoto, A.N. Nakagaito and H. Yano, Nano-fibrillation of pulp fibers for the processing of transparent nanocomposites, *Appl Phys a-Mater*, 89 (2007) 461-466.

[46] T. Taniguchi and K. Okamura, New films produced from

microfibrillated natural fibres, *Polym Int*, 47 (1998) 291-294.

[47] T. Saito and A. Isogai, Ion-exchange behavior of carboxylate groups in fibrous cellulose oxidized by the TEMPO-mediated system, *Carbohydr Polym*, 61 (2005) 183-190.

[48] A. Naderi and T. Lindstrom, Carboxymethylated nanofibrillated cellulose: effect of monovalent electrolytes on the rheological properties, *Cellulose*, 21 (2014) 3507-3514.

[49] M. Paakko, M. Ankerfors, H. Kosonen, A. Nykanen, S. Ahola, M. Osterberg, J. Ruokolainen, J. Laine, P.T. Larsson, O. Ikkala and T. Lindstrom, Enzymatic hydrolysis combined with mechanical shearing and high-pressure homogenization for nanoscale cellulose fibrils and strong gels, *Biomacromolecules*, 8 (2007) 1934-1941.

[50] M. Henriksson, G. Henriksson, L.A. Berglund and T. Lindstrom, An environmentally friendly method for enzyme-assisted preparation of microfibrillated cellulose (MFC) nanofibers, *Eur Polym J*, 43 (2007) 3434-3441.

[51] W.S. Chen, H.P. Yu, Y.X. Liu, P. Chen, M.X. Zhang and Y.F. Hai, Individualization of cellulose nanofibers from wood using high-intensity ultrasonication combined with chemical pretreatments, *Carbohydr Polym*, 83 (2011) 1804-1811.

[52] G. Siqueira, S. Tapin-Lingua, J. Bras, D.D. Perez and A. Dufresne, Morphological investigation of nanoparticles obtained from combined mechanical shearing, and enzymatic and acid hydrolysis of sisal fibers,

Cellulose, 17 (2010) 1147-1158.

[53] A.F. Jozala, L.C. de Lencastre-Novaes, A.M. Lopes, V.D. Santos-Ebinuma, P.G. Mazzola, A. Pessoa, D. Grotto, M. Gerenutti and M.V. Chaud, Bacterial nanocellulose production and application: a 10-year overview, *Appl Microbiol Biot*, 100 (2016) 2063-2072.

[54] M. Gama, P. Gatenholm and D. Klemm, Bacterial nanocellulose a sophisticated multifunctional material, in: *Perspectives in nanotechnology*, CRC Press,, Boca Raton, 2013, pp. 1 online resource (p.).

[55] D. Klemm, D. Schumann, F. Kramer, N. Hessler, M. Hornung, H.P. Schmauder and S. Marsch, Nanocelluloses as innovative polymers in research and application, *Adv Polym Sci*, 205 (2006) 49-96.

[56] K. Fleming, D. Gray, S. Prasannan and S. Matthews, Cellulose crystallites: A new and robust liquid crystalline medium for the measurement of residual dipolar couplings, *J Am Chem Soc*, 122 (2000) 5224-5225.

[57] M. Ioelovich, Cellulose as a Nanostructured Polymer: A Short Review, *Bioresources*, 3 (2008) 1403-1418.

[58] M.I. Voronova, A.G. Zakharov, O.Y. Kuznetsov and O.V. Surov, The effect of drying technique of nanocellulose dispersions on properties of dried materials, *Mater Lett*, 68 (2012) 164-167.

[59] C.W. Miao and W.Y. Hamad, Cellulose reinforced polymer composites and nanocomposites: a critical review, *Cellulose*, 20 (2013) 2221-2262.

[60] B. Sun, Q.X. Hou, Z.H. Liu and Y.H. Ni, Sodium periodate oxidation of cellulose nanocrystal and its application as a paper wet strength additive,

Cellulose, 22 (2015) 1135-1146.

[61] A. Salam, L.A. Lucia and H. Jameel, Fluorine-based surface decorated cellulose nanocrystals as potential hydrophobic and oleophobic materials, Cellulose, 22 (2015) 397-406.

[62] B. Sun, Q.X. Hou, Z.H. Liu, Z.B. He and Y.H. Ni, Stability and efficiency improvement of ASA in internal sizing of cellulosic paper by using cationically modified cellulose nanocrystals, Cellulose, 21 (2014) 2879-2887.

[63] U.D. Hemraz, K.A. Campbell, J.S. Burdick, K. Ckless, Y. Boluk and R. Sunasee, Cationic Poly(2-aminoethylmethacrylate) and Poly(N-(2-aminoethylmethacrylamide) Modified Cellulose Nanocrystals: Synthesis, Characterization, and Cytotoxicity, Biomacromolecules, 16 (2015) 319-325.

[64] J.L. Huang, C.J. Li and D.G. Gray, Functionalization of cellulose nanocrystal films via "thiol-ene" click reaction, Rsc Adv, 4 (2014) 6965-6969.

[65] A. Villares, C. Moreau, A. Dammak, I. Capron and B. Cathala, Kinetic aspects of the adsorption of xyloglucan onto cellulose nanocrystals, Soft Matter, 11 (2015) 6472-6481.

[66] T. Saito, Y. Nishiyama, J.L. Putaux, M. Vignon and A. Isogai, Homogeneous suspensions of individualized microfibrils from TEMPO-catalyzed oxidation of native cellulose, Biomacromolecules, 7 (2006) 1687-1691.

[67] T. Abitbol, E. Kloser and D.G. Gray, Estimation of the surface sulfur content of cellulose nanocrystals prepared by sulfuric acid hydrolysis, Cellulose, 20 (2013) 785-794.

- [68] M. Jonoobi, J. Harun, A.P. Mathew, M.Z.B. Hussein and K. Oksman, Preparation of cellulose nanofibers with hydrophobic surface characteristics, *Cellulose*, 17 (2010) 299-307.
- [69] J.H. Bae and S.H. Kim, Alkylation of mixed micro- and nanocellulose to improve dispersion in polylactide, *Polym Int*, 64 (2015) 821-827.
- [70] H. Rosilo, J.R. McKee, E. Kontturi, T. Koho, V.P. Hytonen, O. Ikkala and M.A. Kostiaainen, Cationic polymer brush-modified cellulose nanocrystals for high-affinity virus binding, *Nanoscale*, 6 (2014) 11871-11881.
- [71] U.D. Hemraz, A. Lu, R. Sunasee and Y. Boluk, Structure of poly(N-isopropylacrylamide) brushes and steric stability of their grafted cellulose nanocrystal dispersions, *J Colloid Interf Sci*, 430 (2014) 157-165.
- [72] J.R.G. Navarro, S. Wennmalm, J. Godfrey, M. Breitholtz and U. Edlund, Luminescent Nanocellulose Platform: From Controlled Graft Block Copolymerization to Biomarker Sensing, *Biomacromolecules*, 17 (2016) 1101-1109.
- [73] J.L. Huang, C.J. Li and D.G. Gray, Cellulose Nanocrystals Incorporating Fluorescent Methylcoumarin Groups, *Acs Sustain Chem Eng*, 1 (2013) 1160-1164.
- [74] M.A. Hubbe, O.J. Rojas, L.A. Lucia and M. Sain, Cellulosic Nanocomposites: A Review, *Bioresources*, 3 (2008) 929-980.
- [75] S. Padalkar, J.R. Capadona, S.J. Rowan, C. Weder, Y.H. Won, L.A. Stanciu and R.J. Moon, Natural Biopolymers: Novel Templates for the Synthesis of Nanostructures, *Langmuir*, 26 (2010) 8497-8502.

- [76] E.D. Cranston and D.G. Gray, Morphological and optical characterization of polyelectrolyte multilayers incorporating nanocrystalline cellulose, *Biomacromolecules*, 7 (2006) 2522-2530.
- [77] Q. Zhou, H. Brumer and T.T. Teeri, Self-Organization of Cellulose Nanocrystals Adsorbed with Xyloglucan Oligosaccharide-Poly(ethylene glycol)-Polystyrene Triblock Copolymer, *Macromolecules*, 42 (2009) 5430-5432.
- [78] B. Wang and M. Sain, The Effect of Chemically Coated Nanofiber Reinforcement on Biopolymer Based Nanocomposites, *Bioresources*, 2 (2007) 371-388.
- [79] J.M. Rajwade, K.M. Paknikar and J.V. Kumbhar, Applications of bacterial cellulose and its composites in biomedicine, *Appl Microbiol Biot*, 99 (2015) 2491-2511.
- [80] N. Shah, M. Ul-Islam, W.A. Khattak and J.K. Park, Overview of bacterial cellulose composites: A multipurpose advanced material, *Carbohydr Polym*, 98 (2013) 1585-1598.
- [81] Y. Nishi, M. Uryu, S. Yamanaka, K. Watanabe, N. Kitamura, M. Iguchi and S. Mitsuhashi, The Structure and Mechanical-Properties of Sheets Prepared from Bacterial Cellulose .2. Improvement of the Mechanical-Properties of Sheets and Their Applicability to Diaphragms of Electroacoustic Transducers, *J Mater Sci*, 25 (1990) 2997-3001.
- [82] J. Kucinska-Lipka, I. Gubanska and H. Janik, Bacterial cellulose in the field of wound healing and regenerative medicine of skin: recent trends and

future prospectives, *Polym Bull*, 72 (2015) 2399-2419.

[83] Z.J. Shi, Y. Zhang, G.O. Phillips and G. Yang, Utilization of bacterial cellulose in food, *Food Hydrocolloid*, 35 (2014) 539-545.

[84] W.L. Hu, S.Y. Chen, J.X. Yang, Z. Li and H.P. Wang, Functionalized bacterial cellulose derivatives and nanocomposites, *Carbohydr Polym*, 101 (2014) 1043-1060.

[85] D. Klemm, D. Schumann, U. Udhardt and S. Marsch, Bacterial synthesized cellulose - artificial blood vessels for microsurgery, *Prog Polym Sci*, 26 (2001) 1561-1603.

[86] K. Zaar, Visualization of Pores (Export Sites) Correlated with Cellulose Production in the Envelope of the Gram-Negative Bacterium *Acetobacter-Xylinum*, *J Cell Biol*, 80 (1979) 773-777.

[87] R.M. Brown, J.H.M. Willison and C.L. Richardson, Cellulose Biosynthesis in *Acetobacter-Xylinum* - Visualization of Site of Synthesis and Direct Measurement of In vivo Process, *P Natl Acad Sci USA*, 73 (1976) 4565-4569.

[88] P. Ross, R. Mayer and M. Benziman, Cellulose Biosynthesis and Function in Bacteria, *Microbiol Rev*, 55 (1991) 35-58.

[89] M. Shoda and Y. Sugano, Recent advances in bacterial cellulose production, *Biotechnol Bioproc E*, 10 (2005) 1-8.

[90] H.C. Wong, A.L. Fear, R.D. Calhoon, G.H. Eichinger, R. Mayer, D. Amikam, M. Benziman, D.H. Gelfand, J.H. Meade, A.W. Emerick, R. Bruner, A. Benbassat and R. Tal, Genetic Organization of the Cellulose Synthase

- Operon in *Acetobacter-Xylinum*, *P Natl Acad Sci USA*, 87 (1990) 8130-8134.
- [91] P. Ross, H. Weinhouse, Y. Aloni, D. Michaeli, P. Weinbergerohana, R. Mayer, S. Braun, E. Devroom, G.A. Vandermarel, J.H. Vanboom and M. Benziman, Regulation of Cellulose Synthesis in *Acetobacter-Xylinum* by Cyclic Diguanylic Acid, *Nature*, 325 (1987) 279-281.
- [92] R. Standal, T.G. Iversen, D.H. Coucheron, E. Fjaervik, J.M. Blatny and S. Valla, A New Gene Required for Cellulose Production and a Gene Encoding Cellulolytic Activity in *Acetobacter-Xylinum* Are Colocalized with the Bcs Operon (Vol 176, Pg 665, 1994), *J Bacteriol*, 176 (1994) 3443-3443.
- [93] T. Nakai, Y. Nishiyama, S. Kuga, Y. Sugano and M. Shoda, ORF2 gene involves in the construction of high-order structure of bacterial cellulose, *Biochem Bioph Res Co*, 295 (2002) 458-462.
- [94] K.Y. Lee, G. Buldum, A. Mantalaris and A. Bismarck, More Than Meets the Eye in Bacterial Cellulose: Biosynthesis, Bioprocessing, and Applications in Advanced Fiber Composites, *Macromol Biosci*, 14 (2014) 10-32.
- [95] M. Iguchi, S. Yamanaka and A. Budhiono, Bacterial cellulose - a masterpiece of nature's arts, *J Mater Sci*, 35 (2000) 261-270.
- [96] K. Watanabe and S. Yamanaka, Effects of Oxygen-Tension in the Gaseous-Phase on Production and Physical-Properties of Bacterial Cellulose Formed under Static Culture Conditions, *Biosci Biotech Bioch*, 59 (1995) 65-68.
- [97] P.G. Verschuren, T.D. Cardona, M.J.R. Nout, K.D. De Gooijer and J.C.

Van den Heuvel, Location and limitation of cellulose production by *Acetobacter xylinum* established from oxygen profiles, *J Biosci Bioeng*, 89 (2000) 414-419.

[98] T. Naritomi, T. Kouda, H. Yano and F. Yoshinaga, Effect of ethanol on bacterial cellulose production from fructose in continuous culture, *J Ferment Bioeng*, 85 (1998) 598-603.

[99] H. Kornmann, P. Duboc, I. Marison and U. von Stockar, Influence of nutritional factors on the nature, yield, and composition of exopolysaccharides produced by *Gluconacetobacter xylinus* I-2281, *Appl Environ Microb*, 69 (2003) 6091-6098.

[100] P. DeWulf, K. Joris and E.J. Vandamme, Improved cellulose formation by an *Acetobacter xylinum* mutant limited in (keto)gluconate synthesis, *J Chem Technol Biot*, 67 (1996) 376-380.

[101] R.Q. Wu, Z.X. Li, J.P. Yang, X.H. Xing, D.Y. Shao and K.L. Xing, Mutagenesis induced by high hydrostatic pressure treatment: a useful method to improve the bacterial cellulose yield of a *Gluconoacetobacter xylinus* strain, *Cellulose*, 17 (2010) 399-405.

[102] A. Krystynowicz, W. Czaja, A. Wiktorowska-Jeziarska, M. Goncalves-Miskiewicz, M. Turkiewicz and S. Bielecki, Factors affecting the yield and properties of bacterial cellulose, *J Ind Microbiol Biot*, 29 (2002) 189-195.

[103] K.C. Cheng, J.M. Catchmark and A. Demirci, Effects of CMC Addition on Bacterial Cellulose Production in a Biofilm Reactor and Its Paper Sheets Analysis, *Biomacromolecules*, 12 (2011) 730-736.

- [104] H.J. Song, H.X. Li, J.H. Seo, M.J. Kim and S.J. Kim, Pilot-scale production of bacterial cellulose by a spherical type bubble column bioreactor using saccharified food wastes, *Korean J Chem Eng*, 26 (2009) 141-146.
- [105] H.P. Cheng, P.M. Wang, J.W. Chen and W.T. Wu, Cultivation of *Acetobacter xylinum* for bacterial cellulose production in a modified airlift reactor, *Biotechnol Appl Bioc*, 35 (2002) 125-132.
- [106] A. Sani and Y. Dahman, Improvements in the production of bacterial synthesized biocellulose nanofibres using different culture methods, *J Chem Technol Biot*, 85 (2010) 151-164.
- [107] Y.J. Kim, J.N. Kim, Y.J. Wee, D.H. Park and H.W. Ryu, Bacterial cellulose production by *Gluconacetobacter* sp RKY5 in a rotary biofilm contactor, *Appl Biochem Biotech*, 137 (2007) 529-537.
- [108] K.Y. Qiu and A.N. Netravali, A Review of Fabrication and Applications of Bacterial Cellulose Based Nanocomposites, *Polym Rev*, 54 (2014) 598-626.
- [109] G. Guhadós, W.K. Wan and J.L. Hutter, Measurement of the elastic modulus of single bacterial cellulose fibers using atomic force microscopy, *Langmuir*, 21 (2005) 6642-6646.
- [110] S. Yamanaka, K. Watanabe, N. Kitamura, M. Iguchi, S. Mitsuhashi, Y. Nishi and M. Uryu, The Structure and Mechanical-Properties of Sheets Prepared from Bacterial Cellulose, *J Mater Sci*, 24 (1989) 3141-3145.
- [111] Y. Chen, A.J. Stipanovic, W.T. Winter, D.B. Wilson and Y.J. Kim, Effect of digestion by pure cellulases on crystallinity and average chain length

- for bacterial and microcrystalline celluloses, *Cellulose*, 14 (2007) 283-293.
- [112] I. Sulaeva, U. Henniges, T. Rosenau and A. Potthast, Bacterial cellulose as a material for wound treatment: Properties and modifications. A review, *Biotechnol Adv*, 33 (2015) 1547-1571.
- [113] A.H. Basta and H. El-Saied, Performance of improved bacterial cellulose application in the production of functional paper, *J Appl Microbiol*, 107 (2009) 2098-2107.
- [114] L.C. Tome, R.J.B. Pinto, E. Trovatti, C.S.R. Freire, A.J.D. Silvestre, C.P. Neto and A. Gandini, Transparent bionanocomposites with improved properties prepared from acetylated bacterial cellulose and poly(lactic acid) through a simple approach, *Green Chem*, 13 (2011) 419-427.
- [115] S.C.M. Fernandes, L. Oliveira, C.S.R. Freire, A.J.D. Silvestre, C.P. Neto, A. Gandini and J. Desbrieres, Novel transparent nanocomposite films based on chitosan and bacterial cellulose, *Green Chem*, 11 (2009) 2023-2029.
- [116] E. Trovatti, S.C.M. Fernandes, L. Rubatat, C.S.R. Freire, A.J.D. Silvestre and C.P. Neto, Sustainable nanocomposite films based on bacterial cellulose and pullulan, *Cellulose*, 19 (2012) 729-737.
- [117] M. Nogi, K. Handa, A.N. Nakagaito and H. Yano, Optically transparent bionanofiber composites with low sensitivity to refractive index of the polymer matrix, *Appl Phys Lett*, 87 (2005).
- [118] Y.J. Choi, Y.H. Ahn, M.S. Kang, H.K. Jun, I.S. Kim and S.H. Moon, Preparation and characterization of acrylic acid-treated bacterial cellulose cation-exchange membrane, *J Chem Technol Biot*, 79 (2004) 79-84.

- [119] C. Bodhibukkana, T. Srichana, S. Kaewnopparat, N. Tangthong, P. Bouking, G.P. Martin and R. Suedee, Composite membrane of bacterially-derived cellulose and molecularly imprinted polymer for use as a transdermal enantioselective controlled-release system of racemic propranolol, *J Control Release*, 113 (2006) 43-56.
- [120] S.H. Yoon, H.J. Jin, M.C. Kook and Y.R. Pyun, Electrically conductive bacterial cellulose by incorporation of carbon nanotubes, *Biomacromolecules*, 7 (2006) 1280-1284.
- [121] W.L. Hu, S.Y. Chen, Z.H. Yang, L.T. Liu and H.P. Wang, Flexible Electrically Conductive Nanocomposite Membrane Based on Bacterial Cellulose and Polyaniline, *J Phys Chem B*, 115 (2011) 8453-8457.
- [122] B.H. Lee, H.J. Kim and H.S. Yang, Polymerization of aniline on bacterial cellulose and characterization of bacterial cellulose/polyaniline nanocomposite films, *Curr Appl Phys*, 12 (2012) 75-80.
- [123] Z.J. Shi, S.S. Zang, F. Jiang, L. Huang, D. Lu, Y.G. Ma and G. Yang, In situ nano-assembly of bacterial cellulose-polyaniline composites, *Rsc Adv*, 2 (2012) 1040-1046.
- [124] C. Legnani, C. Vilani, V.L. Calil, H.S. Barud, W.G. Quirino, C.A. Achete, S.J.L. Ribeiro and M. Cremona, Bacterial cellulose membrane as flexible substrate for organic light emitting devices, *Thin Solid Films*, 517 (2008) 1016-1020.
- [125] J. Shah and R.M. Brown, Towards electronic paper displays made from microbial cellulose, *Appl Microbiol Biot*, 66 (2005) 352-355.

- [126] Y.Y. Feng, X.Q. Zhang, Y.T. Shen, K. Yoshino and W. Feng, A mechanically strong, flexible and conductive film based on bacterial cellulose/graphene nanocomposite, *Carbohydr Polym*, 87 (2012) 644-649.
- [127] B.R. Evans, H.M. O'Neill, V.P. Malyvanh, I. Lee and J. Woodward, Palladium-bacterial cellulose membranes for fuel cells, *Biosens Bioelectron*, 18 (2003) 917-923.
- [128] A.J.D. Silvestre, C.S.R. Freire and C.P. Neto, Do bacterial cellulose membranes have potential in drug-delivery systems?, *Expert Opin Drug Del*, 11 (2014) 1113-1124.
- [129] D. Ciechanska, Multifunctional bacterial cellulose/chitosan composite materials for medical applications, *Fibres Text East Eur*, 12 (2004) 69-72.
- [130] L.E. Million, G. Guhados and W.K. Wan, Anisotropic polyvinyl alcohol-bacterial cellulose nanocomposite for biomedical applications, *J Biomed Mater Res B*, 86B (2008) 444-452.
- [131] H.L. Luo, G.Y. Xiong, Y. Huang, F. He, W. Wang and Y.Z. Wan, Preparation and characterization of a novel COL/BC composite for potential tissue engineering scaffolds, *Mater Chem Phys*, 110 (2008) 193-196.
- [132] Z. Cai and J. Kim, Bacterial cellulose/poly(ethylene glycol) composite: characterization and first evaluation of biocompatibility, *Cellulose*, 17 (2010) 83-91.
- [133] M.L. Cacicedo, I.E. Leon, J.S. Gonzalez, L.M. Porto, V.A. Alvarez and G.R. Castro, Modified bacterial cellulose scaffolds for localized doxorubicin release in human colorectal HT-29 cells, *Colloid Surface B*, 140 (2016) 421-

429.

[134] J.W. Rhim, H.M. Park and C.S. Ha, Bio-nanocomposites for food packaging applications, *Prog Polym Sci*, 38 (2013) 1629-1652.

[135] A. Sorrentino, G. Gorrasi and V. Vittoria, Potential perspectives of bio-nanocomposites for food packaging applications, *Trends Food Sci Tech*, 18 (2007) 84-95.

[136] J. Yun and H.I. Kim, Electromagnetic interference shielding effects of polyaniline-coated multi-wall carbon nanotubes/maghemite nanocomposites, *Polym Bull*, 68 (2012) 561-573.

[137] D.A. Cerqueira, A.J.M. Valente, G.R. Filho and H.D. Burrows, Synthesis and properties of polyaniline-cellulose acetate blends: The use of sugarcane bagasse waste and the effect of the substitution degree, *Carbohydr Polym*, 78 (2009) 402-408.

[138] K. Lakshmi, H. John, K.T. Mathew, R. Joseph and K.E. George, Microwave absorption, reflection and EMI shielding of PU-PANI composite, *Acta Mater*, 57 (2009) 371-375.

[139] N.C. Das, S. Yamazaki, M. Hikosaka, T.K. Chaki, D. Khastgir and A. Chakraborty, Electrical conductivity and electromagnetic interference shielding effectiveness of polyaniline-ethylene vinyl acetate composites, *Polym Int*, 54 (2005) 256-259.

[140] Y.H. Niu, Preparation of polyaniline/polyacrylate composites and their application for electromagnetic interference shielding, *Polym Composite*, 27 (2006) 627-632.

- [141] N.C. Das and S. Maiti, Electromagnetic interference shielding of carbon nanotube/ethylene vinyl acetate composites, *J Mater Sci*, 43 (2008) 1920-1925.
- [142] J. Jiang, L.C. Li and M. Zhu, Polyaniline/magnetic ferrite nanocomposites obtained by in situ polymerization, *React Funct Polym*, 68 (2008) 57-62.
- [143] M. Armand and J.M. Tarascon, Building better batteries, *Nature*, 451 (2008) 652-657.
- [144] M. Winter, J.O. Besenhard, M.E. Spahr and P. Novak, Insertion electrode materials for rechargeable lithium batteries, *Adv Mater*, 10 (1998) 725-763.
- [145] M.S. Whittingham, Lithium batteries and cathode materials, *Chem Rev*, 104 (2004) 4271-4301.
- [146] H. Wu, G. Chan, J.W. Choi, I. Ryu, Y. Yao, M.T. McDowell, S.W. Lee, A. Jackson, Y. Yang, L.B. Hu and Y. Cui, Stable cycling of double-walled silicon nanotube battery anodes through solid-electrolyte interphase control, *Nat Nanotechnol*, 7 (2012) 309-314.
- [147] W.J. Zhang, A review of the electrochemical performance of alloy anodes for lithium-ion batteries, *J Power Sources*, 196 (2011) 13-24.
- [148] Y.M. Chiang, Building a Better Battery, *Science*, 330 (2010) 1485-1486.
- [149] H. Wu and Y. Cui, Designing nanostructured Si anodes for high energy lithium ion batteries, *Nano Today*, 7 (2012) 414-429.
- [150] U. Kasavajjula, C.S. Wang and A.J. Appleby, Nano- and bulk-silicon-

based insertion anodes for lithium-ion secondary cells, *J Power Sources*, 163 (2007) 1003-1039.

[151] M.Y. Ge, J.P. Rong, X. Fang and C.W. Zhou, Porous Doped Silicon Nanowires for Lithium Ion Battery Anode with Long Cycle Life, *Nano Lett*, 12 (2012) 2318-2323.

[152] L.F. Cui, Y. Yang, C.M. Hsu and Y. Cui, Carbon-Silicon Core-Shell Nanowires as High Capacity Electrode for Lithium Ion Batteries, *Nano Lett*, 9 (2009) 3370-3374.

[153] N. Liu, H. Wu, M.T. McDowell, Y. Yao, C.M. Wang and Y. Cui, A Yolk-Shell Design for Stabilized and Scalable Li-Ion Battery Alloy Anodes, *Nano Lett*, 12 (2012) 3315-3321.

[154] B.R. Liu, P. Soares, C. Checkles, Y. Zhao and G.H. Yu, Three-Dimensional Hierarchical Ternary Nanostructures for High-Performance Li-Ion Battery Anodes, *Nano Lett*, 13 (2013) 3414-3419.

[155] S. Bhadra, D. Khastgir, N.K. Singha and J.H. Lee, Progress in preparation, processing and applications of polyaniline, *Prog Polym Sci*, 34 (2009) 783-810.

[156] E.M. Genies, A. Boyle, M. Lapkowski and C. Tsintavis, Polyaniline - a Historical Survey, *Synthetic Met*, 36 (1990) 139-182.

[157] L.F. Chen, Z.H. Huang, H.W. Liang, W.T. Yao, Z.Y. Yu and S.H. Yu, Flexible all-solid-state high-power supercapacitor fabricated with nitrogen-doped carbon nanofiber electrode material derived from bacterial cellulose, *Energ Environ Sci*, 6 (2013) 3331-3338.

- [158] L.F. Chen, Z.H. Huang, H.W. Liang, Q.F. Guan and S.H. Yu, Bacterial-Cellulose-Derived Carbon Nanofiber@MnO₂ and Nitrogen-Doped Carbon Nanofiber Electrode Materials: An Asymmetric Supercapacitor with High Energy and Power Density, *Adv Mater*, 25 (2013) 4746-4752.
- [159] T.F. Wu, T.M. Yen, Y.Y. Han, Y.J. Chiu, E.Y.S. Lin and Y.H. Lo, A light-sheet microscope compatible with mobile devices for label-free intracellular imaging and biosensing, *Lab Chip*, 14 (2014) 3341-3348.
- [160] H. Wu, G.H. Yu, L.J. Pan, N.A. Liu, M.T. McDowell, Z.A. Bao and Y. Cui, Stable Li-ion battery anodes by in-situ polymerization of conducting hydrogel to conformally coat silicon nanoparticles, *Nat Commun*, 4 (2013).
- [161] K.M. Harmon, Hydrogen-Bonding in Biological Structures - Jeffrey, G., Saenger, W., *Science*, 257 (1992) 1774-1775.
- [162] M. Takai, Y. Tsuta, J. Hayashi and S. Watanabe, Biosynthesis of Cellulose by *Acetobacter-Xylinum* .3. X-Ray Studies of Preferential Orientation of Crystallites in a Bacterial Cellulose Membrane, *Polym J*, 7 (1975) 157-164.
- [163] H.K. Chaudhari and D.S. Kelkar, Investigation of structure and electrical conductivity in doped polyaniline, *Polym Int*, 42 (1997) 380-384.
- [164] Y.H. Xu, G.P. Yin, Y.L. Ma, P.J. Zuo and X.Q. Cheng, Nanosized core/shell silicon@carbon anode material for lithium ion batteries with polyvinylidene fluoride as carbon source, *J Mater Chem*, 20 (2010) 3216-3220.
- [165] J.K. Lee, K.B. Smith, C.M. Hayner and H.H. Kung, Silicon

nanoparticles-graphene paper composites for Li ion battery anodes, *Chem Commun*, 46 (2010) 2025-2027.

[166] M. Sureshkumar, D.Y. Siswanto and C.K. Lee, Magnetic antimicrobial nanocomposite based on bacterial cellulose and silver nanoparticles, *J Mater Chem*, 20 (2010) 6948-6955.

[167] G.F. Perotti, H.S. Barud, S.J.L. Ribeiro and V.R.L. Constantino, Bacterial Cellulose as a Template for Preparation of Hydrotalcite-Like Compounds, *J Brazil Chem Soc*, 25 (2014) 1647-1655.

[168] Y. Wei and K.F. Hsueh, Thermal-Analysis of Chemically Synthesized Polyaniline and Effects of Thermal Aging on Conductivity, *J Polym Sci Pol Chem*, 27 (1989) 4351-4363.

[169] S. Sinha, S. Bhadra and D. Khastgir, Effect of Dopant Type on the Properties of Polyaniline, *J Appl Polym Sci*, 112 (2009) 3135-3140.

[170] J.P. Singh, H.Y. Chu, J. Abell, R.A. Tripp and Y.P. Zhao, Flexible and mechanical strain resistant large area SERS active substrates, *Nanoscale*, 4 (2012) 3410-3414.

[171] S. Chang, Z.A. Combs, M.K. Gupta, R. Davis and V.V. Tsukruk, In situ Growth of Silver Nanoparticles in Porous Membranes for Surface-Enhanced Raman Scattering, *Acs Appl Mater Inter*, 2 (2010) 3333-3339.

[172] X.S. Wang, P. Huang, L.L. Feng, M. He, S.W. Guo, G.X. Shen and D.X. Cui, Green controllable synthesis of silver nanomaterials on graphene oxide sheets via spontaneous reduction, *Rsc Adv*, 2 (2012) 3816-3822.

[173] H. Ko, S. Singamaneni and V.V. Tsukruk, Nanostructured Surfaces

and Assemblies as SERS Media, *Small*, 4 (2008) 1576-1599.

[174] A.M. Yu, Z.J. Liang, J. Cho and F. Caruso, Nanostructured electrochemical sensor based on dense gold nanoparticle films, *Nano Lett*, 3 (2003) 1203-1207.

[175] Y. Lu, G.L. Liu and L.P. Lee, High-density silver nanoparticle film with temperature-controllable interparticle spacing for a tunable surface enhanced Raman scattering substrate, *Nano Lett*, 5 (2005) 5-9.

[176] R.G. Freeman, K.C. Grabar, K.J. Allison, R.M. Bright, J.A. Davis, A.P. Guthrie, M.B. Hommer, M.A. Jackson, P.C. Smith, D.G. Walter and M.J. Natan, Self-Assembled Metal Colloid Monolayers - an Approach to Sers Substrates, *Science*, 267 (1995) 1629-1632.

[177] H.C. Lo, H.I. Hsiung, S. Chattopadhyay, H.C. Han, C.F. Chen, J.P. Leu, K.H. Chen and L.C. Chen, Label free sub-picomole level DNA detection with Ag nanoparticle decorated Au nanotip arrays as surface enhanced Raman spectroscopy platform, *Biosens Bioelectron*, 26 (2011) 2413-2418.

[178] H.B. Tang, G.W. Meng, Q. Huang, Z. Zhang, Z.L. Huang and C.H. Zhu, Arrays of Cone-Shaped ZnO Nanorods Decorated with Ag Nanoparticles as 3D Surface-Enhanced Raman Scattering Substrates for Rapid Detection of Trace Polychlorinated Biphenyls, *Adv Funct Mater*, 22 (2012) 218-224.

[179] K.S. Krishna, C.S.S. Sandeep, R. Philip and M. Eswaramoorthy, Mixing Does the Magic: A Rapid Synthesis of High Surface Area Noble Metal Nanosponges Showing Broadband Nonlinear Optical Response, *Acs Nano*, 4 (2010) 2681-2688.

- [180] S. Lee, M.G. Hahm, R. Vajtai, D.P. Hashim, T. Thurakitsee, A.C. Chipara, P.M. Ajayan and J.H. Hafner, Utilizing 3D SERS Active Volumes in Aligned Carbon Nanotube Scaffold Substrates, *Adv Mater*, 24 (2012) 5261-5266.
- [181] Y.H. Ngo, D. Li, G.P. Simon and G. Garnier, Gold Nanoparticle-Paper as a Three-Dimensional Surface Enhanced Raman Scattering Substrate, *Langmuir*, 28 (2012) 8782-8790.
- [182] E.Z. Tan, P.G. Yin, T.T. You, H. Wang and L. Guo, Three Dimensional Design of Large-Scale TiO₂ Nanorods Scaffold Decorated by Silver Nanoparticles as SERS Sensor for Ultrasensitive Malachite Green Detection, *Acs Appl Mater Inter*, 4 (2012) 3432-3437.
- [183] J. Cai, S. Kimura, M. Wada and S. Kuga, Nanoporous Cellulose as Metal Nanoparticles Support, *Biomacromolecules*, 10 (2009) 87-94.
- [184] X.G. Luo, S.L. Liu, J.P. Zhou and L.N. Zhang, In situ synthesis of Fe₃O₄/cellulose microspheres with magnetic-induced protein delivery, *J Mater Chem*, 19 (2009) 3538-3545.
- [185] J.J. Wu, N. Zhao, X.L. Zhang and J. Xu, Cellulose/silver nanoparticles composite microspheres: eco-friendly synthesis and catalytic application, *Cellulose*, 19 (2012) 1239-1249.
- [186] J.J. Tan, R.G. Liu, W. Wang, W.Y. Liu, Y. Tian, M. Wu and Y. Huang, Controllable Aggregation and Reversible pH Sensitivity of AuNPs Regulated by Carboxymethyl Cellulose, *Langmuir*, 26 (2010) 2093-2098.
- [187] R.T. Olsson, M.A.S.A. Samir, G. Salazar-Alvarez, L. Belova, V. Strom,

L.A. Berglund, O. Ikkala, J. Noguees and U.W. Gedde, Making flexible magnetic aerogels and stiff magnetic nanopaper using cellulose nanofibrils as templates, *Nat Nanotechnol*, 5 (2010) 584-588.

[188] T.J. Zhang, W. Wang, D.Y. Zhang, X.X. Zhang, Y.R. Ma, Y.L. Zhou and L.M. Qi, Biotemplated Synthesis of Gold Nanoparticle-Bacteria Cellulose Nanofiber Nanocomposites and Their Application in Biosensing, *Adv Funct Mater*, 20 (2010) 1152-1160.

[189] K. Vimala, K.S. Sivudu, Y.M. Mohan, B. Sreedhar and K.M. Raju, Controlled silver nanoparticles synthesis in semi-hydrogel networks of poly(acrylamide) and carbohydrates: A rational methodology for antibacterial application, *Carbohydr Polym*, 75 (2009) 463-471.

[190] G. Yang, J.J. Xie, Y.X. Deng, Y.G. Bian and F. Hong, Hydrothermal synthesis of bacterial cellulose/AgNPs composite: A "green" route for antibacterial application, *Carbohydr Polym*, 87 (2012) 2482-2487.

[191] C. Tokoh, K. Takabe, M. Fujita and H. Saiki, Cellulose synthesized by *Acetobacter xylinum* in the presence of acetyl glucomannan, *Cellulose*, 5 (1998) 249-261.

[192] H.M. Badawi and W. Forner, Analysis of the infrared and Raman spectra of phenylacetic acid and mandelic (2-hydroxy-2-phenylacetic) acid, *Spectrochim Acta A*, 78 (2011) 1162-1167.

[193] J.S. Suh, M. Moskovits and J. Shakhsemampour, Photochemical Decomposition at Colloid Surfaces, *J Phys Chem-US*, 97 (1993) 1678-1683.

[194] D.H. Jeong, J.S. Suh and M. Moskovits, Photochemical reactions of

phenazine and acridine adsorbed on silver colloid surfaces, *J Phys Chem B*, 104 (2000) 7462-7467.

[195] W.J. Zhang, S.T. Zhao, W. Rao, J. Snyder, J.K. Choi, J.F. Wang, I.A. Khan, N.B. Saleh, P.J. Mohler, J.H. Yu, T.J. Hund, C.B. Tang and X.M. He, A novel core-shell microcapsule for encapsulation and 3D culture of embryonic stem cells, *J Mater Chem B*, 1 (2013) 1002-1009.

[196] A.M. Rokstad, I. Lacik, P. de Vos and B.L. Strand, Advances in biocompatibility and physico-chemical characterization of microspheres for cell encapsulation, *Adv Drug Deliv Rev*, (2013).

[197] G. Orive, R.M. Hernandez, A.R. Gascon, R. Calafiore, T.M. Chang, P. De Vos, G. Hortelano, D. Hunkeler, I. Lacik, A.M. Shapiro and J.L. Pedraz, Cell encapsulation: promise and progress, *Nat Med*, 9 (2003) 104-107.

[198] J.J. Schmidt, J. Rowley and H.J. Kong, Hydrogels used for cell-based drug delivery, *J Biomed Mater Res A*, 87A (2008) 1113-1122.

[199] K.I. Draget, K. Steinsvag, E. Onsoyen and O. Smidsrod, Na- and K-alginate; effect on Ca²⁺-gelation, *Carbohydr Polym*, 35 (1998) 1-6.

[200] N. Lin, C. Bruzzese and A. Dufresne, TEMPO-Oxidized Nanocellulose Participating as Crosslinking Aid for Alginate-Based Sponges, *Acs Appl Mater Inter*, 4 (2012) 4948-4959.

[201] S. Fujisawa, Y. Okita, H. Fukuzumi, T. Saito and A. Isogai, Preparation and characterization of TEMPO-oxidized cellulose nanofibril films with free carboxyl groups, *Carbohydr Polym*, 84 (2011) 579-583.

[202] H. Dong, J.F. Snyder, K.S. Williams and J.W. Andzelm, Cation-

induced hydrogels of cellulose nanofibrils with tunable moduli, *Biomacromolecules*, 14 (2013) 3338-3345.

[203] J.L. Pedraz and G. Orive, *Therapeutic applications of cell microencapsulation*, Springer Science+Business Media ; Landes Bioscience, New York Austin, Tex., 2010.

[204] A. Ostlund, D. Lundberg, L. Nordstierna, K. Holmberg and M. Nyden, *Dissolution and Gelation of Cellulose in TBAF/DMSO Solutions: The Roles of Fluoride Ions and Water*, *Biomacromolecules*, 10 (2009) 2401-2407.

[205] G. Marci, G. Mele, L. Palmisano, P. Pulito and A. Sannino, *Environmentally sustainable production of cellulose-based superabsorbent hydrogels*, *Green Chem*, 8 (2006) 439-444.

[206] B. Fei, R.A. Wach, H. Mitomo, F. Yoshii and T. Kume, *Hydrogel of biodegradable cellulose derivatives. I. Radiation-induced crosslinking of CMC*, *Journal of Applied Polymer Science*, 78 (2000) 278-283.

[207] Q. Zhao, J.W. Qian, Q.F. An, C.J. Gao, Z.L. Gui and H.T. Jin, *Synthesis and characterization of soluble chitosan/sodium carboxymethyl cellulose polyelectrolyte complexes and the pervaporation dehydration of their homogeneous membranes*, *Journal of Membrane Science*, 333 (2009) 68-78.

[208] C.Y. Chang, A. Lue and L. Zhang, *Effects of crosslinking methods on structure and properties of cellulose/PVA hydrogels*, *Macromol Chem Physic*, 209 (2008) 1266-1273.

[209] M.C.I.M. Amin, N. Ahmad, N. Halib and I. Ahmad, *Synthesis and*

characterization of thermo- and pH-responsive bacterial cellulose/acrylic acid hydrogels for drug delivery, *Carbohydr Polym*, 88 (2012) 465-473.

[210] K.S. Halake and J. Lee, Superporous thermo-responsive hydrogels by combination of cellulose fibers and aligned micropores, *Carbohydr Polym*, 105 (2014) 184-192.

[211] S. Ekici, Intelligent poly(N-isopropylacrylamide)-carboxymethyl cellulose full interpenetrating polymeric networks for protein adsorption studies, *J Mater Sci*, 46 (2011) 2843-2850.

[212] L. Li, P.M. Thangamathesvaran, C.Y. Yue, K.C. Tam, X. Hu and Y.C. Lam, Gel network structure of methylcellulose in water, *Langmuir*, 17 (2001) 8062-8068.

[213] S.M.C. Silva, F.V. Pinto, F.E. Antunes, M.G. Miguel, J.J.S. Sousa and A. Pais, Aggregation and gelation in hydroxypropylmethyl cellulose aqueous solutions, *Journal of Colloid and Interface Science*, 327 (2008) 333-340.

[214] D.L. Nettles, A. Chilkoti and L.A. Setton, Applications of elastin-like polypeptides in tissue engineering, *Adv Drug Deliver Rev*, 62 (2010) 1479-1485.

[215] G.L. Bidwell and D. Raucher, Cell penetrating elastin-like polypeptides for therapeutic peptide delivery, *Advanced Drug Delivery Reviews*, 62 (2010) 1486-1496.

[216] A.J. Simnick, D.W. Lim, D. Chow and A. Chilkoti, Biomedical and biotechnological applications of elastin-like polypeptides, *Polymer Reviews*, 47 (2007) 121-154.

- [217] J. Cheng, K. Na, H.S. Kim, C.K. Lee and J. Hyun, "Smart" microspheres for self-renewal of embryonic stem cells, *Macromol Res*, 21 (2013) 134-136.
- [218] Y.Y. Zhang, X.J. Xu and L. Zhang, Dynamic viscoelastic behavior of triple helical Lentinan in water: Effect of temperature, *Carbohydr Polym*, 73 (2008) 26-34.
- [219] A.K.A.S. Brun-Graeppi, C. Richard, M. Bessodes, D. Scherman, T. Narita, G. Ducouret and O.W. Merten, Study on the sol-gel transition of xyloglucan hydrogels, *Carbohydr Polym*, 80 (2010) 555-562.
- [220] A. Karppinen, A.H. Vesterinen, T. Saarinen, P. Pietikainen and J. Seppala, Effect of cationic polymethacrylates on the rheology and flocculation of microfibrillated cellulose, *Cellulose*, 18 (2011) 1381-1390.
- [221] P. Myllytie, S. Holappa, J. Paltakari and J. Laine, Effect of polymers on aggregation of cellulose fibrils and its implication on strength development in wet paper web, *Nord Pulp Pap Res J*, 24 (2009) 125-134.
- [222] C.G. de Kruif, F. Weinbreck and R. de Vries, Complex coacervation of proteins and anionic polysaccharides, *Curr Opin Colloid In*, 9 (2004) 340-349.
- [223] C. Schmitt, C. Sanchez, S. Desobry-Banon and J. Hardy, Structure and technofunctional properties of protein-polysaccharide complexes: A review, *Crit Rev Food Sci*, 38 (1998) 689-753.
- [224] S.L. Turgeon, C. Schmitt and C. Sanchez, Protein-polysaccharide complexes and coacervates, *Curr Opin Colloid In*, 12 (2007) 166-178.
- [225] Y.A. Antonov, J. Lefebvre and J.L. Doublier, On the one-phase state

of aqueous protein uncharged polymer systems: Casein-guar gum system, *J Appl Polym Sci*, 71 (1999) 471-482.

[226] V.B. Tolstoguzov, Functional properties of food proteins and role of protein-polysaccharide interaction, *Food Hydrocolloid*, 4 (1991) 429-468.

[227] Y.A. Antonov and B.A. Wolf, Calorimetric and structural investigation of the interaction between bovine serum albumin and high molecular weight dextran in water, *Biomacromolecules*, 6 (2005) 2980-2989.

[228] Y. Cho, L.B. Sagle, S. Iimura, Y.J. Zhang, J. Kherb, A. Chilkoti, J.M. Scholtz and P.S. Cremer, Hydrogen Bonding of beta-Turn Structure Is Stabilized in D₂O, *J Am Chem Soc*, 131 (2009) 15188-15193.

[229] H. Nuhn and H.A. Klok, Secondary Structure Formation and LCST Behavior of Short Elastin-Like Peptides, *Biomacromolecules*, 9 (2008) 2755-2763.

[230] D.W. Urry, Molecular Machines - How Motion and Other Functions of Living Organisms Can Result from Reversible Chemical-Changes, *Angewandte Chemie-International Edition in English*, 32 (1993) 819-841.

초록

본 논문에서는 적합한 합성전략을 통해 박테리아 셀룰로오스에 무기나노입자와 바이오폴리머를 도입한 나노복합체를 제작하였고, 그 응용가능성을 평가해 보았다.

첫 번째로 자성나노입자, 실리콘나노입자, 금나노입자를 각각 박테리아 셀룰로오스와 복합화하였다. 자성 박테리아셀룰로오스 복합체는 자성나노입자가 함유된 배지에 박테리아를 배양하는 생합성 방법을 통하여 제조하였고, 아닐린 모노머를 도입하여 전도성 고분자인 폴리아닐린을 중합하였다. 전자기 차폐막으로의 응용가능성을 파악하기 위해 자성과 전기전도성 측정 실험을 수행하였고, 합성된 복합체는 전도성과 자성을 모두 가졌다. 실리콘나노입자가 함유된 박테리아 셀룰로오스 나노복합체는 안정적으로 분산된 실리콘나노입자 분산용액에 박테리아셀룰로오스를 담침시키는 방법으로 제조하였다. 실리콘 나노입자들은 셀룰로오스 나노섬유에 균일하게 도입되었다. 이 후, 폴리아닐린을 중합하여 복합체에 전도성을 부여하였다. 완성된 복합체는 반복적인 구부림 시험에서 일정한 전기 전도성을 나타내었다. 이를 통하여 유연성 전극으로 응용이 가능함을 확인하였다. 금나노입자-박테리아셀룰로오스 복합체는 *in situ* 합성법을 통해 제조되었다. 셀룰로오스 나노섬유는 합성 과정에서 지지체이자 환원제로서 역할을 하였다. 제조된 복합체의 구조적 변형을 통하여 분석물질의 표면 증강 라만 산란 신호를 크게 증가시킬 수 있었다.

두 번째로, TEMPO/NaBr/NaClO 산화 시스템을 통해 개질된 박테리아셀룰로오스와 바이오폴리머를 이용한 복합체를 제작하였다. 수용액에 잘 분산된 산화 박테리아셀룰로오스를 알지네이트와 섞고, 칼슘이온에 의한 이온가교를 유도하여 하이드로젤 형태로 제조하였다. 형

성된 복합체는 기계적·화학적 저항성이 증가하였고, 세포 담지체로서의 응용가능성이 평가되었다. 수용액상에서 양전하를 갖는 엘라스틴 유래 폴리펩타이드와 음전하를 갖는 산화 박테리아 셀룰로오스를 이용하여 온도민감성 하이드로젤 복합체를 제조하였다. 온도가 증가함에 따라 엘라스틴 유래 폴리펩타이드가 물리적 가교제로 작용을 하여 하이드로젤이 형성되고, 온도가 낮아짐에 따라 젤-졸 전이가 일어났다. 이 후 세포 실험을 통하여 하이드로젤 내부에서 세포를 안정적으로 성장시킬 수 있었다.

위와 같은 적합한 합성전략을 통한 다양한 박테리아셀룰로오스 기반 나노복합체 연구들은 소재로서의 박테리아 셀룰로오스에 대한 이해를 넓혀주고, 다양한 분야로의 응용 가능성을 높여 줄 수 있을 것으로 기대한다.

색인어: 박테리아 셀룰로오스 복합체, 무기나노입자, 자성나노입자, 실리콘나노입자, 금 나노입자, 바이오폴리머, 알지네이트, 엘라스틴 유래 폴리펩타이드

학 번: 2011-21250